THE CONTRIBUTION OF LARGE, SLOW-MOVING LANDSLIDES TO LANDSCAPE EVOLUTION

by

BENJAMIN HUNTER MACKEY

A DISSERTATION

Presented to the Department of Geological Sciences
and the Graduate School of the University of Oregon
in partial fulfillment of the requirements
for the degree of
Doctor of Philosophy

December 2009

University of Oregon Graduate School

Confirmation of Approval and Acceptance of Dissertation prepared by:

Benjamin Mackey

Title:

"The Contribution of Large, Slow-Moving Landslides to Landscape Evolution"

This dissertation has been accepted and approved in partial fulfillment of the requirements for the Doctor of Philosophy degree in the Department of Geological Sciences by:

Joshua Roering, Chairperson, Geological Sciences
Ilya Bindeman, Member, Geological Sciences
Dean Livelybrooks, Member, Physics
Ray Weldon, Member, Geological Sciences
W. Andrew Marcus, Outside Member, Geography

and Richard Linton, Vice President for Research and Graduate Studies/Dean of the Graduate School for the University of Oregon.

December 12, 2009

Original approval signatures are on file with the Graduate School and the University of Oregon Libraries.

An Abstract of the Dissertation of

Benjamin Hunter Mackey for the degree of Doctor of Philosophy

in the Department of Geological Sciences to be taken December 2009

Title: THE CONTRIBUTION OF LARGE, SLOW-MOVING LANDSLIDES TO LANDSCAPE EVOLUTION

Approved: _____
Joshua J. Roering

This dissertation discusses the contribution of deep-seated landslides and earthflows to the morphology, erosion, and evolution of mountainous landscapes, focusing on the northern California Coast Ranges.

In active landscapes, channel incision is necessary to create relief but also increases stresses in adjacent hillslopes, ultimately leading to slope failure. While conceptually simple, the spatial relationships between channel incision and landsliding have not been well quantified. Along the South Fork Eel River, I mapped the distribution of deep-seated landslides using light detection and ranging (LiDAR) derived maps. Landslide density increases in regions subject to late Pleistocene – Holocene channel incision and particularly in response to lateral incision at the apex of meander bends.

Wavelet analysis of channel sinuosity reveals hillslopes are most sensitive to meander wavelengths of 1.5 km.

Argillaceous lithology generates abundant earthflow activity along the main stem Eel River, yet spatial and temporal patterns of earthflow movement are poorly understood. I undertook a detailed study of the Kekawaka Earthflow using LiDAR, meteoric ^{10}Be in soil, orthorectified historical aerial photographs, and field surveys. Inventories of ^{10}Be in soil pits increase systematically downslope, indicate an average movement rate of 2.1 ± 1.3 m/a over the past 150 years, and establish a minimum earthflow age of 1700 years. The Kekawaka earthflow has a systematic history of movement, both spatially, with greatest movement in the narrow transport zone, and temporally, as velocities peaked in the 1960's and have slowed since 1981.

I used LiDAR and aerial photographs to map earthflow movement and calculate sediment flux across 226 km^2 of the main stem Eel River. From 1944 – 2006, 7.3% of the study area was active, and earthflows account for an erosion rate of 0.53 ± 0.04 mm/a, over half the regional average sediment yield. Velocity time series on 17 earthflows suggest temporal earthflow behavior is influenced by decadal-scale changes in precipitation, temperature, and river discharge, although local topographic factors can overwhelm this climatic signal. When active, earthflows erode an order of magnitude faster than surrounding terrain; however, source supply limitations appear to govern long-term earthflow evolution.

This dissertation includes previously published coauthored material.

CURRICULUM VITAE

NAME OF AUTHOR: Benjamin H. Mackey

PLACE OF BIRTH: Blenheim, New Zealand

GRADUATE AND UNDERGRADUATE SCHOOLS ATTENDED:

University of Oregon
University of Canterbury

DEGREES AWARDED:

Doctor of Philosophy, 2009, University of Oregon
Bachelor of Science (1st Class Honours – Geological Sciences), 2003, University of Canterbury
Bachelor of Laws (1st Class Honours), 2002, University of Canterbury

AREAS OF SPECIAL INTEREST:

Landscape Evolution
Tectonic Geomorphology
Landslides and Natural Hazards

PROFESSIONAL EXPERIENCE:

Graduate Teaching Fellow, University of Oregon, 2004–2009

GRANTS, AWARDS AND HONORS:

Fulbright–EQC Graduate Award in Natural Disaster Research, Fulbright New Zealand, 2004

University Prize in Science, University of Canterbury, 2003

PUBLICATIONS:

Mackey, B.H., Roering, J.J., and McKean, J.A., 2009, Long-term kinematics and sediment flux of an active earthflow, Eel River, California: Geology, v. 37, p. 803-806.

ACKNOWLEDGMENTS

Foremost thanks to my advisor, Josh Roering, who guided me through the trials and adventures of graduate school, and has been an inspiration to work with. Josh was always generous with time and resources, has opened my eyes to the fascinating world of quantitative geomorphology, all the while retaining a sharp sense of humor and great outlook on life. I can only hope some of your insight and skill as a scientist has rubbed off on me over the past five years. I am similarly grateful to Jim McKean and Jarg Pettinga for fostering my interest in geomorphology as an undergraduate in New Zealand, and for continued advice, counsel, and encouragement during my time at Oregon.

The graduate students at Oregon have ensured time in Eugene has been both thoroughly enjoyable and academically stimulating; whether in formal group discussion, a Friday evening at Rennie's, or around a campfire in the Cascades. Special thanks to the fellow students, past and present, in Josh's Earth Surface Processes Laboratory. Additionally, I remain indebted to the Geological Sciences faculty and administrative staff for their continued help, advice, and accessibility.

This research was funded by an NSF Grant (EAR-0447190) to J. Roering, and a NASA Earth Surface and Interior Program grant to J. Roering and D. Schmidt (UO). I had additional support via the 'Fulbright EQC award in Natural Disaster Research' from Fulbright and the Earthquake Commission in New Zealand.

The LiDAR data of the South Fork Eel River analyzed in Chapter II was provided by the National Center for Earth-surface Dynamics. Thanks to Peter Steel and the Angelo Coast Range Reserve for access. Sean Bemis and Belle Philibosian helped prepare radiocarbon samples. The main stem Eel River LiDAR data underpinning Chapters III and IV was acquired by the National Center for Airborne Laser Mapping. John Stone, Greg Balco and the University of Washington Cosmogenic Isotope Laboratory provided invaluable advice and assistance with meteoric ^{10}Be processing. I am especially grateful to Calvin and Wendy Stewart of Stewart Ranch for field access, advice, and generous hospitality over the past several years. Additional field access along the Eel River was provided by Lone Pine Ranch and Mr. Ted Winters. Sean Bemis, Adam Booth and Laura Stimely provided assistance with field surveying. I thank Humboldt County Public Works, Six Rivers National Forest, USGS, and the libraries at Humboldt State University and UC Berkeley for help with accessing aerial photos. Discussions with Harvey Kelsey and Jay Stallman enhanced our understanding of this spectacular landscape.

None of this would have been possible without the encouragement of my extended family and friends in New Zealand, and new friends I have made in the US. Eternal thanks to my parents, Ian and Lachlan, and sisters, Sarah and Rachael, who have been unwavering in their support during my time at both Canterbury and Oregon. Finally, many thanks to Austin for your all you have done over the past year.

For Jim and Nancy

TABLE OF CONTENTS

Chapter Page

Chapter Page

LIST OF FIGURES

Figure Page

LIST OF TABLES

CHAPTER I

INTRODUCTION

A major contemporary focus in the geosciences is the study of earth surface processes, with the objective of providing quantitative explanations and predictions for how environmental perturbations may affect surface processes. This focus encompasses the processes of erosion in the broadest sense – where and how sediment is produced, the rate and mechanics of transport through the fluvial system, and how it is delivered to floodplains, the coastal environment, and ultimately the ocean depths. Beyond simply dictating the physical appearance of a landscape, surface processes exert primary controls on hydrocarbon and mineral genesis and storage, the locations of arable land, building sites and transport corridors, and can pose significant natural hazards through flooding and landslides. In particular, significant effort is directed at constraining how surface processes were affected by the climates of the past, and crucially, how they will be affected by future climate changes.

For much of the twentieth century, the study of earth surface processes was largely qualitative. Researchers were concerned with descriptions of landscapes (Chorley et al., 1991), and influenced by pioneering works such as Davis (1899) and Penck (1953). In recent decades however, aided by significant advances in computing, geochronology, and geodesy, there has been a shift towards a more quantitative understanding of the mechanics and rates of processes, so that we can better predict landscape form and dynamics (Dietrich et al., 2003). For many surface processes, such as soil production, slope dependent soil creep, and river incision, researchers have developed field verified and physically testable mathematical statements that can quantify both the mass flux

(erosion) attributable to a surficial processes, and the resulting landscape morphology. When parameterized in this way, a given surface process can be incorporated into powerful numerical landscape evolution models, which are used to test fundamental theories about how the earth surface evolves (e.g., Perron et al., 2009).

In non-glaciated mountainous landscapes, sediment production and hillslope form are controlled by mass wasting processes, such as landslides and earthflows. Beyond their popular notoriety as a formidable natural hazard, landslides exert a considerable influence on the supply rate, grain size, and timing of sediment to the channel network and morphology of the landscape. Landslides and earthflows have proven challenging to analyze using the quantitative framework described above, as they do not occur predictably in time or space, and range in size from local stream bank collapse to mountain-scale slope failure. Given these difficulties, landslide processes are frequently overlooked in models of landscape evolution, and none account for slow sustained mass-movement such as earthflows (Dietrich and Perron, 2006).

Research into deep-seated landsliding typically focuses either on detailed engineering-style studies of individual slides, or broad regional landslide inventories (Malamud et al., 2004). Earthflow studies have adopted a narrower focus, with research directed almost exclusively on seasonal slide mechanics (e.g., Coe et al., 2003; Iverson and Major, 1987), and we know little of earthflow behavior beyond individual slopes, or at timescales exceeding a decade (cf. Bovis and Jones, 1992; Kelsey, 1978; Maquaire et al., 2003; Trotter, 1993). Consequently, we struggle to quantify the sediment yield, morphology and dynamics of an earthflow prone landscape.

With this motivation, I seek to quantify the factors which influence deep-seated slope instability and modulate sediment yield. I address a need for extensive, detailed maps of mass movement, which capture landslide and earthflow behavior over significant spatio-temporal scales. Specifically, I investigate how and why deep-seated landslide and earthflow movement varies in time and space, with a particular focus on large, slow moving earthflows in the Eel River catchment of northern California. Methodologically, I

underpin the research presented in the next three chapters with high-resolution digital topography acquired via airborne light detection and ranging (LiDAR).

The upper South Fork Eel River has experienced sustained incision since the late Pleistocene, as reflected in extensive strath terraces and abundant ancient, deep-seated landslides (Seidl and Dietrich, 1992). In Chapter II, I document the landslide response to this incision, and map the spatial distribution of landslides, terraces and channel incision. I observe extensive landsliding in the incised section of the river, although the amount of landsliding does not scale with the magnitude of incision, but rather reflects the progressive hillslope evolution of up to 80 m of sustained incision. The lateral migration of the channel within the valley also exerts a strong influence on landslide location, which typically cluster at the outer edge of meander bends. Wavelet analysis of channel sinuosity reveals that landslides are most sensitive to meanders with a wavelength of 1.5 km. This chapter provides rare field data on landslide response to channel incision, a commonly assumed by seldom quantified process. Chapter II was co-authored with Josh Roering, Jim McKean and Bill Dietrich.

Extensive argillaceous mélange along the main stem Eel River generates abundant slow-moving landslides spanning all states of activity and form, from small <100 m^2 slumps, to huge earthflow complexes spanning 900 m of relief and extending up to 5 km from channel to ridge (Brown and Ritter, 1971; Dwyer et al., 1971). Chapter III describes a study of the 1.5 km long Kekawaka earthflow. This project was designed to better understand long-term earthflow activity and evolution, and I incorporate LiDAR, orthorectified aerial photographs, field survey data, and a novel application of meteoric ^{10}Be in soil pits to measure earthflow displacement. Inventories of meteoric ^{10}Be increase systematically downslope, indicate an average movement rate of 2.1 ± 1.3 m/a over the past 150 years, and establish a minimum earthflow age of 1700 years. Orthorectified aerial photos show earthflow velocities peaking in the 1960's at 3–4 m/a. I calculate a 20th Century erosion rate approaching 10 mm/a, 10–20 times greater than the estimated regional sediment yield over that period. This study emphasizes the variability of earthflow movement at the decadal scale, and the localized and vigorous role of active

earthflows in landscape evolution. Chapter III was published in the journal *Geology* in September 2009, volume 37(9), pages 803–806, and co-authored with Josh Roering and Jim McKean.

Chapter IV, co-authored with Josh Roering, describes a regional study of large, slow moving earthflows in the Eel River catchment. A 226 km^2 LiDAR dataset and a series of orthorectified aerial photos enables documentation of 122 individual active earthflow features, including 17 large (>1.5 km long) failures with sufficient displacement (>30 m) to generate a time series of earthflow movement. Over the period 1944–2006, 7.3% of the terrain was active, and earthflows account for a 0.53 ± 0.04 mm/a erosion rate across the study area, over half the regional average sediment yield. I suggest that when active, earthflows erode an order of magnitude faster than surrounding terrain, however source supply limitations appear to govern long term earthflow evolution. The displacement data, determined by systematically tracking the position of shrubs growing on earthflow surfaces, cluster into 3 distinct temporal patterns. One group exhibits peak velocities from 1944 to 1964 with little subsequent movement, while a second group of earthflows sustain rapid velocities of ~4m/a until the late 1970's. The third group shows slow steady movement (~1 m/a), with occasional surges. The temporal patterns of movement correspond with decadal-scale climatic changes recognized as the recent cool-warm cycle of the Pacific Decadal Oscillation (1947–2008). I document persistently cooler, wetter conditions from 1950 to the late 1970's, synchronous with the majority of earthflow movement.

CHAPTER II

DEEP-SEATED LANDSLIDES AND HILLSLOPE BASE LEVEL CONTROL: SPATIAL ANALYSIS USING AIRBORNE LIDAR MAPPING

This chapter is in preparation for submission to *Journal of Geophysical Research – Earth Surface*. This paper is co-authored with Josh Roering, who provided funding and advisorial help. Josh Roering, Jim McKean and Bill Dietrich provided editorial support.

1. Introduction

1.1. Landslides and Landscape Evolution

Deep-seated landsliding is a dominant erosional process in the evolution of mountainous landscapes – landslides can impart large perturbations on sediment budgets, establish or modify drainage patterns, and alter hillslope morphology [*Hovius et al.*, 1998; *Korup*, 2005b; *Korup*, 2006a]. Despite the significance of deep seated landslides to landscape evolution, when compared to other erosional processes (eg river incision, soil production, or slope dependent soil creep), we continue to be challenged when attempting to predict the landscape form and sediment flux associated with large slope failures [*Dietrich and Perron*, 2006]. Much of this knowledge gap can be attributed to the stochasticity of landslide behavior. Difficulties arise when extrapolating geomechanical theories beyond an individual hillslope to the landscape scale, where the hillslope

material properties, vegetation, destabilization processes, rate of base level change, and triggering factors (meteorological and seismic events) are inherently spatially and temporally variable [*Dietrich et al.*, 2003; *Palmquist and Bible*, 1980].

Many geotechnical and engineering investigations document the behavior and characteristics of individual landslides, yet comparatively few studies have explored the erosional and morphologic role of deep-seated landslides in a context significant to geomorphic temporal and areal scales. Such an approach, for example, would look to explain where and when landslides occur within drainage basins [*Densmore and Hovius*, 2000; *Hovius et al.*, 1998; *Korup*, 2005b; *Palmquist and Bible*, 1980], and ultimately their contribution to sediment flux and impact on landscape morphology [*Densmore et al.*, 1998; *Hovius et al.*, 2000; *Meunier et al.*, 2007; *Ouimet et al.*, 2007; *Roering et al.*, 2005].

1.2. Channel Incision

Because river incision sets the pace of erosion in non-glaciated landscapes [e.g., *Whipple*, 2004], and deep-seated landslides ultimately respond to changes in base level via channel incision, increased understanding of the nature of coupling between the channel and deep-seated landslides may help us predict the geomorphic impact of such landslides (such as their size, location and timing) after a given channel perturbation. Alternatively, we would not expect landslides generated by other factors, such as earthquakes, to show a strong signal of coupling with the channel, as they preferentially occur on ridges where seismic accelerations are greatest [*Densmore and Hovius*, 2000; *Meunier et al.*, 2007]. In landscapes prone to deep-seated slope failure, landsliding should occur following channel incision, although the response may not be immediate as stress and/or strength changes may require time to propagate upslope. Physical models give some insight into the extent to which landslide behavior is coupled to channel incision [*Densmore et al.*, 1997; *Hasbargen and Paola*, 2000]; however, catchment-scale deep-seated landslide response to channel incision remains poorly documented in real landscapes [cf. *Azanon et al.*, 2005; *Griffiths et al.*, 2005; *Hovius et al.*, 2000; *Hovius et al.*, 1998; *Ouimet et al.*, 2007].

It is well established that river incision can cause hillside strength to decrease, and/or shear stresses within adjacent slopes to increase, leading to slope failure [*Terzaghi*, 1950]. An important, but often elided consideration in many studies of river incision is that rivers do not just incise vertically – lateral river incision will similarly increase stresses on adjacent hillslopes. As a simple example, on a slope of 45°, 1 m of lateral incision is effectively the same as 1 m vertical incision. Lateral incision can occur more rapidly, and will be preferentially imposed on the outside of meander bends [*Stark*, 2006]. This pattern has been observed with small historical landslides clustering on the outer edge of meander bends due to fluvial undercutting [*Hugenholtz and Lacelle*, 2004].

Although deep-seated slope failure in response to lateral channel incision may seem axiomatic, and specific examples have been well documented [e.g., *Kelsey*, 1978], it has rarely been systematically quantified throughout a landscape. There is insufficient data to test theories relating the locations of deep seated landslides to progressive incision, and no studies have assessed landslide response to varying scales of channel curvature. We are not equipped to answer fundamental questions regarding how hillslopes respond to a channel undergoing sustained incision. For example, is a channel with a very short wavelength and tighter transient meanders more effective at generating slope instability than river with longer wavelength, less-mobile meanders? How do landslide prone slopes evolve under sustained channel incision?

With research focused largely on contemporary landslide movement, there is little theory about what happens to a slope following failure [*Mather et al.*, 2003], or how the slope might evolve through a series of landsliding episodes [*Cendrero and Dramis*, 1996]. Given the long time scales of slope evolution, and the difficulty of reconstructing pre-failure morphology, the process of slope failure in response to sustained channel incision has not been well quantified.

1.3. Testing Landslide Response to Channel Incision

We focus on one particular hillslope erosion process, mass wasting through deep-seated (bedrock) landslides in geotechnically weak meta-sedimentary rocks, and ask a

first order question: does the location of landslides correspond with recent channel incision, as recorded by strath terraces? As a null hypothesis, we assume landsliding along the channel has no systematic pattern. To test this, we employ light detection and ranging (LiDAR) to document the spatial pattern of landsliding and strath terraces along the South Fork (SF) Eel River, Northern California. We explore whether the extent and location of landsliding correlates with the relative magnitude and lateral directivity of channel incision.

2. South Fork Eel River, California

We used ~200 km^2 of LiDAR data (average bare earth data density about 2.6 m^{-1}, gridded to 1 m resolution) encompassing the upper South Fork Eel River catchment in northern California, centered on the Nature Conservancy's Angelo Coast Range Reserve (Figure 1a,b). The area has a Mediterranean climate, and vegetation comprises a mixture of redwood, fir and oak forest. The lithology, summarized in Figure 2a, consists of the Central and Coastal Belts of the Franciscan Complex [*Jayko et al.*, 1989], a Jurassic–Cretaceous accrectionary prism complex renowned for its susceptibility to deep seated landsliding [*Iverson and Major*, 1987; *Kelsey*, 1978]. Tectonically, the Neogene-to-present migration of the Mendocino Triple Junction along the coast of northern California has generated a double humped zone of uplift which migrates north at approximately 5 cm/yr [*Furlong and Schwartz*, 2004]. This manifests in the landscape as transient changes in uplift rates and regional-scale catchment reorganization [*Lock et al.*, 2006].

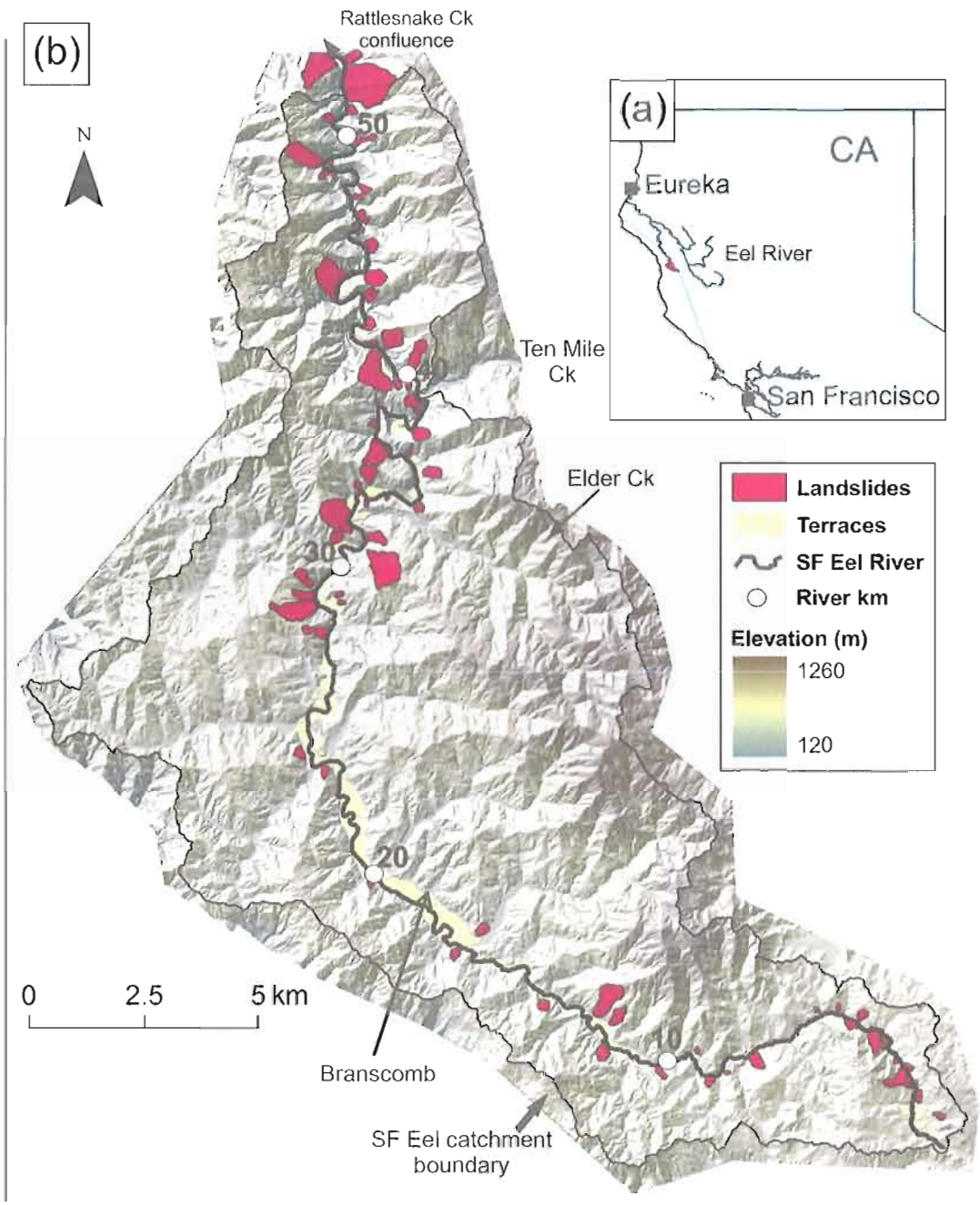

Figure 1. Location map of northern California and study site. (a) Eel River system and the area of LiDAR coverage in the headwaters of the SF Eel River catchment. (b) Shaded relief map of the Lidar coverage illuminated from the NW. SF Eel River (black line) runs south to north. Mapped deep seated landslides (red) and SF Eel River terraces (yellow) are indicated. Mapping was confined to the slopes bounding the SF Eel River. White circles mark every 10 km of channel distance.

From the late Pleistocene to the present, the SF Eel River has experienced several periods of incision, recorded by multiple levels of strath terraces that typically converge upstream [*Fuller et al.*, 2009; *Seidl and Dietrich*, 1992]. To approximate the relative depth of incision along the SF Eel River, we focus on a distinctive upper strath terrace (locally equivalent to Terrace 3 in *Seidl and Dietrich* [1992]) whose apparent remnants can be traced for approximately 30 km along the river profile (top of green shading in Figure 2a). Optically stimulated luminescence dating on gravels at the base of this terrace tread (river km 32.5) gives an age of 20.5 ± 3.3 kyr [*Fuller et al.*, 2009], which equates to a bedrock incision rate of 0.3–0.4 mm/yr. *Fuller et al.* [2009] use ^{10}Be in terrace gravels to show catchment averaged erosion rates were higher in the late Pleistocene than the Holocene. They invoke increased deep seated landslide activity to explain these higher erosion rates, and suggest elevated levels of sediment supply armored the channel and promoted strath planation.

Incision into the strath terraces extends approximately half way up our study reach, and invites comparison of landslide distribution between the un-incised (0–26 km) and incised (26–53 km) sections of channel. Abundant dormant deep-seated landslide features are preserved throughout the upper SF Eel catchment [*Lashermes et al.*, 2007], as evident in Figures 1 and 7. There is minimal evidence of modern deep-seated activity, such as ground fissures or bowed trees.

The landslides along the SF Eel River span a range of failure styles from large deep-seated rotational slumps, slump-flows, to complex, multi-part earthflows. Some ridges exhibit Sackung or antiscarp features illustrating the large-scale slope instability. Due to the predominance of the slump failure style, on many slides the landslide mass has not been completely eroded, and persists as a restabilized mass or bench below the headscarp. We frequently observe extensive channel or gully incision and subsidiary slumps on the landslide deposit. One section of the river (41–50 km) differs, in that many of the landslides deposits have been eroded, to expose the approximate landslide failure surface.

Excavations and creek exposures reveal the landslide material as a very poorly sorted, largely unstructured colluvium, with individual clasts up to tens of meters per side. Overlying the landslide deposits are mature redwood and fir forests, which presumably favor the deep soils and favorable groundwater conditions afforded by the landslide mass. The depth to the failure plane is unknown, although given scaling relationships between slide area and volume [*Hovius et al.*, 1997; *Malamud et al.*, 2004], potentially ranges from 4 to 50 m.

As the slides are currently largely inactive, modern conditions may not be conducive to promoting deep seated slope failure. This lack of modern activity is plausibly attributable to various factors, including a dryer climate, a change in the rate or directivity of channel incision, changed seismic regime, or the establishment of the dense redwood and conifer forest in the late Holocene [*Barron et al.*, 2003; *Pisias et al.*, 2001]. Alternatively, the landslides may reflect previous perturbations, such as a rapid period of channel incision.

3. Methods

3.1. Geomorphic Mapping

High-resolution LiDAR data enables us to map landslides and quantify the spatial relationship between landslides and river channels across large areas. The pervasive landslide features throughout the SF Eel River catchment are problematic to map conventionally: dense conifer forests obscure slide features, and surficial erosion acts to attenuate and modify the characteristic landslide morphology [*Wieczorek*, 1984; *Wills and McCrink*, 2002]. The 'bare-earth' digital elevation model (DEM) generated by LiDAR therefore serves as an efficient and effective tool to map subtle landslide features across an extensive, mostly forested catchment [*Van den Eeckhaut et al.*, 2007].

We concentrated our analysis on the upper 53 km of the SF Eel River (extent of LiDAR coverage – Figure 1b), and delineated the margins of landslide features located on hillslopes bounding the river. Our mapping did not extend up tributary drainages;

tributaries frequently have a knickpoint or channel step at the tributary junction, and thus do not experience the same extent of channel incision as the SF Eel River. We digitized landslide boundaries guided by slope, contour, drainage area, surficial roughness [*McKean and Roering*, 2004] and variably-rendered shaded relief maps via characteristic landslide morphologic features including headscarps, benches, undrained depressions, toe boundaries, drainage patterns, and residual hummocky slide mass deposits [*Cruden and Varnes*, 1996]. Terrain not affected by deep-seated landslides is generally restricted to the inside of meander bends. This terrain typically has steep, well organized 'ridge and valley' topography, conventionally associated with incision by debris flows [*Stock and Dietrich*, 2006], distinguishable from the hummocky, low drainage density terrain attributed to deep-seated landsliding [e.g., *Roering et al.*, 2005]. We caution that mapping ancient deep-seated landslides in highly erodible mélange terrain, even from high-resolution LiDAR-derived DEM's, remains an interpretive exercise [*Van Den Eeckhaut et al.*, 2005] and acknowledge that this is the most subjective aspect of our methodology.

We grouped slide scarps and masses for each landslide within a single polygon, and mapped complex slides as one contiguous feature. Similarly, we mapped individual terrace treads from the flights of terraces flanking the SF Eel River, and visited dozens of landslide and terrace sites in the field to verify correct feature classification. A geographical information system (GIS) generated areal and elevation statistics for each of the landslide and terrace polygons, and we projected mapped landslides and terraces to the channel longitudinal profile, as shown in Figure 2a-c. We quantify the pattern of terraces both in the context of height above the river (terrace elevation as the median elevation of the individual terrace polygon), and in terms of bank-dependent average terrace width down the channel (Figure 2b). Additionally, in Figure 2 we distinguish landslides which impinge on the modern SF Eel River from those landslides which do not interact with (and are disconnected from) the modern channel (e.g. landslides higher on hillslope or adjacent to a terrace).

Figure 2. South Fork Eel River longitudinal profile, landslides, terraces and sinuosity. Figure 2a-d is displayed as a function of distance (km) along the SF Eel River.

(a) Stream profile of the SF Eel River. Terraces of the SF Eel River are denoted by horizontal dashes, with elevation the median elevation of a terrace polygon. The region shaded green from ~26 km represents vertical incision into the upper strath surface. Landslides are projected onto the stream profile, and are represented by vertical bars related to elevation range, while the circle at the top indicates relative landslide size, with the largest 0.817 km^2 at 51 km. Slides colored red have potential interaction with the modern SF Eel channel, whereas those colored grey are disconnected. We summarize the lithology transected by the SF Eel along the base [Jayko et al., 1989].

(b) Individual terrace surfaces were projected to the channel and area binned every 500 m of channel length. Terraces greater than 500 m in length were compartmentalized and projected in pieces. Positive area is the left bank, and negative area the right bank. Approximate incision into the upper strath surface is shown in green. Note the anti-correlation between terraces and landslides from 12-27 km.

(c) All landslides are projected to the SF Eel channel. A positive area represents the slides on the true left bank, a negative area those on the right, with the same coupling coloring described in 2a. The curves are the coefficients of the 1.5 km (solid) and 6.2 km (dashed) wavelets, used to approximate planform curvature at different scales. The box denotes the section of channel depicted in Figure 7.

(d) Average slope (degrees) ± 1 standard deviation of hillslopes bounding the SF Eel River. All terrace surfaces were excluded from slope calculations.

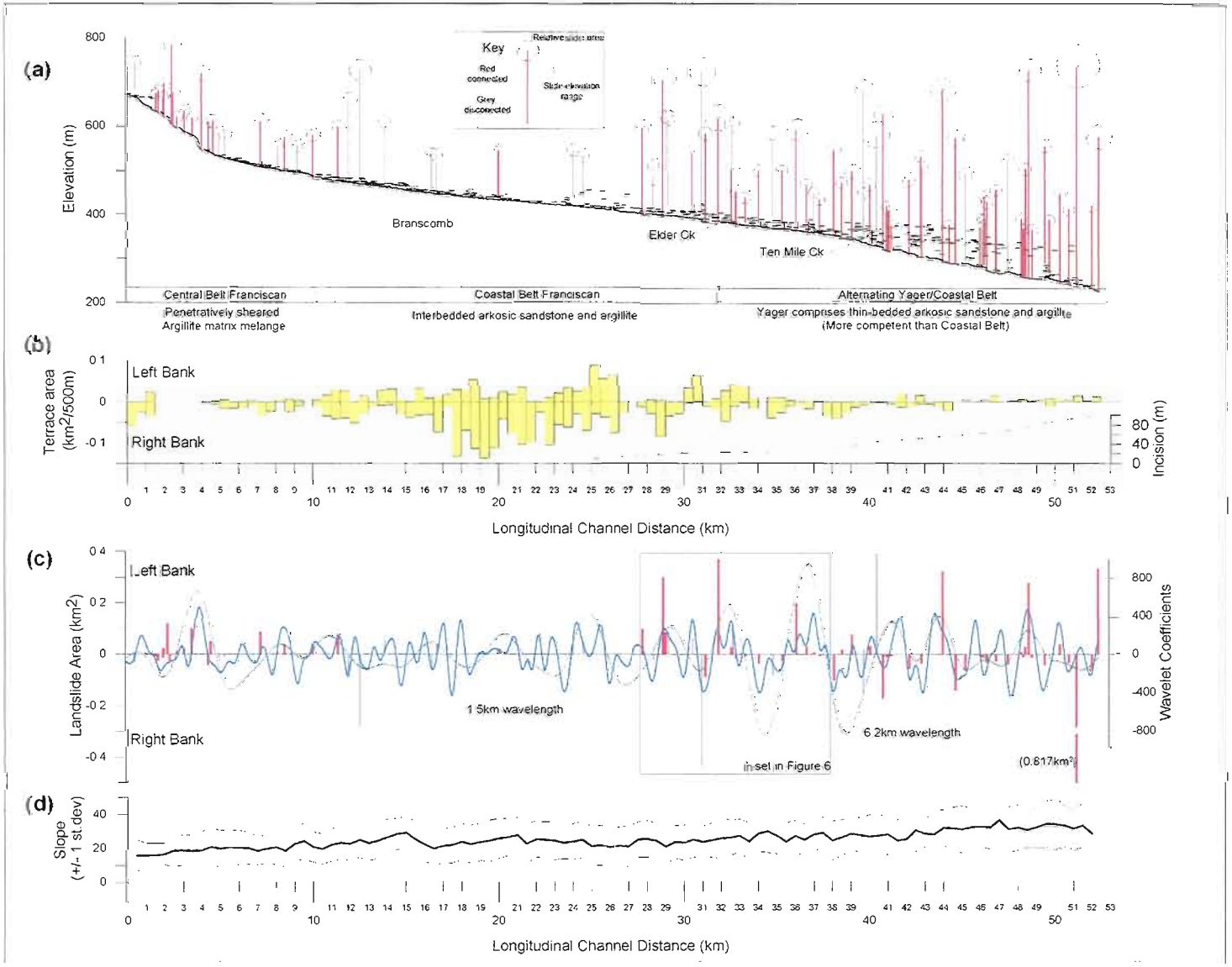
(a)
Elevation (m)
800
600
400
200
Key
Red connected
Grey disconnected
Relative slide area
Slide elevation range
Branscomb
Elder Ck
Ten Mile Ck
Central Belt Franciscan
Penetratively sheared Argillite matrix melange
Coastal Belt Franciscan
Interbedded arkosic sandstone and argillite
Alternating Yager/Coastal Belt
Yager comprises thin-bedded arkosic sandstone and argillite (More competent than Coastal Belt)
(b)
Terrace area (km2/500m)
0.1
0
-0.1
Left Bank
Right Bank
Incision (m)
80
40
0
0
10
20
30
40
50
Longitudinal Channel Distance (km)
(c)
Landslide Area (km2)
0.4
0.2
0
-0.2
-0.4
Left Bank
Right Bank
1.5km wavelength
6.2km wavelength
Inset in Figure 6
(0.817km2)
Wavelet Coefficients
800
400
0
-400
-800
(d)
Slope (+/- 1 st.dev)
40
20
0
0
10
20
30
40
50
Longitudinal Channel Distance (km)

3.2. Wavelet analysis of channel sinuosity

In quantitative geomorphology, wavelet analysis has been used to analyze changes in river corridor width [*Gangodagamage et al.*, 2007], morphological roughness of landslides [*Booth et al.*, 2009], and longitudinal variation in thalweg depth [*McKean et al.*, 2008]. Here we use wavelets to characterize scales of planform river curvature. For our purposes, wavelet analysis has advantages over other signal processing techniques (e.g., Fourier transform) in that frequency and time data can be obtained simultaneously (although here we substitute time for channel distance). Wavelet analysis enables us to examine channel curvature patterns over a variety of wavelengths at all sections of the channel, in order to determine the scale of channel sinuosity that best correlates with the along-channel distribution of landsliding.

We constructed a channel path for the SF Eel River by routing water down the path of steepest descent. From this profile, we sampled points every 20 m along the thalweg of the SF Eel River (Figure 1), and connect successive points with a chord of azimuth θ (Figure 3). We calculated the change of direction ($\Delta\theta$) between successive chords to generate a series of direction change $\{\theta\}$, described as $\Delta\theta_i = \theta_i - \theta_{i-1}$ [*Ferguson*, 1975], and defined positive change as a clockwise rotation. We added each successive angle of direction change to the sum of the previous, to generate a record of cumulative change in deflection. We used a very stiff smoothing spline to de-trend the regional planform curvature from the signal and undertook wavelet analysis on the residuals of the signal of cumulative change in deflection (Figure 3) to find characteristic wavelengths of sinuosity.

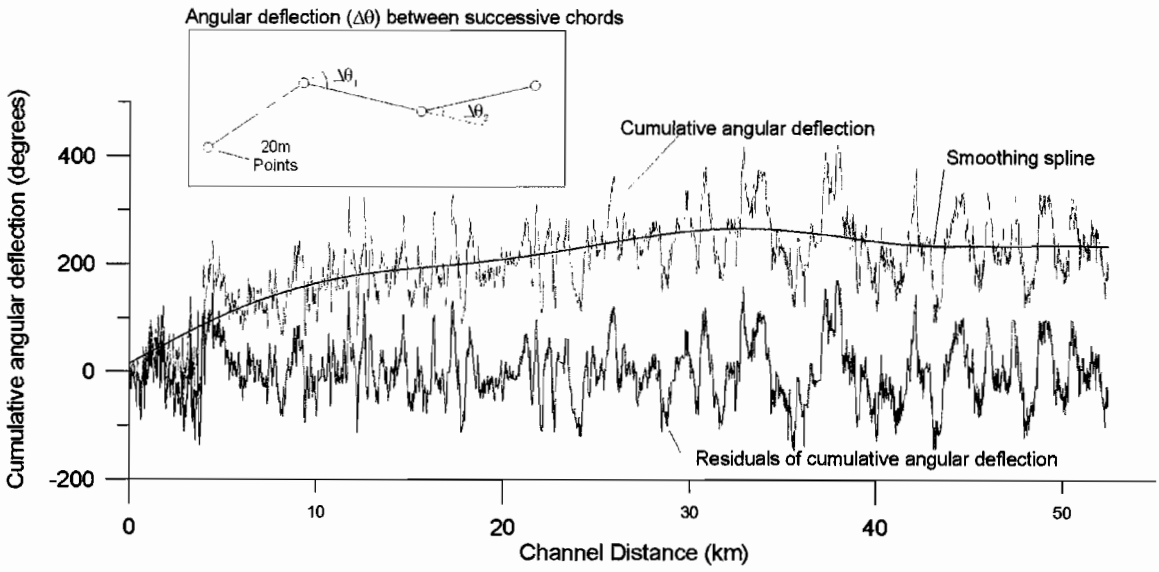

Figure 3. South Fork Eel River cumulative angular deflection and residuals. Inset diagram shows angular deflection ($\Delta\theta$) between chords constructed from points every 20 m of channel length. Cumulative angular deflection ($\sum \Delta\theta$ - grey line) with spline fit (Lambda = 10^{13}). Note how the trend mimics the channel planform in Figure 1a. The residuals of spline fit (black) remove the regional channel curvature, and we analyze this signal with wavelet analysis.

Using a first order Gaussian wavelet (Figure 4), we analyzed the residual direction change data (Figure 3) with a 1-D continuous wavelet transform. Figure 5 details how the wavelet captures channel sinuosity. Compared with other conventional wavelet shapes, the simple and smoothly varying form of the Gaussian (Figure 4) best approximates the form of a planform channel 's-bend'. To relate wavelet length-scale (amount of dilation of the wavelet) to the sampling period of the signal (Δ, the 20 m sampling interval) and therefore back to channel length, we calculated the 'center frequency' (F_c) and corresponding 'pseudo period' (T_a) of the Gaussian wavelet as illustrated in Figure 4 [*Abry*, 1997; *Zhou*, 2003]. The center frequency is the frequency maximizing the Fourier transform of the mother wavelet, and equates to 0.2 signal units for the 1st order Gaussian. F_c is related to pseudo-frequency (F_a) at a given scale or dilation of the wavelet (a) and sampling period (Δ) by the relationship:

$$F_a = \frac{F_c}{a \cdot \Delta} \tag{1}$$

Finally, the pseudo period, T_a, is simply the inverse of F_a. For example, in our analysis a wavelet scale (a) of 20, stretches the wavelet over 200 signal units, or 4 km of longitudinal channel length with $\Delta = 0.02$ km. The a of 20 and Fc of 0.2 generates a pseudo frequency of 0.5 km^{-1}, and pseudo-period (or wavelength) of 2 km. The pseudo-period relates to channel distance as the wavelength of an idealized planform s-bend, and is how we henceforth quantify and term wavelet length scale. We stress this is a different definition to the conventional definition of wavelength, being the direct distance between similar points on the waveform.

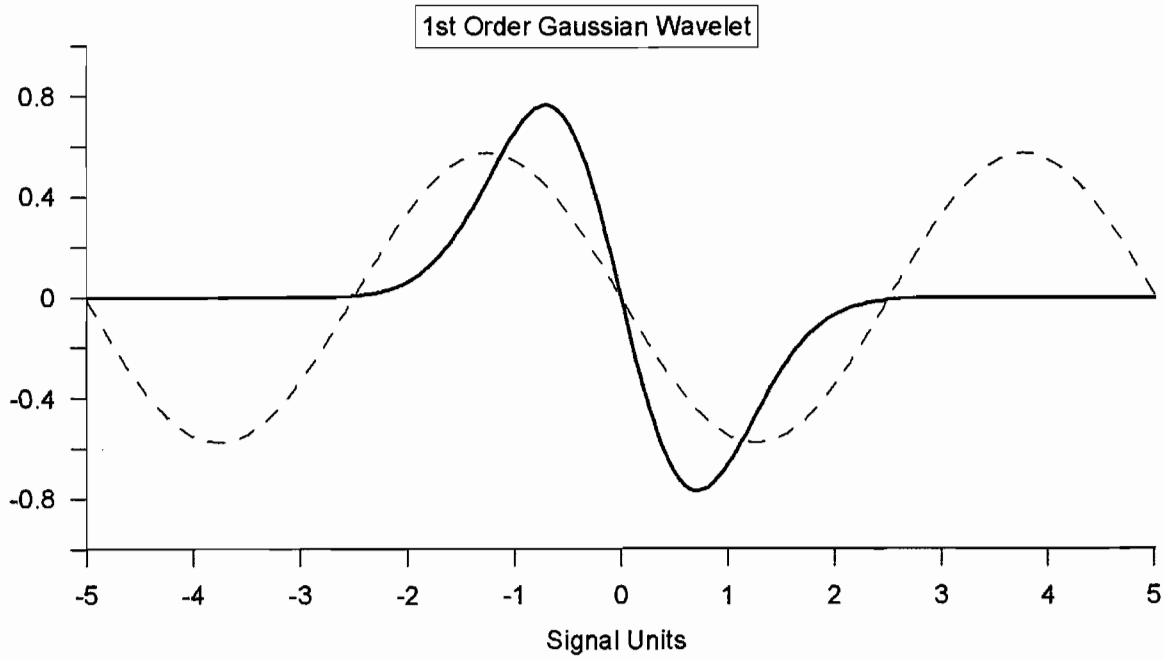

Figure 4. First order Gaussian wavelet (solid line - effective support [-5, 5]). The center frequency based approximation has a frequency of 0.2, and pseudo-period of 5 (dashed line). We appropriate pseudo-period as the channel length of an 's-bend' at a given wavelet scale.

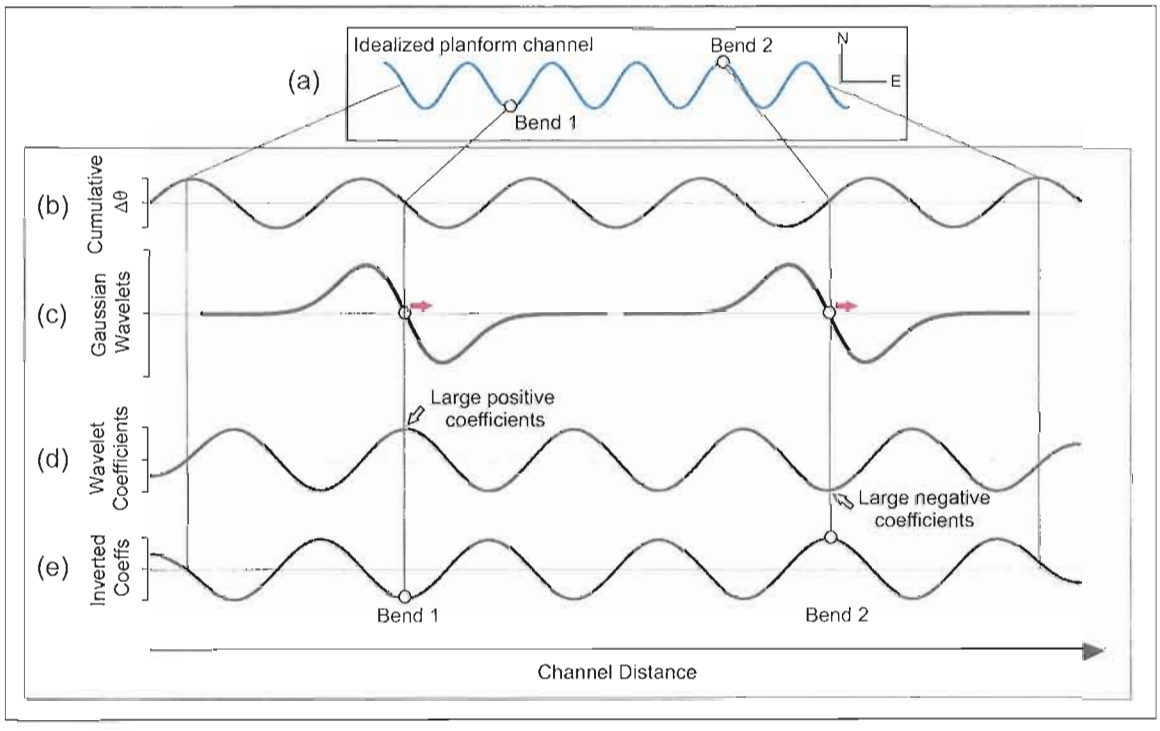

Figure 5. Representation of how we use wavelets to capture channel sinuosity, illustrated at two channel bends. 5a is in map view, whereas the x-axis of plots 5b-e is channel distance.

(a) Planform view of an idealized sinuous channel, with 2 opposite bends highlighted.

(b) Plot of cumulative change in direction between successive chords (degrees) along the channel. At the apex of a meander bend, the rate of change in direction is greatest, and these points correspond with inflection points on this plot of cumulative $\Delta\theta$.

(c) The wavelet calculates coefficients at all points along the channel, but here we show a representation of the wavelet at 2 points correlating to the two channel bends from 5a. At Bend 1 the left wavelet is in phase with the cumulative azimuth signal and returns high coefficients, whereas at Bend 2 the wavelet is out of phase and returns large negative coefficients

(d) Coefficients of the wavelet transform – note the high coefficients relating to the apex of bends, such as at Bend 1 and Bend 2.

(e) Due to the way we defined directionality (clockwise channel turn positive), the wavelet coefficients finally need to be inverted to give a representation of the channel sinuosity at a given wavelet length scale.

Large absolute wavelet coefficients indicate that the local river planform is well approximated by the Gaussian wavelet at the designated wavelet length scale. Positive wavelet coefficients (clockwise river bend) correlate with positive (true left bank) landslide area, and vice versa (Figure 6). To determine which scale of sinuosity best correlates with the along channel distribution of landsliding, we cross-correlated wavelet coefficients with bank dependent landslide area for a range of wavelet length-scales. We excluded the slide at 52 km from the correlation as its large size exerted too much influence on the regression. We analyzed both the whole channel length, and the un-incised (0–26 km) and incised sections (26–53 km) separately. While it is ambitious to expect a linear relationship between coefficients and landslide area, if landslides do cluster on the outer edge of meander bends we would expect points to plot in opposite quadrants, as shown conceptually in Figure 6. The top right quadrant relates to landslides on the left bank, and clockwise river bends, whereas landslides on the right bank and anti-clockwise river bends will fall within the lower left quadrant. Linear regression is a simple way to quantify the clustering of points in the opposite quadrants, even though the correlation coefficients are generally low.

4. Results

4.1. Distribution of Landsliding

We mapped 87 deep-seated landslide features along the 53 km length of the SF Eel River as shown on Figures 1 and 2. Along 0–26 km, we identified 29 landslides, which have an average area of 0.047 km^2. There is a notable concentration of landslides from 0 to 10 km where the SF Eel crosses the highly erodable Central Belt of the Franciscan Complex (Figure 2a). In contrast, along 11–27 km, there are only 9 mapped landslides, and this section coincides with low channel gradient, and extensive broad terraces. From 26 to 53 km, the section of the profile with evidence of channel incision, we mapped 58 deep seated landslides, with an average area of 0.096 km^2.

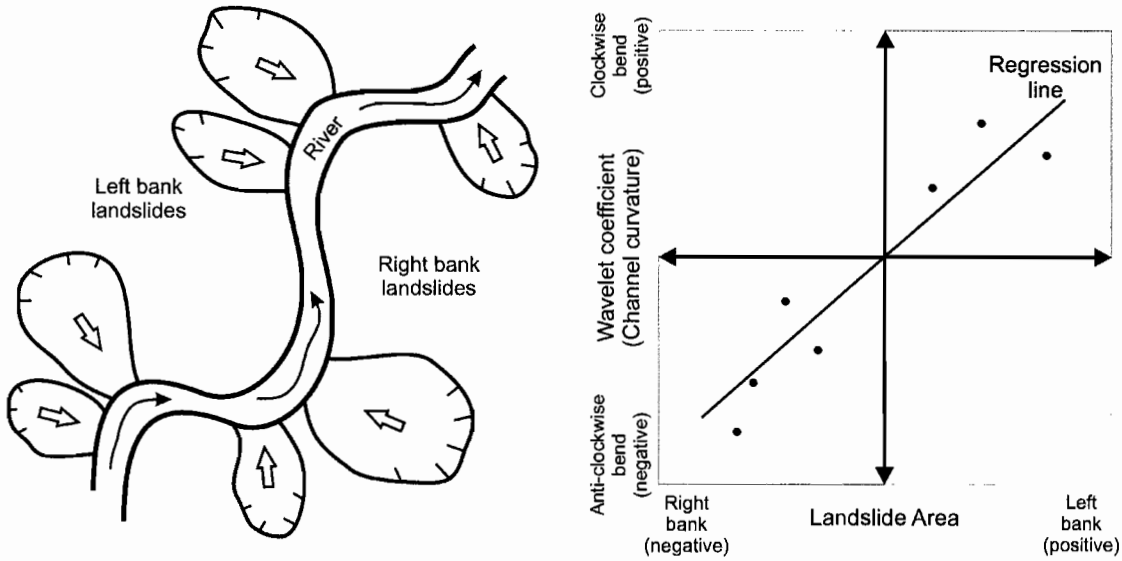

Figure 6. Quantifying channel curvature and bank-dependent landslide area. The cartoon on the left shows an idealized section of river with landslides clustering at the apex of meander bends. The graph represents how this would look when curvature is plotted against landslide area at a specific wavelet lengthscale. We use the correlation coefficient to quantify the correlation between landslides and varying scales of planform curvature.

As colored red in Figure 2, we observed that slides which adjoin the modern channel occur preferentially from 0 to 12 km, and along the incised channel section from 27 to 52 km. From 12 to 27 km, only one of the landslides has interaction with the modern channel (at 20.1 km). Towards the far end of the canyon (50–53 km) are several large slumps, the largest at 51 km with an area of 0.817 km^2. Qualitatively, the landslides between 28 and 36 km appear the most recently active, based on freshest (or roughest) surface features (Figure 7).

Figure 7. South Fork Eel River channel from 28 to 38 km. The channel is color coded by the absolute coefficients of the 1.5 km wavelet, with the warmer colors denoting larger coefficients. The inset shows the relevant part of Figure 2c, and highlights the effectiveness with which wavelet coefficients can replicate the channel planform, and the high correlation between landslides and the outer edge of meander bends. Note how the 1.5 km scale of sinuosity is superimposed on the larger scale (~6 km) valley sinuosity.

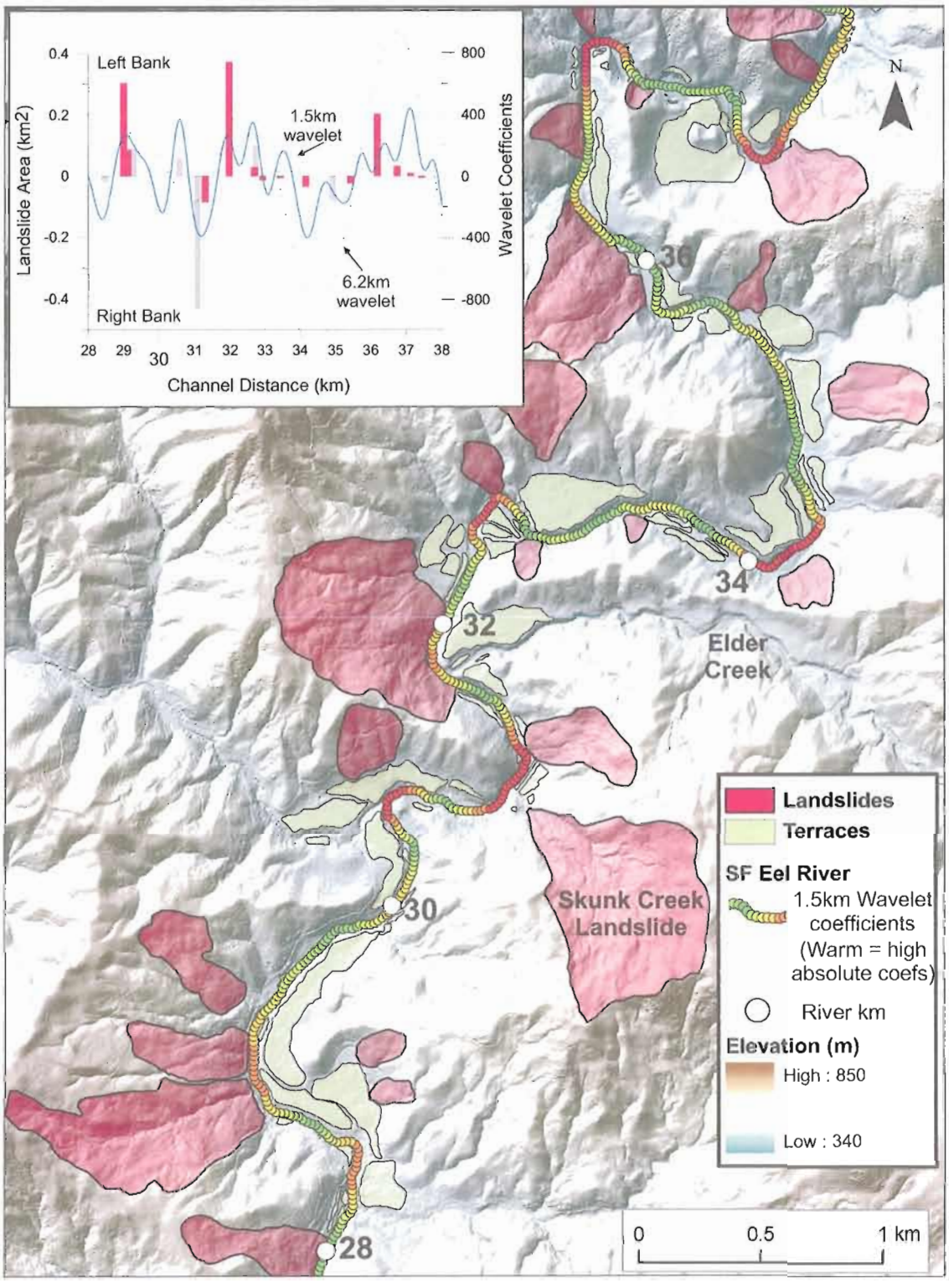
Left Bank
Right Bank
1.5km wavelet
6.2km wavelet
Landslide Area (km2)
Wavelet Coefficients
Channel Distance (km)
0.4
0.2
0
-0.2
-0.4
800
400
0
-400
-800
28 29 30 31 32 33 34 35 36 37 38
N
36
34
32
30
28
Elder Creek
Skunk Creek Landslide
Landslides
Terraces
SF Eel River
1.5km Wavelet coefficients (Warm = high absolute coefs)
River km
Elevation (m)
High : 850
Low : 340
0
0.5
1 km

4.2. Distribution of Terraces

Terraces persist along much of the SF Eel River (Figure 2a,b), and are most areally extensive along 10–26 km, where they occur on both sides of the river. Downstream of 26 km, terrace remnants are smaller and less continuous than upstream, and characteristically alternate from bank to bank. Some comparatively high but isolated terrace features are preserved sporadically along the length of the river (e.g., the terrace 60 m above the channel at 25 km), but these likely persist in the landscape from periods of channel migration that long pre-date the late Pleistocene–Holocene focus of this study. Figure 2(a) implies some incision into the gently sloping broad terraces between 11 km and 23 km, although much of this is a methodological artifact and primarily attributable to the median elevation of broad, gently sloping terraces, as opposed to channel incision.

Between 26 km and 39 km the channel becomes more sinuous, the depth of incision into the upper strath terrace gradually increases, and landsliding is more prevalent. At 39.3 km, the SF Eel River's drainage area approximately doubles at the confluence of Ten Mile Creek, and the SF Eel gradient increases sharply, as does the elevation difference between the channel and the reference strath terrace (Figure 2a,b). Downstream of 39 km the SF Eel River is confined to a steep, sinuous canyon (Figures 1b, 2d), and only isolated remnants of the terrace surfaces remain.

4.3. Channel Sinuosity and Landslide Location

Figure 8 shows the results of cross-correlation between wavelet coefficients and landslide location over a range of wavelet length-scales. We analyzed the whole channel, and the upper and lower sections of the channel separately, to see if the pattern of sinuosity and landsliding differed in the section which has been incised (downstream of 26 km). The upstream and downstream reaches exhibit different patterns of cross-correlation with changing meander wavelength. Along the 0–26 km section of the profile the channel is generally straight, with small-scale intra-floodplain sinuosity. Small wavelengths (pseudo-period 0.5 km) have the highest correlation with landslide location. Downstream of 26 km, the channel is more sinuous, and the cross-correlation exhibited a peak at a wavelength of 1.5 km. The spatial pattern along the whole channel length

mimics the 26–53 km pattern due to the larger number of slides in the regression. Figure 2c illustrates the optimal agreement between the 1.5 km period wavelet and the bank-dependent landslide location along the lower section of the river. The channel in Figure 7 is color coded by absolute wavelet coefficients of the 1.5 km wavelength wavelet (warm colors = high coefficient), and the warm colors at the apex of river bends frequently correspond with landslide locations.

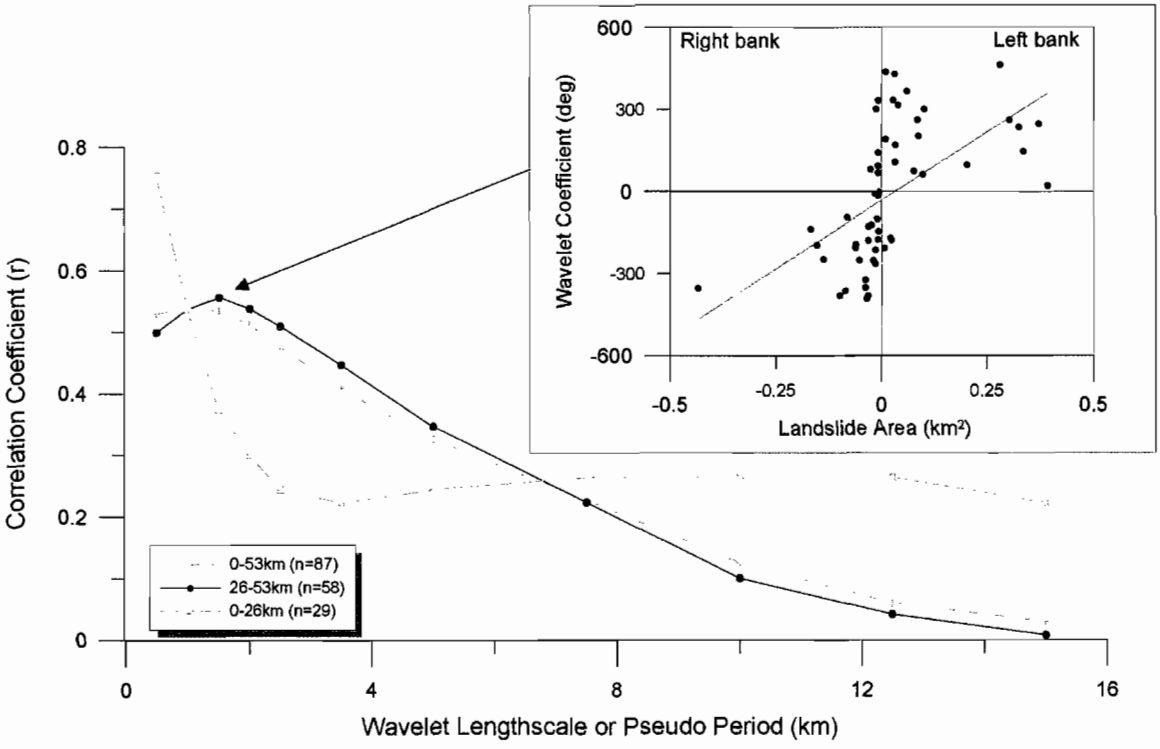

Figure 8. Cross-correlation between landslide area and wavelet coefficient over a range of wavelet lengthscales. The regression of the 1.5 km wavelet over channel distance 26–53 km is shown in the inset.

The largest absolute wavelet coefficients are associated with wavelet pseudo-period 6.2 km, centered on channel distance 36.8 km. This is where the river planform

best approximates the Gaussian derivative, and corresponds to a section of the river with entrenched large-scale sinuosity, as seen of Figures 1 and 7. The inset in Figure 7 shows the finer scale channel sinuosity captured by the 1.5 km wavelength, which is super-imposed on the larger 6.2 km wavelength.

5. Discussion

5.1. Incision-Landslide Correlation

The pattern of deep-seated landsliding along the SF Eel River, as documented from LiDAR, supports the notion that base level fall via channel incision has increased the incidence of landsliding. This is illustrated by sections of channel with late Pleistocene channel incision having a greater occurrence of along-channel landsliding. Upstream portions of our study area that have not been subject to recent channel incision (0–26 km) do not exhibit widespread or systematic landsliding when compared to the incised section of the SF Eel River (26–53 km), which has twice as many landslide features per unit of channel length. We note a strong tendency for landslides to cluster on the outer edge of river bends where the river incises laterally. The high incidence of landslides on the outer edge of channel bends may result from lateral incision at the base of the slope. Other considerations include the greater area of available hillslope in these locales upon which landsliding can occur, and hydrological considerations such as the concentration of groundwater flows and increased pore pressures in areas of topographic convergence.

5.2. Terrace Distribution

The apparent linearity of the upper terrace treads from 26 to 52 km suggests the treads are remnants of a once extensive and possibly continuous terrace surface. We use this as a reference surface to quantify channel incision along the river. The systematic decrease in the amount of river incision into this surface from 52 to 26 km suggests that a pulse of incision has migrated headward, although the cause of this incision (tectonic, eustatic or climatic in origin) remains unknown. Within the zone of incision there are

lower flights of terraces which also converge upstream, indicating that the SF Eel River has experienced several pulses of incision and strath cutting subsequent to the planation of the upper strath. In addition to the change in gradient at the Ten Mile Ck confluence, we note the more subtle inflection in the river profile at 24 km, where incision into the upper strath terrace pinches out.

The paucity of landsliding from 12 to 28 km corresponds with extensive terraces. Along this reach of the channel the terraces have effectively isolated most of the hillslopes from any recent or future channel incision.

5.3. Scale of Sinuosity

We found wavelet analysis to be an effective new method by which to characterize different scales of sinuosity along the channel profile. Our technique could be replicated on any channel for which high-resolution topographic data is available.

The Gaussian wavelet with pseudo-period (wavelength) of 1.5 km had the most meaningful correlation with the along channel distribution of mapped landslides (Figure 2c). River meanders with a scale of ~1.5 km (longitudinal channel length of an 'S-bend') may reflect a critical length scale for generating landsliding in the actively incising section of the SF Eel River. This length scale likely reflects a compromise between minimizing the radius of channel curvature that can persist for geomorphic timescales, whilst maximizing the width of hillslope base that is exposed to lateral incision on the outer edge of a meander bend, thereby having the greatest probability of undercutting and destabilizing a significant section of terrain. A meander with a small wavelength can have a very small radius, and exert a lot of hydraulic energy at the outer bank, but only over a short continuous length of the slope base. Very small radius meanders are also more likely to be modified by natural river evolution, and are unlikely to persist in the landscape. Conversely, a large wavelength meander may abut a significant length of slope, but as the bend has a larger radius, the migration rate and hydraulic energy directed at the slope will be comparatively less than a bend with smaller radius. Currently, we have little ability in predicting where deep seated landslides will occur in a landscape

beyond basic considerations of slope, drainage area and rock properties [*Densmore et al.*, 1998; *Korup et al.*, 2007; *Niemi et al.*, 2005]. Identifying critical length scales of meandering in a particular landscape may become an important and readily quantified metric in landscape evolution models.

The most sinuous section of river (33–42 km) has a characteristic wavelength of 6.2 km. Although this scale of sinuosity did not correlate as well with landsliding as did smaller wavelengths, we note along 31–38 km (Figure 7) there is good agreement between the 6.2 km coefficients and landslide location. The ~6 km wavelength of sinuosity in this stretch represents the entrenched river course, especially from 30 to 45 km, and would not have changed significantly since the late Pleistocene, as the strath terraces follow a similar pattern. In contrast, smaller-scale sinuosity (1.5 km) is superimposed on the ~6 km scale of valley meandering, and at this smaller scale the channel can incise into the strath terraces, undercutting adjacent hillslopes within the architecture of the larger scale valley sinuosity. This scale of lateral channel activity appears to impart a dominant control on the location of mappable landslides.

Very short wavelengths of sinuosity best correlated with landsliding from 0 to 26 km (Figure 8), although we do not view this result as significant. The correlation was strongest at the 0.5 km length-scale, but this is approaching the scale of intra-channel noise, and the high correlation is likely a reflection of increased degrees of freedom with the smaller meander scale as opposed to a physical control on landslide location. There were only 29 landslides along the 0–26 km river section, and the correlation is not as robust in comparison to the lower half of the profile which has a greater population of landslides. As such, we downplay the role of modern lateral channel migration as a significant control on landslides along the 0–26 km section of the river. Additionally, there is little evidence of recent vertical incision along 0–26 km, significant terraces and flood plains isolate much of the hillslopes from the river from 10 to 24 km, and only rarely could the river be considered to influence the adjacent slopes (e.g., 20.1 km). The high concentration of landsliding from 0 to 10 km corresponds with the very weak argillaceous Central Belt mélange, which has a very different character to the Coastal

Belt and Yager lithology encountered by the SF Eel downstream of 10 km (Figure 2). For much of the 0–10 km section, the river is confined in a narrow valley, in constant connection with the weak adjacent hillslopes. This tight connection between the SF Eel River and adjacent landslides likely illustrates how weak rocks are unable to resist failure, as opposed to a signal of active channel incision. As such, weak lithology can potentially overwhelm other landscape signals.

5.4. Long Term Landslide–Channel Coupling

Most studies of hillslope-channel coupling to date have looked at smaller scale catchments, with active, quantifiable movement, where the interactions between the channel and slope failures are readily discerned (See for example *Harvey* [2001] and references therein). Our study is complicated by an extensive study area, large, mostly dormant slope failures (lacking in chronology), a time frame tentatively spanning the Late Pleistocene – Present, and poor constraints on the rate or homogeneity of incision. Despite these challenges, the linkages we find between channel incision and deep-seated landsliding are instructive when considering channel-landslide coupling over longer time periods.

Landslides along the lower reach of our study area in the SF Eel River preferentially occur in areas subject to vertical and/or lateral channel incision, so base level fall appears a primary factor in the landslides' ultimate failure, as we would predict from fundamental geomechanics [*Terzaghi*, 1950]. In Figure 2a we distinguished the slides that extend onto the floodplain of the modern channel. We consider these slides to be influenced by recent incision of the SF Eel River, as the landslide mass extends below the projected terrace elevation. Of the 26 slides not considered coupled in Figure 2a, 22 appear to have evidence of previous interaction with the SF Eel River. For example, most slides occur at the edge of strath terraces (see for example the two small slides at ~28.5 km, Figure 7), and there are very few landslides which are restricted to higher parts of the hillslope, away from the direct influence of the SF Eel River during its strath cutting period. The comparative scarcity of landslides higher up on the slope would suggest that base level exerts a greater control on deep-seated landslide location than seismic

acceleration in this landscape [*Densmore and Hovius*, 2000]. The hillslopes adjacent to the SF Eel terraces would have been undercut by the river at the time of strath planation as the river eroded laterally, but have since become isolated as the river has incised, the terrace effectively acting as a buffer between channel incision and hillslope. Without age control on these landslides or the time of terrace formation it is speculative to say the two events were coeval, but the presence of many qualitatively old slide features at the margins of strath terraces may reflect tight coupling between the SF Eel and hillslopes during strath cutting. The controls on the cyclical process of strath terrace planation and subsequent channel incision are yet to be fully resolved, but once a river starts cutting a strath and undermining hillslopes, the supply of sediment from activated landslides may represent a positive feedback, with coupled landslides at the strath margin providing tools and abundant sediment to inhibit vertical incision and promote further strath cutting [*Finnegan et al.*, 2007; *Fuller et al.*, 2009].

There are many large dormant landslides with toes encroaching onto the modern SF Eel channel, such as those seen in Figure 7. If these landslides were active, we would expect to observe perturbations in the channel profile or bed-form attributable to landslide toe deposits [*Korup*, 2005a]. The lack of deep seated landslide activity under modern environmental conditions is a defining feature of this study area. We observe a network of gullies and small creeks eroding into the dormant mass of these landslides, and this secondary reworking of the landslide deposit may be the primary means of removing sediment from the system, rather than direct sediment delivery from the landslide to river.

5.5. Channel Incision, Landsliding and Long Term Hillslope Evolution

Poor constraints on incision/landslide chronology inhibit predictions as to whether there is a critical amount of incision required to generate slope failure, or whether there is a characteristic lag period between incision and slope failure. The most recent incision (e.g., 15–20 m at 28–30 km) corresponds with the terrace dated to 20.5 kyr [*Fuller et al.*, 2009], and what qualitatively appear to be some of the most recent landslides along the profile. This observation suggests that ~15–20 m of channel incision adjacent to a

hillslope may be sufficient to generate large-scale slope failure in this landscape, although it is difficult to attribute causality given the changing climate and vegetation over the Holocene. Farther downstream, the amount of incision into the upper strath increases, and the character of the landslide deposits change. In the channel reach below the Ten Mile Creek confluence (41–50 km), most of the landslide deposits have been eroded. Slopes along this section of the river are steep and planar (Figure 2d), and deep-seated slumps are rare. Near the end of the profile, the slumping failure style returns as seen in the large slides at 51 and 52 km.

The strath terraces which converge upstream indicate that incision is migrating headward. Therefore, the farther down the profile, the longer a section of the river has been undergoing channel incision into the upper strath. This observation allows a simplistic space-for-time substitution [e.g., *Hilley and Arrowsmith*, 2008], and we can speculate about the long term cyclical hillslope response to channel incision. We propose that initial channel incision generates large slope slumps where the river abuts the hillslope (28–38 km). Once the landslide has slumped and stabilized, the landslide deposit is gradually removed by subsidiary erosion processes. As channel incision proceeds and the channel migrates within the valley, the strath is incrementally removed, all original landslide debris is eroded, and the hillslopes are progressively steepened by shallower planar landsliding (41–48 km). During this time, we speculate that weathering proceeds into the recently exposed bedrock as channel incision increases. Eventually, stresses in the bedrock have accumulated and/or weathering has decreased mountain scale rock strength sufficiently [*Schmidt and Montgomery*, 1995], to generate a second generation of large slump failures, such as we see at 50–52 km. Qualitative hillslope evolution models have been proposed in the past [e.g., *Cendrero and Dramis*, 1996; *Hugenholtz and Lacelle*, 2004; *Palmquist and Bible*, 1980], but generally conclude at slope failure, and don't explore slope evolution under sustained incision.

6. Conclusion

Predicting the size, location and timing of deep-seated landslides remains a challenging problem, and much research needs to be done before we can articulate a comprehensive geomorphic transport law for deep-seated landslides. We constrained our analysis to the spatial pattern of deep-seated landslides in response to channel incision, as opposed to determining rates of landslide generated sediment flux – the quantity a sediment transport law would seek to address. Our key findings, that deep-seated landsliding correlates well with channel incision and the outer edge of meander bends are not unexpected, but these relations have seldom been systematically quantified in a manner that could eventually be incorporated into an expression for geomorphic transport by deep seated landslides. Channel meanders with a wavelength of 1.5 km best explained the distribution of along-channel landsliding in this catchment, and we suspect this optimal wavelength will vary between different landscapes, drainage areas, lithology, and river systems.

We propose a long term model of hillslope evolution in a slump-prone landscape undergoing continual base level fall. Initial incision induces deep-seated slumping. The landslide mass stabilizes, and is removed by smaller scale erosion processes, exposing the failure surface. Weathering penetrates into the hillslope, and after continual channel incision we predict an additional episode of deep seated slumping.

CHAPTER III

LONG-TERM KINEMATICS AND SEDIMENT FLUX OF AN ACTIVE EARTHFLOW, EEL RIVER, CALIFORNIA

This paper was published in the journal *Geology* in September 2009, volume 37(9), pages 803–806. This paper was co-authored with Josh Roering and Jim McKean. Josh provided funding, advisorial, and editorial support. Jim provided editorial and field support.

1. INTRODUCTION

Large, slow moving (<2 m/yr) glacier-like earthflows are pervasive in many rapidly eroding landscapes world wide, most commonly in fine grained marine sediments. They are extremely problematic for land management, transport corridors, and represent major point sources of sediment to the channel network, yet we have little knowledge of earthflow behavior beyond the decadal scale. While factors such as precipitation, temperature, topographic loading or toe erosion are widely recognized to influence motion (Keefer and Johnson, 1983), the geomorphic role of this style of slow, persistent mass wasting as an erosional process remains poorly constrained, especially when compared to other processes such as bedrock channel incision, debris flows or soil creep (Dietrich and Perron, 2006). The majority of earthflow research has been directed at interpreting earthflow mechanics by constraining movement patterns over seasonal-to-annual monitoring periods, and this approach yields excellent data on contemporary earthflow behavior (e.g., Coe et al., 2003; Iverson and Major, 1987; Zhang et al., 1991).

With notable exceptions (Bovis and Jones, 1992; Kelsey, 1978), comparatively little focus has been applied to the longer term evolution of individual earthflows. Active earthflows can deflate their source basins orders of magnitude faster than regional erosion rates (Kelsey, 1978), and consequently, earthflow movement at a given location will likely be episodic. As such, active earthflows may compose a small percentage of the landscape, yet account for a large fraction of the regional sediment flux. Attesting to the ephemeral nature of earthflow activity, much of an earthflow-prone landscape is imprinted with ubiquitous subtle headscarps, toes, and deflated transport zones from multiple generations of earthflows and landslides in various stages of dormancy (e.g., Bovis and Jones, 1992). Factors controlling long-term earthflow evolution include availability of easily mobilized source material, base level control and slope buttressing, climatic variability, and land-use practices. To better understand the relative importance of such factors on earthflow transport history and evolution, we aim to constrain the long term sediment flux, kinematics, and topographic development of an individual earthflow.

2. EEL RIVER, NORTHERN CALIFORNIA

The coastal ranges of northern California are composed of penetratively sheared meta-sedimentary interbedded sandstone and argillite of the Franciscan Mélange, a Jurassic-Cretaceous accretionary prism complex, renowned for earthflows and deep seated landsliding (Iverson and Major, 1987; Kelsey, 1978). Some of the most extensive earthflow activity in northern California occurs along the main stem of the Eel River and its tributaries between Dos Rios and Alderpoint (Brown and Ritter, 1971). Highly erodible Central Belt Mélange and high seasonal rainfall predispose this section of the Eel River to ubiquitous earthflows. Here, we observe slow-moving landslides spanning all states of activity and form, from small <100 m^2 slumps, to huge earthflow complexes spanning 900 m of relief and extending up to 5 km from channel to ridge.

We focused on a 1.5 km-long active earthflow (0.2 km^2 area) entering Kekawaka Creek, an 85 km^2 tributary of the Eel River (Fig. 1). This active earthflow has classic morphology (Keefer and Johnson, 1983), including: a steep, amphitheater-like source

area; a narrow, elongate transport zone which over-rides several bedrock steps; and termination at the creek as a bulbous toe (Fig. 1- Appendix B). Specifically, we study the upper half of the earthflow where the surface has minimal disturbance and little lateral input from creeks and other earthflows. Based on morphology, we sub-divide it into three kinematic units; a steep headscarp or source area, a long narrow transport zone, and a mid-slide compressional zone with reduced topographic gradient (Fig. 1). The headscarp of the earthflow currently abuts a broad ridgeline, underlain by sandstone.

3. HISTORICAL AIR PHOTOS AND SURVEYING

We use several approaches to study movement of the Kekawaka earthflow. Underpinning the analysis is high resolution (1m grid spacing) digital topography derived from airborne laser scanning (LiDAR) that reveals earthflow morphology in unprecedented detail (Fig. 1, Fig 1 - Appendix B). To determine modern earthflow movement, we placed 27 0.9 m rebar stakes on the slide, and recorded their position using a total station for 3 successive summers (2006–2008).

To quantify decadal scale slide deformation, we rectified historical air photos to remove lens distortions and topographic effects (Wolf and Dewitt, 2000) and measured offset features in sequential photographs (Baum et al., 1998, Walstra et al., 2007). We obtained aerial photos taken in 1944, 1964, 1968, 1981, and 1991, in addition to the LiDAR coverage flown in 2006, defining 5 time intervals of landslide change (Table 1, Appendix B). We identified 53 individual trees growing on the earthflow surface and tracked their positions (and thus velocities) from 1944 to 2006 (Figs. 1–2). The sequential location of trees on stable ground adjacent to the earthflow enabled us to constrain errors due to imperfect rectification or vegetation change (Fig. 2, Appendix B).

Figure 1. Kekawaka Earthflow displacement. Colored lines show trajectories of trees growing on the earthflow from 1944 to 2006, which we demarcate into 3 kinematic units. The inset shows depth profiles of meteoric ^{10}Be concentration. Vertical error bars show the sample interval, and horizontal bars the analytical error. The background image is LiDAR derived slope (1 m resolution). Inset map shows site location in northern California.

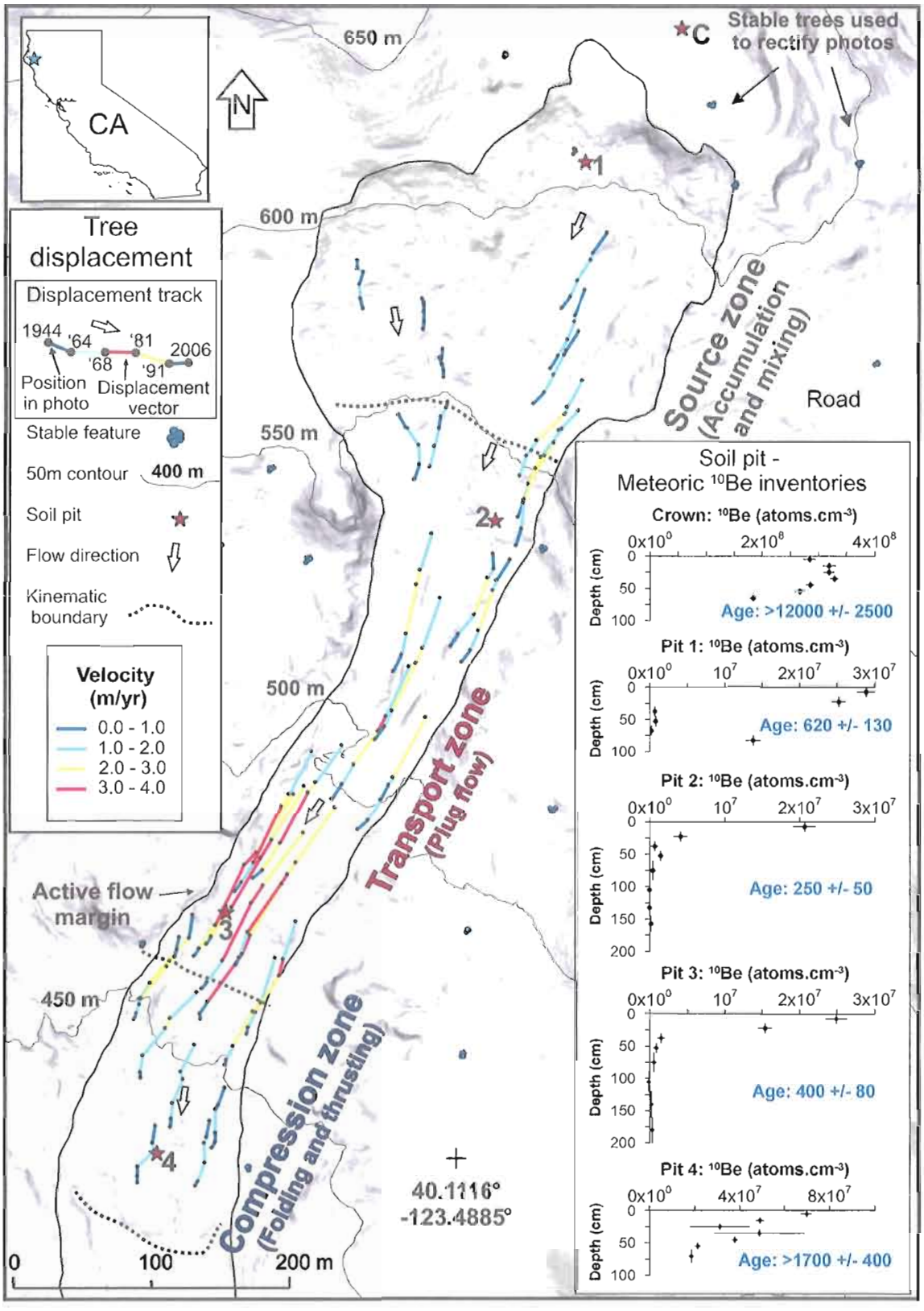
CA
N
650 m
600 m
550 m
500 m
450 m
Stable trees used to rectify photos
C
1
2
3
4
Source zone (Accumulation and mixing)
Road
Transport zone (Plug flow)
Compression zone (Folding and thrusting)
Active flow margin
Tree displacement
Displacement track
1944
'64
'68
'81
'91
2006
Position in photo
Displacement vector
Stable feature
50m contour
400 m
Soil pit
Flow direction
Kinematic boundary
Velocity (m/yr)
0.0 - 1.0
1.0 - 2.0
2.0 - 3.0
3.0 - 4.0
Soil pit - Meteoric 10Be inventories
Crown: 10Be (atoms.cm-3)
Age: >12000 +/- 2500
Pit 1: 10Be (atoms.cm-3)
Age: 620 +/- 130
Pit 2: 10Be (atoms.cm-3)
Age: 250 +/- 50
Pit 3: 10Be (atoms.cm-3)
Age: 400 +/- 80
Pit 4: 10Be (atoms.cm-3)
Age: >1700 +/- 400
Depth (cm)
40.1116°
-123.4885°
0
100
200 m

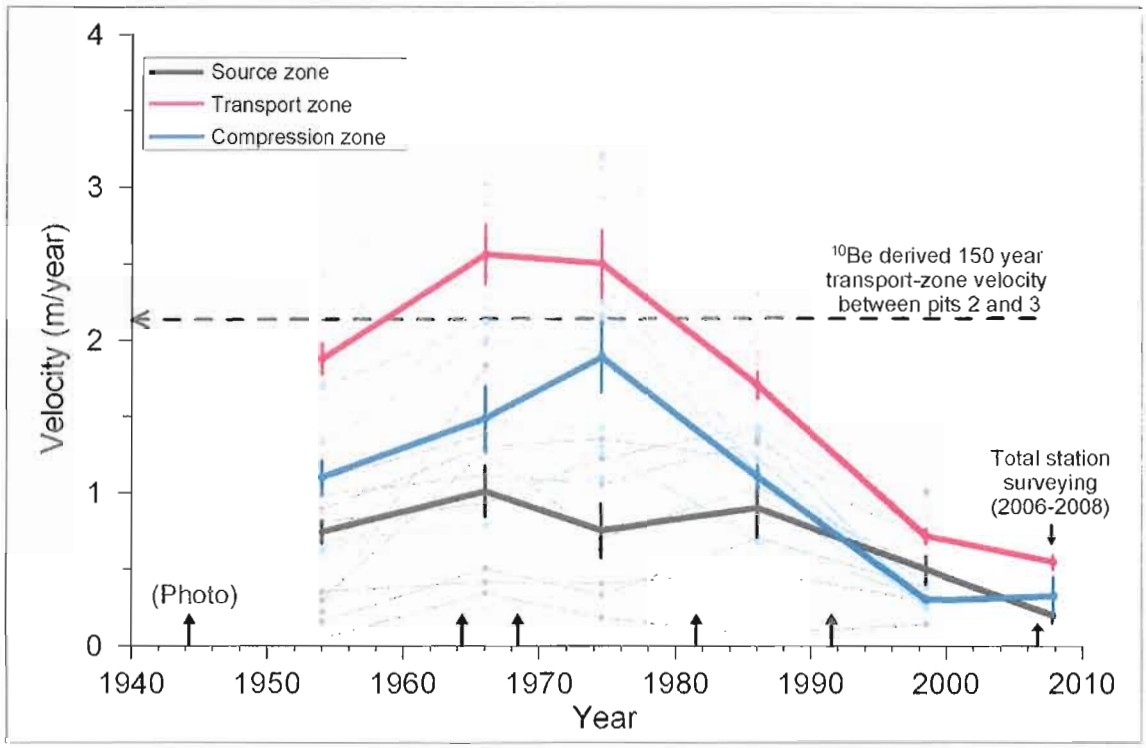

Figure 2. Tree velocities for the three kinematic zones of the earthflow for each photo interval, in addition to the 2006–2008 total station survey data. We plot the individual velocity of each tree (faint lines), and the mean and standard error for each kinematic unit (bold lines).

4. METEORIC ^{10}BE AND THE TRANSPORT ZONE "SOIL CONVEYOR"

Based on field and LiDAR observations, we envisage the earthflow transport zone as a relatively undeformed soil conveyor that progressively translates material generated and mixed in the source area to the compressional zone. Because it can take 100s to 1,000s of years for soil to move through an earthflow, this novel application of meteoric ^{10}Be has the potential to substantially extend historical records of earthflow movement.

Meteoric ^{10}Be is produced in the atmosphere by the spallation (fragmentation) of atmospheric gas nuclei from cosmic rays (Monaghan and Elmore, 1994). Once produced, ^{10}Be (half life of 1.51×10^6 years) attaches to sub-micron aerosol particles in the atmosphere. These particles are scavenged by precipitation, and delivered to the Earth's

surface. The ^{10}Be nuclide is rapidly adsorbed and sequestered when it contacts fine grained soils, which typically have a high surface area per volume, and high cation exchange capacity (McKean et al., 1993; Pavich et al., 1986; You et al., 1989). ^{10}Be can be lost through groundwater leaching or clay translocation to lower soil horizons (Pavich et al., 1986) and is readily mobilized under acidic soil conditions. Soils derived from the Central belt Franciscan mélange are ideal reservoirs for ^{10}Be because they are clay rich and relatively non-acidic.

By measuring the inventory of ^{10}Be through soil profiles and dividing by the annual ^{10}Be delivery rate, we calculated the age of several earthflow surfaces. Below the base of the steep source zone, which experiences pervasive block rotation, ravel, and soil slips, the reconstituted earthflow material exhibits a broad, planar morphology, demarcating the top of the transport zone "soil conveyor." At this location, we expect concentrations of ^{10}Be to be low given the extent of source zone reworking and thus dilution of previously stable ^{10}Be enriched soil incorporated into the earthflow. Through the transport zone, we assume that the surface remains relatively intact such that local inventories of ^{10}Be progressively increase downslope. The ratio of the distance between two sample locations and the difference in their surface ages provides an estimate the long-term velocity of the transport zone.

For this approach, we assume the following: 1) rainfall and ^{10}Be production are relatively constant with time, 2) minimal ^{10}Be is lost once it adheres to the soil (e.g., via leaching), 3) the cation adsorption capacity of the soil is not exhausted, and 4) slide movement occurs by simple plane strain. Below the headscarp, incomplete mixing of previously stable surface soils with high ^{10}Be concentrations may cause pockets of concentrated ^{10}Be to persist. Such pockets should be readily identifiable because the progressive accumulation of ^{10}Be in stable, clay-rich surfaces tends to generate well-behaved exponential concentration profiles.

We dug 4 soil pits along the axis of the earthflow, and 1 on unfailed terrain above the headscarp crown (Pit C, Fig. 1). The earthflow material is colluvium (poorly sorted gravelly clayey sand with occasional large rocks 1–5 m in diameter), whereas the soil

above the headscarp was a loamy sand. We sampled soil at regular depth intervals in each pit, and collected intact samples to determine representative bulk density of the earthflow colluvium (2.1 ± 0.1 g/cm^3). We extracted ^{10}Be from the soil samples following the soil fusion technique described in Stone (1998) at the University of Washington Cosmogenic Isotope Laboratory. The ^{10}Be/^{9}Be ratio was analyzed via mass spectrometry at PRIME Lab, Purdue University. By integrating through the concentration profile, we calculated the inventory of ^{10}Be for each sample site (atoms/cm^2). We used the average annual rainfall recorded at Alderpoint (15 km NW) of 1.3 m ± 0.06 (mean ± s.e., 1940–1980) and an estimate for mid-latitude meteoric ^{10}Be production of 1.3×10^6 ± 20% atoms/cm^2/yr per meter of rain (Pavich et al., 1985; Pavich and Chadwick, 1997) to quantify the surface exposure age of the earthflow soil.

5. RESULTS

Our surveying and photographic data show that earthflow velocities vary significantly between the 3 kinematic units (Figs. 1–2). Maximum slide velocities averaged across each kinematic zone are lowest in the upper source zone (<1 m/yr), fastest through the narrow transport zone (2.5 m/yr), and moderate through the mid-slide compressional zone (1.8 m/yr). Since 1944, the average velocity in the transport zone is 1.7 m/yr, although temporal variation was substantial. Velocities were highest in the late 1960's and 1970's and have steadily decreased to <1 m/yr since. This temporal pattern is broadly consistent over all three kinematic units (Fig. 2). The headscarp exhibited negligible expansion over the photographic record, whereas the mid-slope toe advanced over 40 m.

Our ^{10}Be analysis (Fig.1, Table 2 – Appendix B) demonstrates that the unfailed soil above the headscarp (Pit C) has the highest inventory of ^{10}Be and a minimum surface age of 12ka. On the earthflow, Pits 1–3 show the majority of ^{10}Be is retained in the upper 40 cm of soil, although Pit 1 in the source zone has an anomalous high concentration at 90 cm. Pits 2 and 3 in the transport zone show a difference in surface age of 150 ± 90 yr, which can be used to derive a long-term slide velocity of 2.1 ± 1.3 m/yr (Figs. 1–2). Pit 4,

in the compression zone, retained 1700 ± 450 yr of 10Be, although this age remains a minimum estimate, as our deepest sample interval shows high concentrations of ^{10}Be implying the isotope has penetrated to depths below 90 cm.

6. DISCUSSION AND CONCLUSIONS

The spatial pattern of movement, as revealed by photo-derived tree displacement vectors (Fig. 1), shows a systematic change in displacement rates from the headscarp to the lower portion of the earthflow. The upper source zone exhibits slowing velocities on the order of 1 m/yr, indicative of slow steady input of source material from headscarp slumping. The maximum earthflow velocities are obtained through the narrow (80 m wide) section of the transport zone. This section also has the smoothest surface, largely free of folding or extensional slumping, implying plug sliding with minimal internal deformation (Fig. 1- Appendix B). The mid-slope compressional zone exhibits slower movement than the transport zone, but follows a similar temporal pattern. Here the slide widens and has a series of folds and thrusts that reflects deformation from the advancing transport zone.

Although we do not have well-constrained data on the basal sliding depth, field-based estimates from the channel margin of the Kekawaka slide are ~6 m, and similar sized earthflows have depths in the range of 4–8 m (Iverson and Major, 1987; Zhang et al., 1991). Taking an average velocity of 2 m/yr, the earthflow translates over 1000 m^3/yr through the transport zone. Given that the combined area of the earthflow source and transport zones is 1.0×10^5 m^2, sliding at 2 m/yr equates to an average lowering rate of 10 mm/yr, ~20 times faster than the estimated regional erosion rate (Fuller et al., 2009). The evacuated volume of the earthflow source area and transport zone is ~1.0×10^6 m^3, suggesting that ~1000 yr are required to evacuate the earthflow basin given average transport zone sliding of 2 m/yr.

The inventories of ^{10}Be provide crucial insight about the long term evolution of the landslide. Pit C on the unfailed surface above the headscarp has the highest ^{10}Be

inventory as would be expected for stable ground. Given the sandy nature of the soil at this location, some of the ^{10}Be may have been lost from this pit, probably by leaching. Pit 1 is within the steep, unstable part of the accumulation zone amidst back-rotated headscarp slumps and disintegrating blocks of detached argillaceous bedrock. As such, we interpret much of the Pit 1 inventory and concentration spike at 80–90 cm to be residual headscarp soil that has yet to be fully mixed or buried, indicating that Pit 1 reflects a transient state between headscarp failure to reconstituted earthflow surface.

Owing to their location in the transport zone, Pits 2 and 3 are useful for determining long-term rates of earthflow movement. Both show the majority of ^{10}Be is retained within the upper 40 cm, and these pits have negligible ^{10}Be below this depth. We argue that ^{10}Be at these sites began accumulating when the surface moved into the transport zone, which is dominated by translational movement as opposed to the mixing in the source zone. Our ^{10}Be-derived, pre-historic velocity (2.1 m/yr) exceeds the 62 year average transport zone velocity obtained from the photos (1.7 m/yr) and to account for the reduced velocities over the past 30 yr, the transport zone may have sustained velocities approaching 2.5 m/yr prior to 1944.

Pit 4 has 1700 ± 400 yr of ^{10}Be. The Pit 4 ^{10}Be depth profile shows ^{10}Be concentration decreasing in a noisy exponential fashion, and the isotope has penetrated to depths well below 40 cm, and probably below our deepest sample at 90 cm. The Pit 4 age represents a minimum age of the earthflow. The transport rate between Pits 3 and 4 is ~0.15 m/yr, and the earthflow has longitudinally shortened through this section via compression and widening, which may account for much of the deceleration. Air photo-derived velocities in this area exceed 1 m/yr, suggesting that earthflow movement is episodic and the earthflow surface proximate to Pit 4 may have originally been formed during a previous episode of activity, and has subsequently been reactivated, all the while continuing to accumulate ^{10}Be.

The acceleration and subsequent gradual slowing of the 1944-2006 vectors illustrates the non-steady nature of this earthflow's movement at the decadal scale, probably due to climatic variation, supporting the notion of episodic or surging behavior

superimposed on the long-term earthflow evolution. Historical increases in earthflow activity have colloquially been attributed to anthropogenic activity such as grazing, but the dramatic slowing of the Kekawaka earthflow does not support this contention. The peak velocities recorded from 1964 through 1981 coincide with both an increase in rainfall and discharge across the Eel River catchment in the mid 20th Century (Syvitski and Morehead, 1999), and a large storm event in 1964.

Regardless of climatic forcing, a supply of readily mobilized source material is requisite for continued earthflow movement. The Kekawaka earthflow headscarp has retrogressed to a sandstone ridgeline, likely limiting or greatly slowing future expansion and the source zone has received minimal fresh material since the 1940s. With continued earthflow movement (and assuming no downward propagation of the failure surface), the slide thickness must have decreased causing a reduction in shear stress. This supply limitation may be a primary factor in the long-term velocity decline revealed by our analysis, although the buttressing effect of accumulation in the low gradient mid slope compressional zone may also contribute. The surface of the earthflow is 5-10m lower than the surrounding slopes, consistent with progressive deflation and slowing of the active slide. Given this supply limitation, the Kekawaka earthflow appears set to become a dormant feature, typical of this slide-dominated landscape.

CHAPTER IV

DECADAL-SCALE VARIATIONS IN EARTHFLOW MOVEMENT AND SEDIMENT PRODUCTION USING HISTORICAL AERIAL PHOTOS AND AIRBORNE LIDAR, EEL RIVER, CALIFORNIA

This chapter is in preparation for submission to the journal *Geological Society of America – Bulletin.* This chapter was co-authored with Josh Roering, who provided financial, advisorial and editorial support.

1. INTRODUCTION

In non-glaciated mountainous landscapes, sediment production and hillslope form are primarily controlled by mass wasting processes, including deep seated landsliding and earthflows. These large slope failures can establish or modify drainage patterns, alter hillslope morphology, and impart large perturbations on sediment budgets by regulating the timing, magnitude, frequency, spatial distribution, and grain size of sediment entering the channel or river network (Hovius et al., 1998; Korup, 2005b, 2006b). This has direct implications for flooding, channel network evolution, sediment transport, aquatic habitat, and infrastructure. While the importance of landsliding in mountainous landscapes has been long recognized, understanding how landsliding, and in particular earthflows, operate as a geomorphic process has proven more challenging.

1.1. Earthflows – Slow Moving 'Earth Glaciers'

Earthflows are a class of landslide (Cruden and Varnes, 1996) characterized by continuous movement along transient shear surfaces with a degree of internal deformation or flow. They span a range of landslide failure styles, and have been variably described as landslide complex (Iverson, 1986a), earth-slide (Cruden and Varnes, 1996), and mud-slide (Chandler and Brunsden, 1995; Glastonbury and Fell, 2008). Here, we use the term earthflow as advocated by Hungr et al. (2001) to describe large, slow moving landslides. These features typically resemble 'earth glaciers'. They are slow moving (<4 m/a), large (>500 m long), deep-seated (>5 m thick), clay rich, and behave in a plastic or visco-plastic manner (e.g., Baum et al., 1993; Bovis and Jones, 1992; Chandler and Brunsden, 1995; Coe et al., 2003; Iverson and Major, 1987; Kelsey, 1978; Malet et al., 2002; Zhang et al., 1991). Earthflows classically have an hour-glass planform, with an amphitheatre-like accumulation zone, an elongate narrow transport zone, and a lobate toe (Keefer and Johnson, 1983). Commonly earthflows exhibit seasonal movement patterns and can require several months of cumulative rainfall before the onset of movement. Earthflows can potentially dominate sediment delivery to channels in erosive landscapes (Kelsey, 1978; Swanson and Swanston, 1977), yet seldom fail catastrophically. We specifically distinguish earthflows from large displacement, catastrophic single event failures, such as rockslides, slumps, or translational bedrock slides.

1.2. Mass Movements and Landscape Evolution

A common approach to quantify the role of a surface process in landscape evolution is to develop a physically based mathematical statement which describes the sediment flux or erosion, and resulting landscape form, attributable to the process over geomorphically significant time and space scales (Dietrich et al., 2003). This statement can then be incorporated into numerical landscape evolution models to quantify the process's contribution to landscape evolution and change (e.g., Perron et al., 2008). While this approach has worked successfully for surface processes which operate

predictably across a landscape (such as channel incision, slope dependent soil creep, and debris flow incision), landslides have proven more challenging to describe using this framework. Difficulties arise when extrapolating geomechanical theories of slope stability beyond an individual hillslope to the landscape scale, where the hillslope material properties, vegetation, destabilization processes, rate of base level change, and triggering factors (meteorological and seismic events) are inherently spatially and temporally variable (Dietrich et al., 2003).

Despite these challenges, some progress has been made with single-event catastrophic deep-seated landsliding. Landsliding of this type is somewhat predictable, based on structure, bedding, defects, critical strength discontinuities (Korup et al., 2007; Pettinga, 1987), and considerations of mountain scale strength (Schmidt and Montgomery, 1995). Landscape evolution models incorporating a simplified process of deep seated bedrock failure can generate synthetic landscapes which statistically replicate real topography. These models incorporate probabilistic event failure based on a critical slope (Densmore et al., 1998) and employ detachment limited transport of resulting landslide debris.

1.2.1. Earthflows and Landscape Evolution

No landscape-scale theory exists for slow, sustained mass movements such as earthflows, and there is little data or theory pertaining to earthflow behavior beyond the decadal scale. As a consequence, we cannot confidently explain where earthflows occur in a landscape, what percentage of terrain is active at a given time, the duration of activity, and what governs long-term movement. A key question is whether earthflow movement is systematic or predictable in space and time.

Perhaps more important than the lack of theory describing catchment-scale earthflow generated sediment flux, we also lack a conceptual model describing the long term evolution of an earthflow prone landscape, and even the long-term evolution of an individual earthflow. For clay rich, earthflow-prone hillslopes, there is nothing

comparable to the colluvial hollow and debris flow framework applicable to soil mantled uplands (Dietrich and Dunne, 1978; Lehre and Carver, 1985).

1.2.2. The Focus on Earthflow Mechanics

Although we lack earthflow data for the long term, extensive work has been undertaken on the behavior of individual earthflows at the seasonal scale (Coe et al., 2003; Iverson and Major, 1987; Malet et al., 2002; Van de Grift and Sack, 2004), specific earthflow mechanics such as shear zone dilatency and strengthening (Iverson, 2005; Schulz et al., 2009), and the evolution of material strength over time (Maquaire et al., 2003). Many attempts have been made to model earthflow movement and rheology (e.g., Angeli et al., 1996; Baum et al., 1993; Bruckl and Sehidegger, 1973; Iverson, 1986c; Savage and Wasowski, 2006; van Asch et al., 2007; Vulliet and Hutter, 1988), primarily to describe or replicate the behavior of specific earthflows.

Despite the abundance of site specific geomechanical studies focusing on seasonal earthflow movement, knowledge of earthflow activity across a landscape trails our understanding of other styles of landsliding. This is in part attributable to the continuous, sometimes inconspicuous, failure style of earthflows. Whereas single event landslide failure can be easily bracketed between sequential sets of aerial photos or site visits, earthflows can continue moving for many decades, at rates heterogeneous both over time and spatially within an individual earthflow complex (Swanson and Swanston, 1977).

One of the few attempts to study longer term earthflow behavior was undertaken by Bovis and Jones (1992), who used radiocarbon dating and dendrochronology to link periods of accelerated earthflow movement with sustained wet periods across several hundred years of climatic changes in British Columbia. Bovis and Jones (1992) stressed the sensitivity of large slow moving earthflows to multi-year climatic trends, rather than individual storms or wet seasons.

1.3. Earthflows – A Unique Form of Landslide

1.3.1. Scaling Relationships

Inventory maps of catastrophic landslides reveal that landslide frequency often decays as the inverse power of landslide area, both for a total landslide inventory, or an event specific distribution (Guzzetti et al., 2002; Malamud et al., 2004). From this fractal relationship, long-term landslide erosion rates can be estimated (Hovius et al., 1997). In comparison, few, if any, earthflow inventory maps sufficiently document earthflow area, distribution, and populations to allow investigation of comparable scaling relationships and estimation of earthflow derived sediment flux.

1.3.2. Long Term Erosional Features

Dormant earthflow features can persist in the landscape for thousands of years (Mackey et al., 2009). Therefore, the history of earthflow evolution and movement must be integrated across a range of climatic conditions and topographic changes, rather than a single causative event such as an earthquake or storm (Bovis and Jones, 1992). Bedrock slopes, in contrast, can adjust suddenly to incision or climatic change (Burbank et al., 1996; Ouimet et al., 2009), making the effect of landscape change immediate and obvious. In both landscape evolution models and calculations of sediment flux, catastrophic slope failure is often amenable to simplification as a detachment limited erosion problem (Densmore et al., 1998).

Low-gradient, fine-grained hillslopes have longer response times. Such hillslopes generally respond by gradual retrogressive failure (Iverson and Major, 1987; Skempton, 1964), so after a perturbation such as base level fall, an earthflow prone hillslope may take hundreds or thousands of years to respond and fully adjust (Carson and Petley, 1970). Landslides can be slope clearing, removing all material down to the failure surface, and erasing much of the pre-failure topography (Densmore et al., 1997). Earthflows frequently stabilize after a period of movement preserving characteristic earthflow morphology on the slope (Keefer and Johnson, 1983), essentially redistributing mass on the hillslope which may not immediately reach the channel network. While this

complicates estimates of earthflow derived sediment flux, dormant earthflow morphology can be used to reconstruct the history of earthflow movement (Booth et al., 2009; McKean and Roering, 2004).

1.3.3. Position in the Landscape

Predictably, earthflows predominately occur in fine-grained, clay-rich lithologies (Hungr et al., 2001; Keefer and Johnson, 1983), especially in argillaceous or altered volcaniclastic sediments (Glastonbury and Fell, 2008). Topographically, Ohlmacher (2007) shows small shallow earthflows preferentially occur in regions of planar slope with low planform curvature. Iverson (1986b) notes that earthflows typically extend from the channel to the ridge, and Kelsey (1978) suggests earthflows in northern California tend to have a southerly aspect, where dry summers inhibit conifer growth on the slopes. Beyond these observations we have little data establishing where earthflows characteristically occur within a drainage basin and on hillslopes. For example, do earthflows require a critical drainage area or slope? Are they driven by failure high on the slope which coalesces and moves downhill, or does a stream bank failure progressively retrogress to the ridgeline?

1.4 Key Questions

We undertook extensive work in the Eel River catchment in northern California (Fig. 1), making detailed earthflow maps with the aid of LiDAR, aerial photography and field inspection. We ask four questions. Firstly, how much of the terrain is active? Do earthflows have a characteristic spatial attributes, or a preferential position in the landscape, such as slope, lithology, or aspect? Thirdly, do temporal patterns of movement correlate to climatic variables such as rainfall or temperature? Finally, we seek the contribution of earthflows to regional sediment flux and erosion. More specifically, how much of the sediment delivery to the channel network is attributable to earthflow activity?

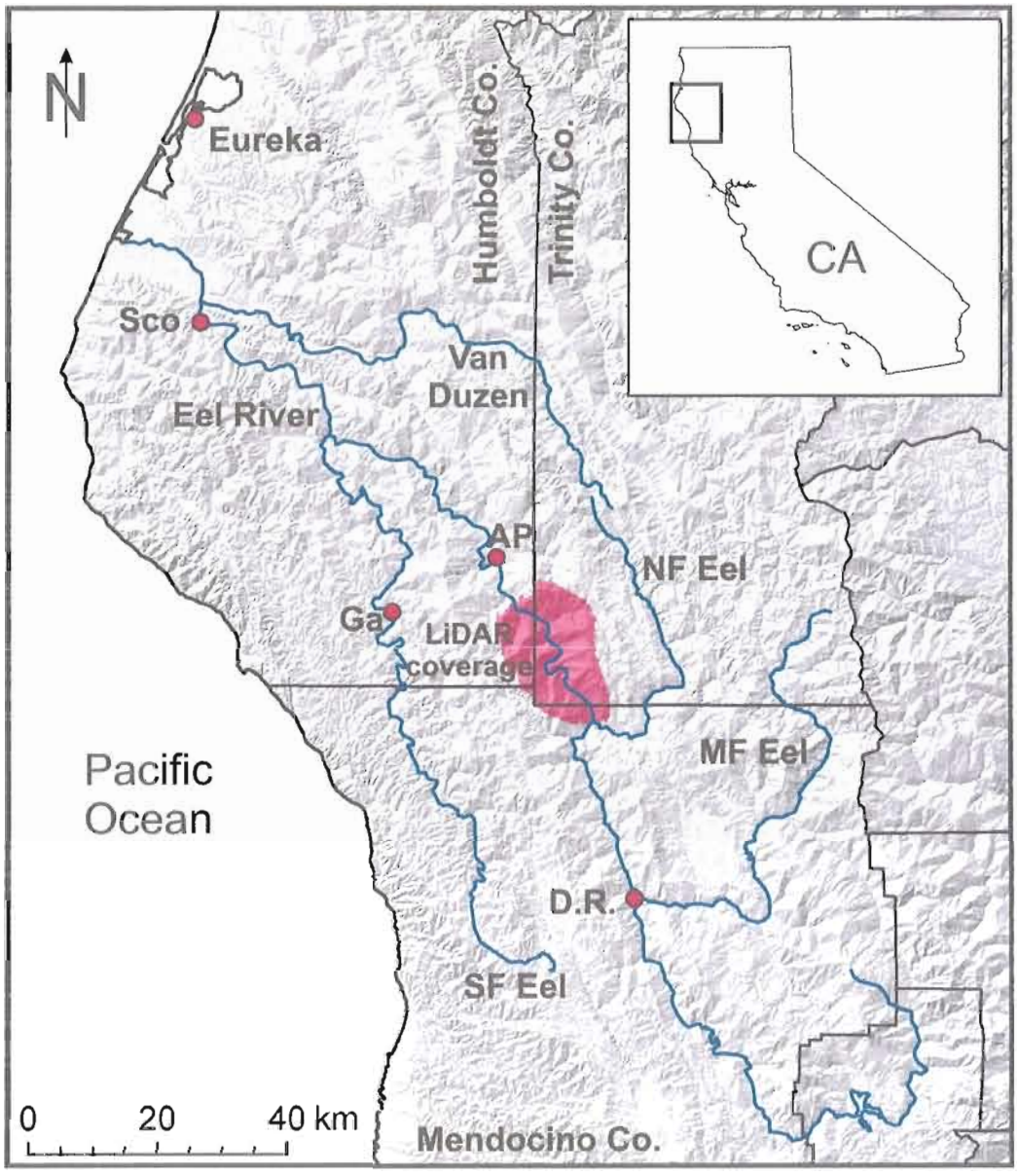

Figure 1. Location of the study area along main stem the Eel River, northern California. LiDAR data was acquired over the 230 km^2 region shaded in red. Towns mentioned: Alderpoint (AP), Dos Rios (D.R.), Scotia (Sco), and Garberville (Ga). Note the strong northwest trending structural grain visible in the shaded relief background map.

2. STUDY AREA – EEL RIVER, CALIFORNIA

2.1. Introduction

The northern California Coast Ranges are comprised of the Franciscan Complex, a Jurassic–Cretaceous penetratively sheared meta-sedimentary accretionary prism complex subject to uplift since the Neogene. Rainfall averages 1.2 m/a, primarily falling between October and May. The combination of weak mélange lithology, active tectonics, and heavy seasonal rainfall makes the Eel River watershed especially prone to landslides and slope instability, and an ideal location to study active earthflow processes.

2.2. Geology and Structure

The Franciscan Complex is comprised of three structurally separated belts, the Eastern, Central and Coastal belts. These terrains young to the west, reflecting the cumulative accretion of oceanic sediments to western North America (Jayko et al., 1989; McLaughlin et al., 2000). The Central belt is especially prone to landsliding. It runs through much of the Eel River catchment, and is structurally bound on the east by the Grogan-Red Mountain fault zone, and on the west by the Coastal belt thrust. It consists of an extensive Late Jurassic to Middle Cretaceous argillaceous mélange matrix, encompassing blocks and slabs of sandstone and shale turbidite sequences (McLaughlin et al., 2000). This assemblage was obliquely obducted to North America from 88 to 40 Ma, prior to emplacement of the Coastal Belt. Large blocks of older, meta-sandstone, meta-basalt and high blueschist-grade rocks have been incorporated into the penetratively sheared matrix of the Central belt from the older eastern units during oblique dextral translation. These more competent, erosion resistant units have a significant local influence on the topography, persisting as erosion resistant topographic highs amid the mélange (Fig. 2). The northwest trending structural grain dominates the modern topography, with major axial drainages and ridges trending northwest (McLaughlin et al., 1982).

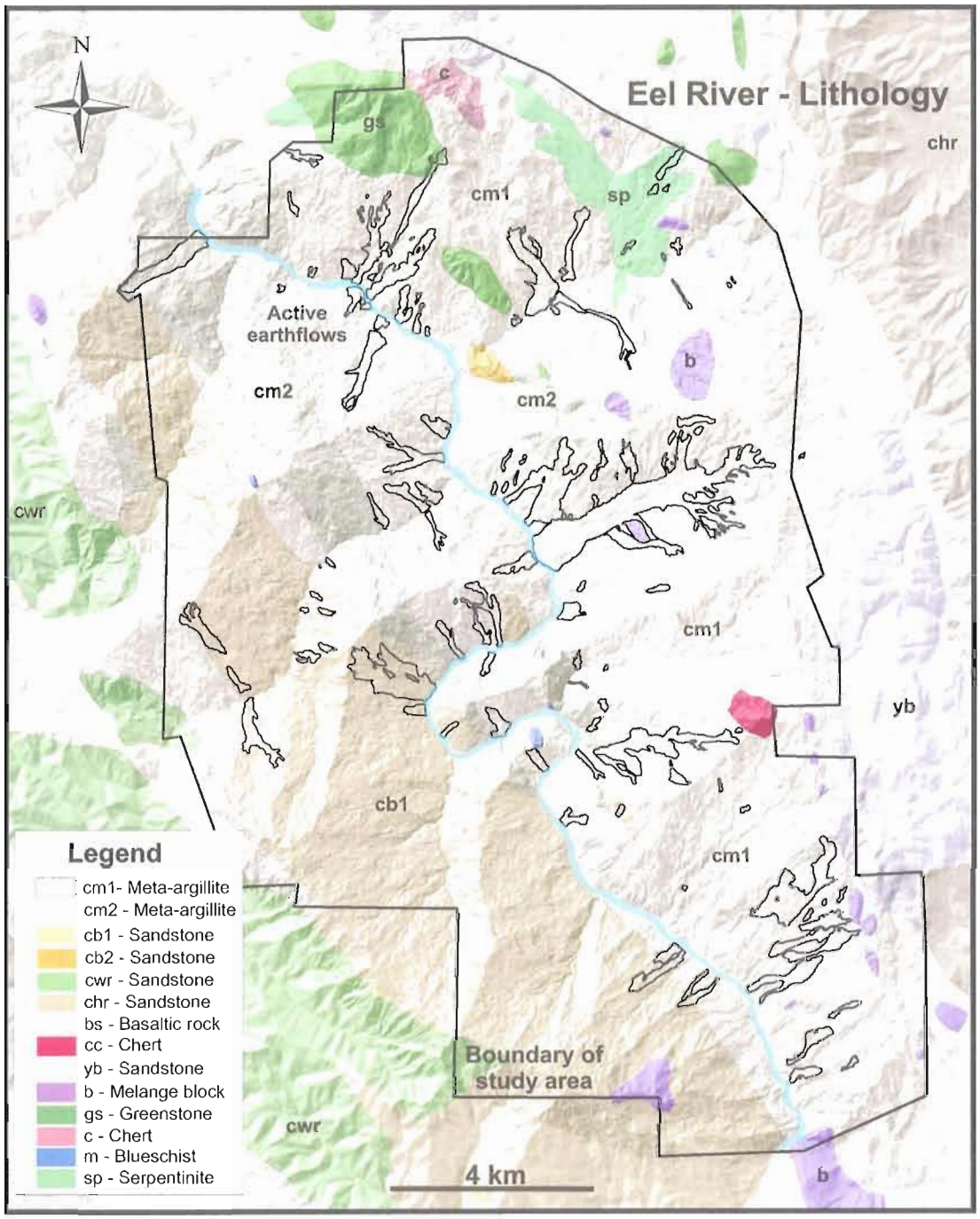

Figure 2. Simplified lithological map modified from Jayko et al. (1989) and McLaughlan et al. (2000). See Table 1 for more detailed lithological descriptions. Active earthflows and the study area extent are outlined in black, and predominantly occur in the mélange unit cm1.

The post-emplacement tectonics of northern California Coast Ranges has been dominated by the northerly migration of the Mendocino triple junction (MTJ) since the Miocene. The Pacific and Gorda plates are translating north relative to North America along the Cascadia Megathrust, creating the San Andreas Fault to the south (Furlong and Schwartz, 2004). This creates a double-humped zone of uplift which migrates north at approximately 5 cm/a (Furlong and Govers, 1999), and a series of northwest-trending emergent fault systems cut through the northern California Coast Ranges associated with the advance of the MTJ (Kelsey and Carver, 1988).

This migrating zone of uplift has had a profound influence on the landscape, causing river capture and drainage reversals. Most notably, the headwaters of the Russian River were captured by the Eel River at 2 Ma when river incision was unable to keep up with the transient wave of increased uplift rates (Lock et al., 2006), generating the unusual 'fish hook' drainage pattern of the Eel River tributaries (Fig. 1).

2.3. Uplift Rates and Erosion

Due to the high rates of erosion, many geomorphic studies have focused on the Northern California Coast Ranges. Wahrhaftig and Curry (1967) warned the rates of erosion in the Eel River (0.84 mm/a) were abnormally high in comparison to other North American river systems, and called for further research into sediment sources and monitoring. After an intensive period of hydrologic and suspended sediment data collection by the USGS in the mid century, Brown and Ritter (1971) established that from 1957–1967, the Eel River had the highest sediment yield of any non-glacial continental river in the United States at 10,000 tons per square mile (3900 tons/km^2).

Extensive research has been undertaken in the offshore environment focusing on the rate and distribution of shelf sedimentation (e.g., Nittrouer, 1999). Notable are the changing rates of sedimentation over the Holocene (Sommerfield and Wheatcroft, 2007) and in historical times (Sommerfield et al., 2002; Sommerfield and Nittrouer, 1999). In the 20th Century, the Eel River catchment experienced significant logging and road

building activities, in addition to major storms in 1955 and 1964 (Brown and Ritter, 1971; Sloan et al., 2001). Determining the relative contribution of natural versus anthropogenic effects on erosion and sediment yield has proven challenging (Sommerfield and Wheatcroft, 2007).

Rapid rates of uplift and channel incision are reflected in fluvial and marine terraces. Merritts and Bull (1989) and Merritts (1996) documented variable rates of coastal uplift peaking at 5 mm/a at the coast near to the MTJ. Uplift rates are thought to decay inland to approximately 1 mm/a near Garberville (Bickner, 1985), located on Figure 1.

A variety of approaches have been used to estimate background levels of erosion. Fuller et al. (2009) used cosmogenic isotopes and optically stimulated luminescence dating to calculate long term erosion rates for the upper South Fork Eel River of approximately 0.3 mm/a. Similarly, Gendaszek et al (2005) measured concentrations of ^{10}Be in sediments from northern California rivers, and document long term catchment averaged erosion rates of 0.8 mm/a in the upper Van Duzen, and 0.4 mm/a for the Eel River catchment near Scotia. Modern erosion rates can be estimated with suspended sediment, and Wheatcroft and Sommerfield (2005) re-analyzed suspended sediment data (1950-2000) and calculated a sediment yield of 2232 tonnes/km^2/a across the 8063 km^2 Eel River catchment, which equates to a catchment averaged erosion rate of 0.9 mm/a (assuming a bedrock density = 2.5 t/m^3). This period includes both anthropogenic effects and the mid-century storms.

2.4. Landslide and Earthflow Studies

The most comprehensive study of earthflow processes in the Eel River catchment was undertaken by Kelsey (1977; 1978; 1980) in the Van Duzen river basin, a large tributary of the Eel River at the northern end of the drainage basin (Fig. 1). Kelsey studied 19 active earthflows over a several year period in the 1970's through a combination of field surveying and aerial photo analysis, and calculated a regional

sediment budget. Although covering just 1% of the Van Duzen basin area, earthflows contributed 10% of sediment to the channel. Kelsey estimated that earthflow translation accounts for approximately 50% of the sediment flux from active features, the remainder removed by active gullies on the surface of the earthflow.

Another extensive study was undertaken farther north in the Redwood Creek catchment, looking at all aspects of sediment production and transport (e.g., Harden et al., 1995; Nolan and Janda, 1995). Nolan and Janda (1995) studied the sediment flux from two Redwood Creek earthflows, but concluded fluvial processes accounted for only 10% of the long term erosion of the earthflow complex, the majority coming from mass movement. They also stressed the temporal variability of earthflow activity across northern California, due to localized lithology and the varying topographic development of individual earthflows. Iverson (1986a; 2005; Iverson and Major, 1987) undertook extensive work on the Minor Creek earthflow in the Redwood Creek Basin, and developed a model to explain earthflow movement by the slow infiltration of winter rainfall through the landslide mass. Iverson (2005) argues movement is regulated by shear zone dilatancy, which decrease pore pressures, thus preventing catastrophic failure.

Kelsey (1980) and Muhs (1987) highlighted the role of contrasting geomorphic processes operating in different lithologies. The harder, competent, steep sandstone lithologies feature well organized ridge and valley drainage networks, with erosion dominated by fluvial debris flow incision. In contrast, the weaker mélange units have a dense but poorly developed ephemeral drainage network, longer low gradient slopes, and erosion is dominated by earthflow and mass movement processes. Despite this weak lithology, rivers frequently steepen when they cross weak mélange, as earthflows deliver boulders to the channel which armor the bed (Kelsey, 1977, 1978).

2.5. Main Stem Eel River Study Area

Our study focuses on a section of the main stem Eel River between Dos Rios and Alderpoint (Fig. 1), which has one of the highest concentrations of earthflow activity in

the Eel River catchment (Brown and Ritter, 1971). Lithology in this area is predominantly argillaceous mélange of the Central belt Franciscan Complex (Fig. 2), characterized by long, low gradient slopes and extensive slope instability. The mélange was open oak grassland at the time of European settlement in the 1850's, attracting ranchers, and the primary land use remains low-density cattle ranching. Conifer growth and forestry are generally limited to isolated sandstone outcrops. The Northwestern Pacific Railway follows the main stem Eel River canyon, connecting Eureka to San Francisco, but this line was abandoned in 1998, partially due to the high cost of landslide related maintenance.

Descriptions of the large landslides and earthflows along the Eel River canyon between Dos Rios and Alderpoint have largely been confined to a variety of engineering reports for the California Department of Water Resources (Dwyer et al., 1971; Scott, 1973; Smith et al., 1974), primarily in anticipation of dam construction over much of the Eel River catchment (California Department of Water Resources, 1965). These were largely reconnaissance studies with descriptions of the landslides and analysis of the earthflow material. They included estimates of landslide generated sediment flux, although with limited information on slide depth and long term movement rates. Malhase (1938) described the Mile 201 landslide after a wet winter in 1938: "the surface of the slide takes on the characteristic form of mud glaciers, with lateral terminal moraines, with rolls and pressure ridges forming valleys and hummocks. Great cracks open up into which water from the surface enters."

More recently, Mackey et al. (2009) studied an earthflow on Kekawaka Creek, a tributary to the Eel River, and highlighted the variability of temporal movement and the longevity of earthflows in the landscape. Roering et al. (2009) used satellite-based InSAR to monitor seasonal movement of the Boulder Creek landslide, and estimated a minimum erosion rate of 1.5 mm/a across the earthflow source area. Brown and Ritter (1971) calculated a 2 mm/a erosion rate for the 1701 km^2 catchment area of the Eel between Dos Rios and Fort Steward between 1965 and 1967, although this period was in the aftermath of the 1964 flood and may be elevated beyond background rates.

Very little data exists on the depth of large landslides and earthflows along the Eel River. The exceptions are 2 landslides in the lower reaches of the Middle Fork Eel River (California Department of Water Resources, 1970), approximately 34 km southeast of our study area, but in comparable Central belt Franciscan lithology. Boreholes in the 1.6 km long, 0.45 km^2 Salt Creek landslide, 3.5 km upstream of Dos Rios, revealed landslide colluvium thickening from 6.7 m near the headscarp, to depths of 33 and 35 m towards the toe. The larger 0.64 km^2 1 km long Salmon Creek landslide is 16 km upstream from Dos Rios. A drill hole in this landslide was sheared off at 34 m depth, although the inclinometer also detected small amounts of movement at 57 m, attributable to deep seated failure within the sheared shale bedrock.

3. METHODS – MAPPING EARTHFLOW ACTIVITY WITH HIGH RESOLUTION TOPOGRAPHY AND PHOTOGRAMMETERY

3.1. Background – Landslide Mapping

Landslide mapping has traditionally been undertaken by a combination of stereo pair aerial photo and topographic map analysis, in concert with some field verification. Aerial photo analysis can efficiently cover a large area, but at the expense of accuracy – especially in forested terrain, and problems arise in accurately relocating features on a photograph to the base topographic map (Malamud et al., 2004). Field mapping yields greater accuracy (especially with modern GPS technology), but at the expense of high labor costs and the limited extent of terrain that can be covered (Wills and McCrink, 2002). In recent years satellite-based InSAR mapping has proven effective in locating slow sustained mass movement (Hilley et al., 2004; Leprince et al., 2008). The C-band PALSAR ALOS satellite has achieved success mapping earthflows in mountainous and vegetated terrain (Roering et al., 2009), although data only extends back to 2006.

The increasing availability of high resolution topography acquired through airborne laser swath mapping (Light detection and ranging or LiDAR) has greatly enhanced the ability of researchers and practitioners to map mass movement features

across a broad area. LiDAR based mapping allows greater accuracy in both correct feature identification and location than is available with traditional aerial photo and field mapping approaches. This has been particularly evident in landscapes with deep seated landslides and slump features occurring in glaciated or generally uncomplicated topography, such as the Puget Sound area in Washington (Schulz, 2007), and the layered basalts in southern Idaho (Glenn et al., 2006). In these landscapes, the margins of landslides are easily recognized on LiDAR imagery as they have a distinctly different visual and statistical surficial texture in comparison to the surrounding unfailed terrain (Booth et al., 2009; McKean and Roering, 2004).

In landscapes prone to pervasive slope instability with multiple generations of landsliding, distinguishing between historically active and long dormant mass movement can be difficult, even with the LiDAR derived meter-scale topographic maps. While the Lidar maps have been a great improvement on previous approaches, confidently mapping mass movement in terrain with multiple episodes of deep seated failure remains a challenging and largely subjective exercise (Van Den Eeckhaut et al., 2005).

Despite this uncertainty, qualitative estimates of earthflow activity state or age can be made from landslide morphology. Over time, morphological features attributable to landslide movement (e.g sharp headscarps, tension cracks, compressional folding and lateral margins) become smoothed out and attenuated by small scale surficial or diffusive processes (e.g soil creep, bioturbation) when a landslide stops moving (Gonzalez-Diez et al., 1999; Wieczorek, 1984). Figure 3 shows earthflows adjacent to the Eel River which qualitatively appear to span a range of activity states. Two currently active features with fresh kinematic structures adjoin a dormant landslide, where much of the small scale morphology has been erased, leaving subtle headscarps and lateral margins.

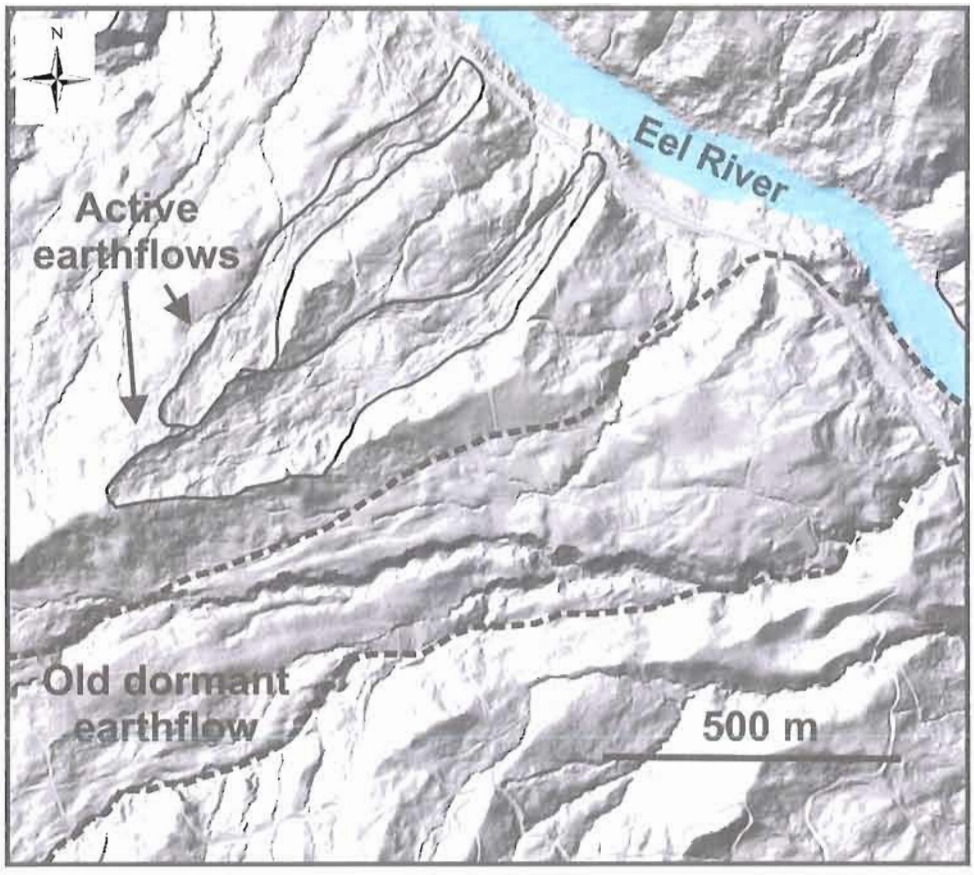

Figure 3. Active vs. dormant earthflow morphology. Two active earthflows show sharp morphological features, whereas a large dormant earthflow to the south has had much of the finer scale morphology attenuated by surficial processes. The Northern Pacific Railroad runs along the southwest side of the Eel River

Visual inspection of bare earth LiDAR shaded relief maps in the Franciscan mélange of northern California reveals a wide range of landslide and earthflow features. Slope failure ranges from small slumps to huge earthflow complexes (Brown and Ritter, 1971; Kelsey, 1978; Mackey et al., 2009). Complicating the mapping process, on a single hillslope, earthflows often exhibit complex cross-cutting and nested relationships, and span a range of size, activity state and failure style.

3.2. LiDAR

The National Center for Airborne Laser Mapping (NCALM) acquired a high resolution LiDAR dataset of the study area in September 2006 (Fig. 1). The raw data was processed by NCALM, who produced ESRI-compatible grids of elevation in January 2007. The elevation grids included both unfiltered elevation (trees and buildings are recorded and show up in the data), and filtered data, where algorithms filter out vegetation and structures, leaving the bare earth elevation (Carter et al., 2007; Slatton et al., 2007).

3.3. Photo Orthorectification

The earliest extensive aerial photo set covering our field area in the Eel River catchment was flown in 1944 by the Department of Defense. These 1:24000 scale photos are of high quality; trees, buildings, and subtle topographic features are readily identifiable. We acquired medium resolution (800 dpi) scans of the photos extending over the field area (Appendix D).

For quantitative analysis, aerial photographs must be referenced to the ground, and rectified to remove lens distortions and topographic effects (Wolf and Dewitt, 2000). This requires the calibrated focal length of the lens, the coordinates of fiducial markers on the edge of the photo, a digital elevation model of the terrain, and ground control points to co-locate features on the photo with features on the ground.

We were not able to locate camera information or calibration reports for the 1944 series of photos, but estimated the focal length (210 mm) from a database of typical camera specifications (Slama, 1980). The coordinates of fiducial marks around the margins of the photos were measured manually on true scale scans in Corel Draw graphics software to within 0.005mm. We assumed a perfect principal point of focus (x,y = 0,0) to construct the photo coordinate system. We used the 1 m^2 LiDAR bare earth elevation as the elevation model, and the unfiltered 1 m^2 LiDAR shaded relief as a reference image to rectify the photographs within ERDAS Imagine 9.3 software. For

ground control points, we identified features such as small trees, buildings, or rock outcrops on unequivocally stable terrain (such as ridges and terraces) and co-located the identical features on both the LiDAR shaded relief image and the photo.

We compared the position of stable features on the LiDAR with the rectified photos across the study site, to estimate error. Through this process, we could rectify the photos with a high degree of accuracy (~2 m), and relocate features on the photos as they were placed on the ground in 1944.

3.4. Objectively Quantifying Earthflow Movement

The earthflows of the Eel River catchment commonly have oak trees and bushes growing on the earthflow surface. These trees continue to grow on the landslide mass as it translates downhill, and are readily identifiable in sequential photographs, on unfiltered LiDAR maps, and in the field. By comparing differences between the 1944 photos and the unfiltered LiDAR data acquired in 2006, we were able to track the locations of individual trees and construct a series of displacement vectors for the 62 year time interval. We use this approach to objectively map historically active earthflows, and discriminate between stable and moving terrain.

The distribution of trees varies across the study area, and between different earthflows. Some earthflows have many long-lived trees that can be used to construct a detailed vector field of displacement (Fig 4.), whereas on other earthflows trees are sparse and the extent of movement is more difficult to objectively discern with tree displacement vectors alone. To delineate the margins of earthflows we used an iterative approach, carefully comparing the rectified 1944 photos and the LiDAR imagery. The primary guide to mapping the earthflow margin was the comparison of stable and moving trees, which show a clear offset on active earthflows. The margins of active earthflows typically feature a subtle morphological structure, such as a headscarp or lateral levee, or toe lobe thrust, and we used these morphological features to guide fine scale margin construction.

Figure 4. Unfiltered shaded relief map of the Boulder Creek earthflow. Margins of active earthflows outlined in black, with individual tree displacements in red. Inset shows displacement at the mid-section of the flow, where it crosses a structural barrier running obliquely across the transport zone – note the large toe advancing from the northeast. The Lone Pine earthflow (L.P.) is to the northwest. Eel River runs south to north along the toe of the Boulder Creek earthflow. Coordinates are UTM Zone 10N.

4433000
4434000
4435000
4436000
4437000
462000
461000
460000
459000
458000
457000
150 m

In areas with few or no trees suitable for quantifying displacement, we could often observe movement based on changing earthflow morphology. For example, advancing toe lobes or headscarp retrogression can be readily identified by comparing the photos with the LiDAR maps. We took a conservative approach to mapping: if we could not confidently map either vegetation displacement or morphological change, we did not include the terrain as an active earthflow. Where we mapped displacements in different parts of one contiguous earthflow, we amalgamated these into one larger contiguous feature when justified by morphology. Additionally, we distinguished stable patches within a larger earthflow from the neighboring mobile terrain.

We visited earthflow features in the field over 4 field seasons to confirm the reliability of our technique. On the ground, active earthflows exhibit fresh headscarps, exposed 'mole-track' lateral margins with slickensides (Fig. 5a), disturbed, densely cracked hummocky terrain (Keefer and Johnson, 1983; Kelsey, 1978), and occasionally trees which have been stressed, toppled or killed by ground disturbance (Fig. 5b). Conversely, stable or dormant earthflows, while retaining much of the hummocky terrain and characteristic earthflow morphology, do not exhibit the same degree of fresh ground disturbance (Fig. 3).

We mapped earthflow features as detailed polygons using ESRI ArcMap 9.2 software, and constructed a statistical database on the individual earthflows. By combining LiDAR, rectified photos and field inspection, we objectively mapped landslide movement (>5 m) over the 62 year interval.

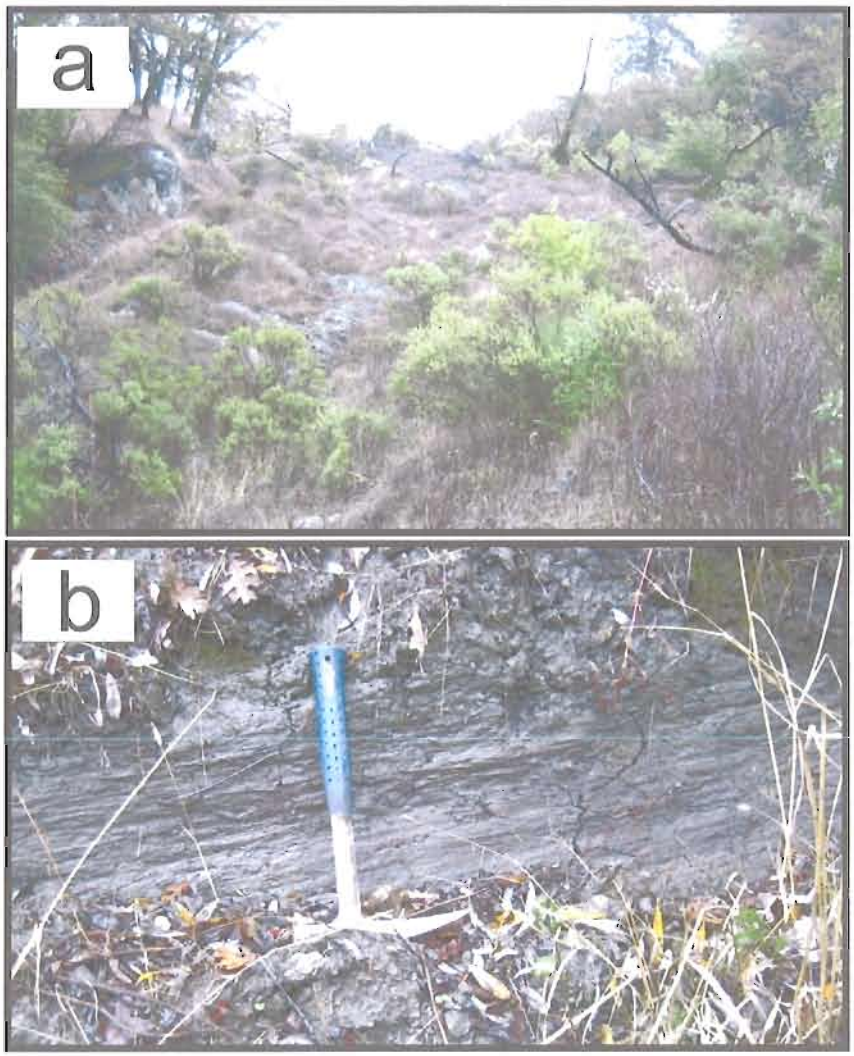

Figure 5. Field evidence for earthflow activity. a) View up the active Penstock earthflow, showing the disturbed ground and distressed trees. b) Lateral margin of an active earthflow showing slicken lines.

3.5. Earthflow Displacement Time Series

On 16 earthflows with sufficient displacement (>30 m over the 62 year period), we used sequential aerial photos to construct a time series of earthflow movement, following the approach of Mackey et al. (2009). We calculated velocities for trees in the transport zone, the sections of the earthflows which are most sensitive to climatic changes (Bovis and Jones, 1992), and where displacements are greatest. Although the aerial photo coverage varies across the study site, we were able to reconstruct the

temporal pattern of movement at approximately the decadal scale. With our resolution (generally 4–10 years between photos), we expect to observe longer term earthflow behavior, such as decadal-scale climatic patterns (Bovis and Jones, 1992), rather than the effect of individual storms or seasonal movement.

In the aerial photo rectification process there is frequently a small positional error, which can propagate through calculations of earthflow velocity. To correct for this, in addition to tracking the position of trees on the earthflow through time, we also tracked the apparent position of stable trees through the same photo series. We were then able to differentially correct the apparent movement of the stable feature from the displacement record of the moving tree.

3.6. Climate

One of the primary factors governing movement of many landslides is climatic change, notably changes in precipitation, groundwater levels, and temperature. The longest climatic record near the field area is located on the Eel River at Scotia (Fig. 1), 65 km to the northeast of the study site (USGS Site 11477000 Latitude 40°29'30", Longitude 124°05'55"). Continuous daily temperature, precipitation and river discharge records date back to the 1920's.

We calculated statistics each water year (starting October 1st) for discharge, temperature and precipitation. Groundwater level is both a critical control on landslide movement, and a primary factor in sustaining channel baseflow. As such, we use the 25th percentile of daily annual discharge (Q_{25}) as a proxy for base flow. Additionally, lower percentile flow measurements have been shown to be a more sensitive recorder of climatic trends (Lins and Slack, 1999; Luce and Holden, 2009).

3.7. Sediment Production

We distinguished earthflows which discharge sediment directly into a channel or major gully from flows which are unconnected to the channel network and do not represent active sediment sources. To calculate the sediment delivery attributable to mass movement from the earthflow to the channel, we multiplied the average annual toe movement rate (from the photo-derived vectors) by the width and depth of the earthflow at the toe (Fig. 6). We have no direct data as to the depth to the failure surface (e.g. from drill holes), but can estimate from the height of the steep toe face where an earthflow reaches the channel. We used the depth data from the Middle Fork Eel River earthflows to guide depth estimates of the larger features in our study area. We assigned uncertainties of 25% for the depth, 10% for the width, and 10% for the velocity when calculating sediment flux from each individual earthflow.

By integrating the sediment contributed by the earthflows across the study area, we can estimate the total sediment flux attributable to earthflow mass movement. Dividing this sediment delivery rate (m^3/a) by the study area (m^2) gives the earthflow driven erosion rate.

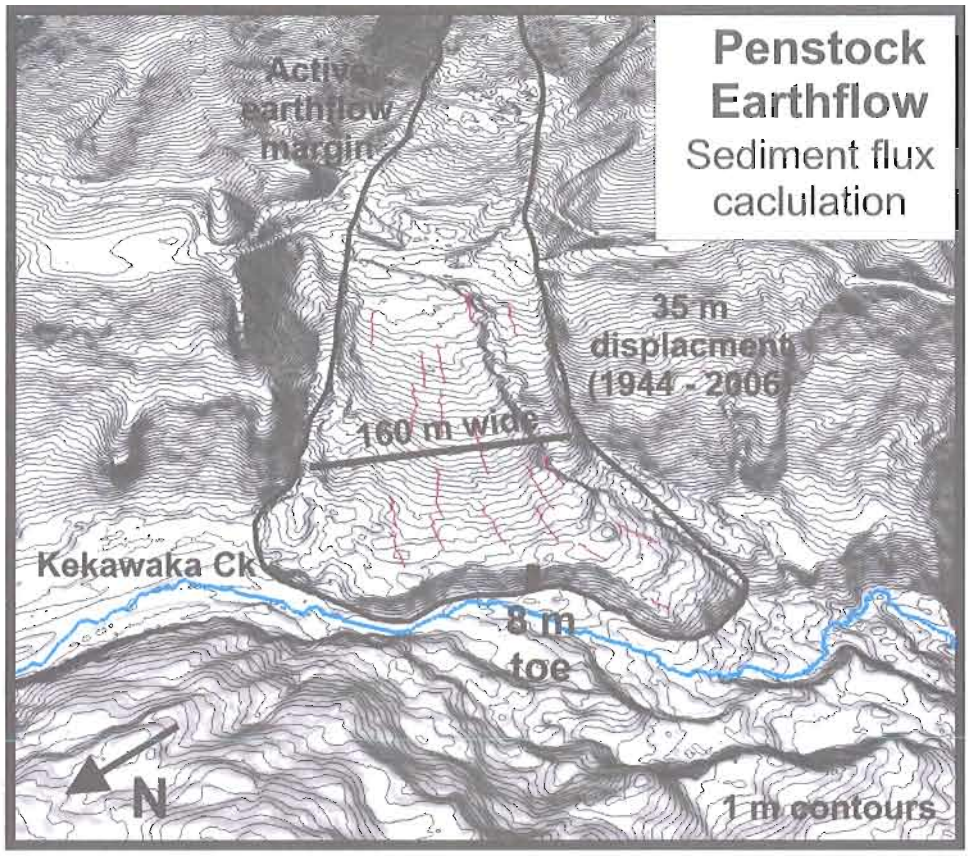

Figure 6. Oblique view of the Penstock Earthflow looking southeast across Kekawaka Creek, illustrating the measurements taken to estimate sediment flux from each earthflow.

4. RESULTS

4.1. Spatial Distribution of Earthflows

The spatial distribution of active earthflows is presented in Figure 7. Across our study area along the Eel River, we identified 122 earthflow features that moved during the interval 1944–2006.

Figure 7. Map of the 226 km^2 study area, active earthflows, and tree displacements, from 1944 to 2006. Extent of LiDAR coverage is shown as shaded relief, colored by elevation. Background image is 30 m grid shaded relief, and coordinates are UTM Zone 10N.

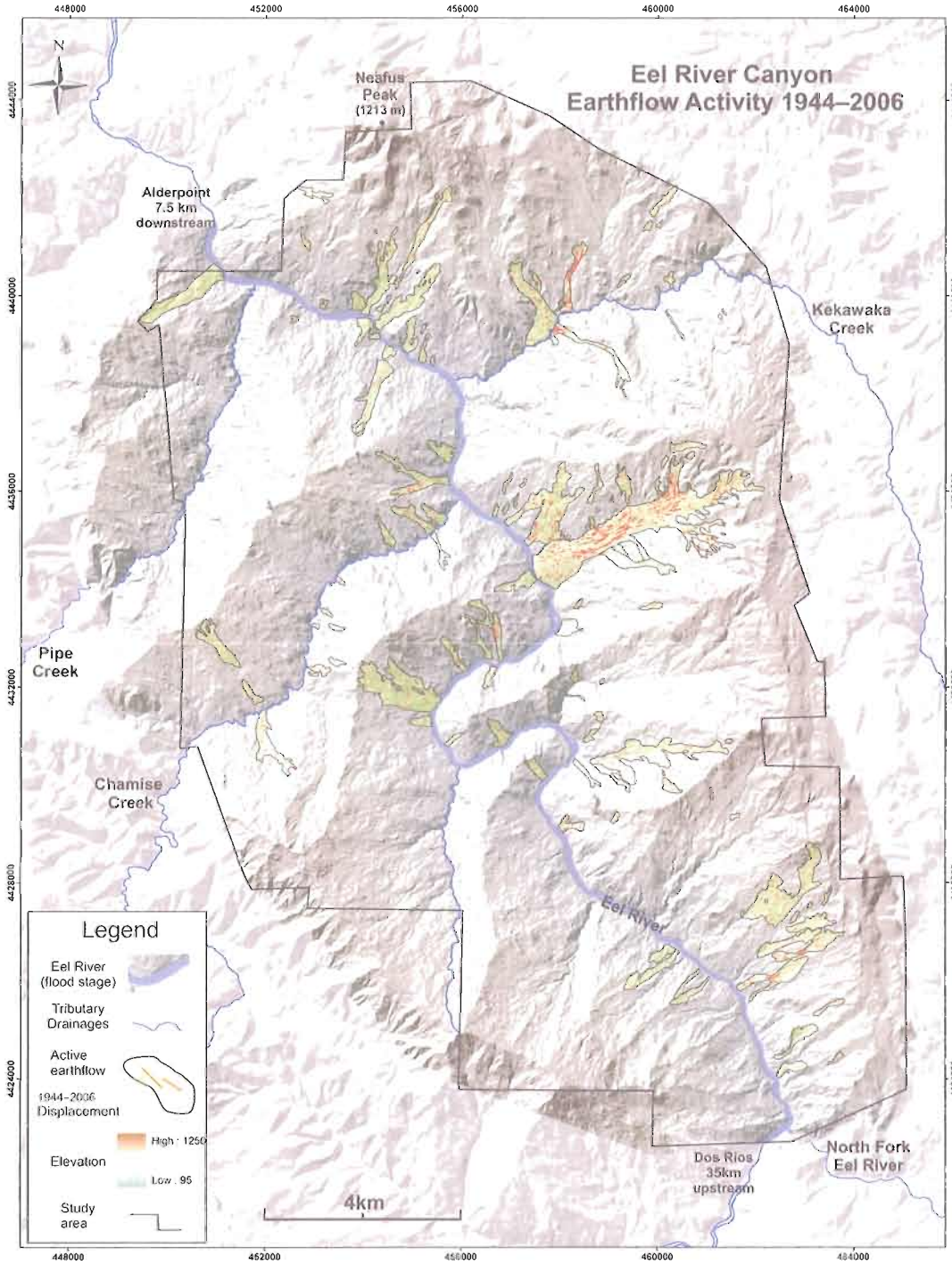
Eel River Canyon
Earthflow Activity 1944–2006
N
Neafus Peak (1213 m)
Alderpoint 7.5 km downstream
Kekawaka Creek
Pipe Creek
Chamise Creek
Eel River
Dos Rios 35km upstream
North Fork Eel River
4km
Legend
Eel River (flood stage)
Tributary Drainages
Active earthflow
1944–2006 Displacement
Elevation
High : 1250
Low : 95
Study area
448000
452000
456000
460000
464000
4444000
4440000
4436000
4432000
4428000
4424000

4.1.1. Earthflow Shape and Area

Across the study area of 226 km^2, we mapped active earthflows covering 16.5 km^2, indicating 7.3% of terrain moved between 1944 and 2006. The 122 earthflows have a median area of 36,500 m^2, with an inter quartile range of 12,500–117,000 m^2. Figure 8 shows histograms and a cumulative probability plot of earthflow area. The distribution of earthflow areas appears to display 2 power law relationships, one with an area from 6.0×10^3 to 6.0×10^4 m^2, and a second when area exceeds 6.0×10^4 m^2. The largest active earthflow in the study site, the Boulder Creek earthflow (3.1×10^6 m^2), is over 3 times the area of the next largest feature, the Island Mountain slide (0.94×10^6 m^2). The group of earthflows with area less than 6.0×10^4 m^2 has an average aspect ratio (width/length) of 4.2 ± 2.7. In comparison, when earthflow area exceeds 6.0×10^4 m^2 the ratio is 7.3 ± 4.2 showing the larger earthflows are typically more elongate.

Many earthflows have intricate planform shapes, often with several small tributary flows coalescing to form the primary earthflow (Fig. 4). Stable regions can persist within an earthflow complex, surrounded by moving terrain. The earthflows generally extend from the channel up to a ridgeline or major break in slope. Earthflows which do not extend longitudinally along the full slope length are most commonly restricted the upper parts of the hillslope (Fig. 7).

4.1.2. Earthflow Displacement

In total, we tracked the displacement of 998 features (trees or rocks) distributed across the 122 earthflows, generating an average density of 1 displaced feature every 1.7×10^4 m^2 of earthflow terrain. Median displacement was 23.9 m, with an inter-quartile range of 14.6–42.3 m (Fig. 9a). Displacements ranged from 4.1 to 175 m, with a mean of 34.6 m. Over the 62 year interval, the median earthflow velocity across all moving features was 0.4 m/a. By comparing the locations of stable features both on the photo and the LiDAR we estimated the error associated with photo rectification. Rectification error was small in comparison to the displaced trees, with a median error of 2.1 m (Fig. 9b).

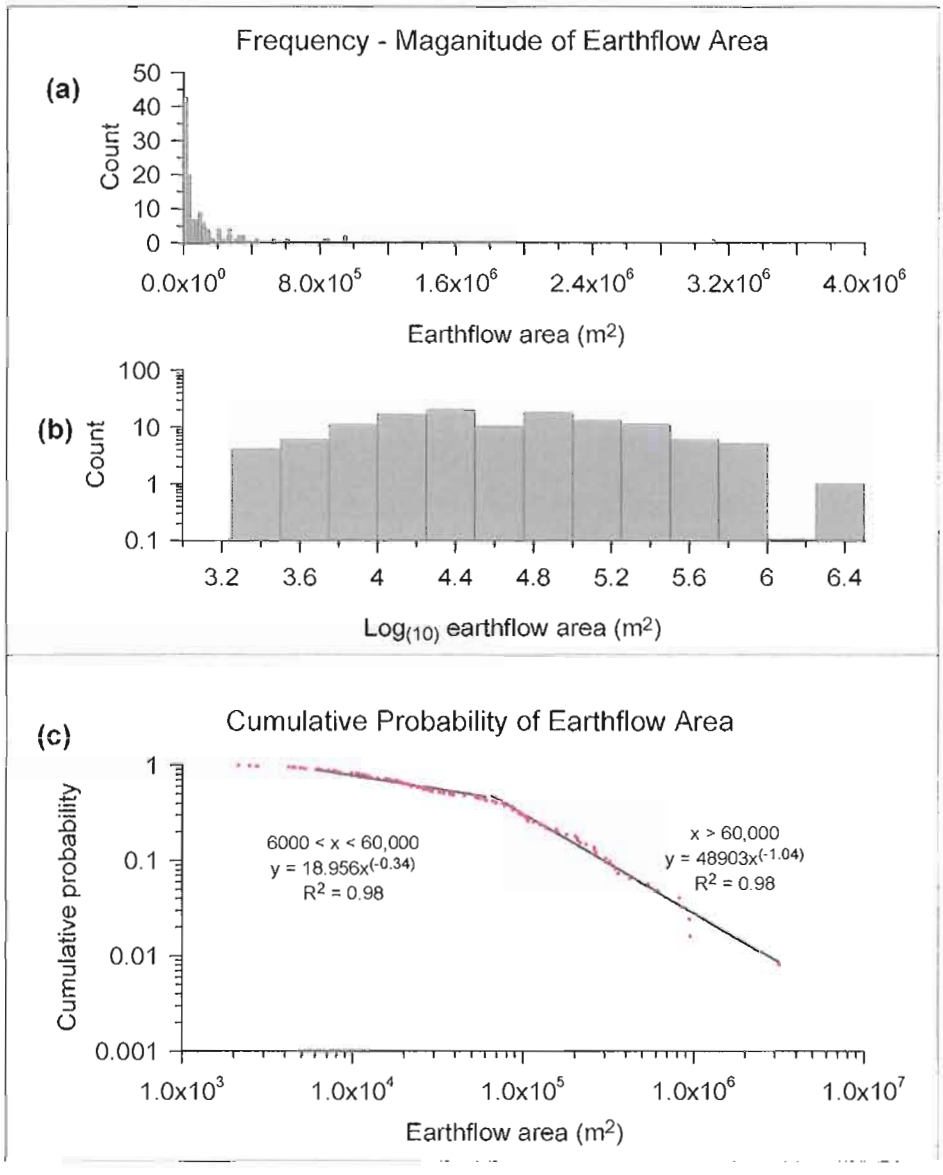

Figure 8. Earthflow areas. a) Histogram of earthflow area. b) Log-log plot of earthflow magnitude-frequency. c) Cumulative distribution plot of earthflow area. The distribution exhibits two power laws, with a scale break at approximately 6×10^4 m^2.

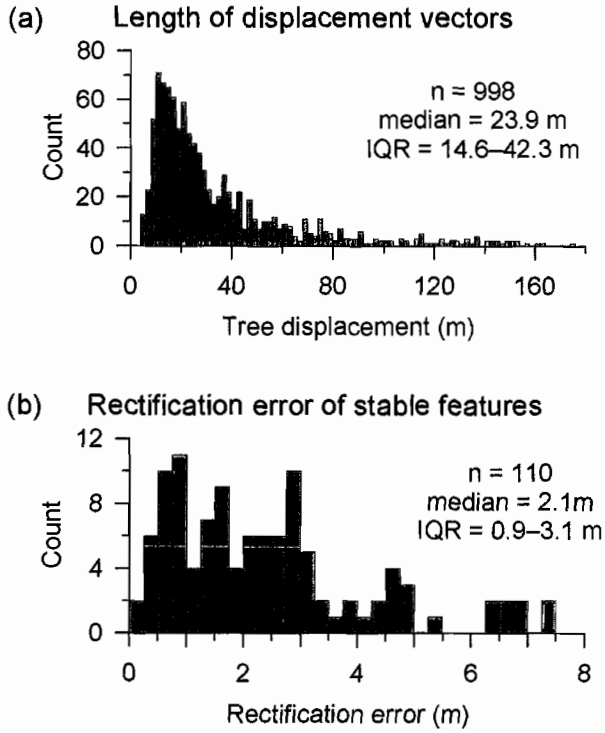

Figure 9.
a) Histogram of 998 tree displacements.
b) Histogram of rectification errors, calculated from the offset between stable features on the photo and LiDAR. Note the scale change from Figure 9a.

4.1.3. Slope and Lithology

We calculated the longitudinal slope of each earthflow (headscarp to toe), in addition to the summary statistics of cells within each earthflow polygon. To compare earthflow topography to the study area as a whole, we recorded the slope of all cells over the extent of the study area.

The longitudinal slope has a normal distribution with a mean slope of 31±7% (mean ± standard deviation). Figure 10 shows the zonal earthflow slope is higher at 36%, accounting for the increased variability of individual cell slopes within each earthflow polygon. The mean slope of the 122 earthflows is nearly identical to the mean slope of

the study area (36.5%), although the study area slope is more broadly distributed, and slightly tailed, possibly accounting for gorges, cliffs, and steeper sandstone units.

Our distribution of earthflow slopes are comparable to those compiled by Keefer and Johnson (1983) for smaller earthflows in the San Francisco Bay area, which clustered on slightly steeper slopes of 20–22 degrees (36–40%).

Figure 2 illustrates the lithology of the study area, modified from Jayko et al. (1989) and McLaughlin et al. (2000), and Table 1 documents the number and area of earthflows in each lithology. Of the 122 earthflows, 98 (82% of the active earthflow area) occur in the penetratively sheared mélange unit (cm1).

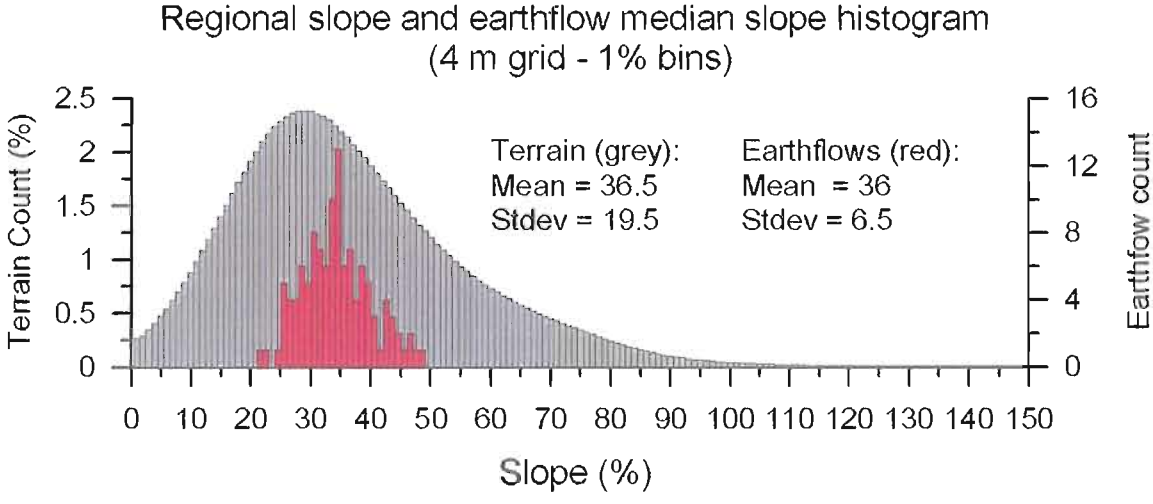

Figure 10. Histogram is slope of all 4 m cells within the study area (grey). Red histogram is median slope of 4m cells within each earthflow polygon.

Lithology	Symbol	Area (m^2)	% study area	No. EF	EF area (m^2)	% EF area	% lith active
Mélange – penetratively sheared meta-argillite	cm1	1.32×10^8	58.2	98	1.33×10^7	80.89	10.08
Broken Fm (Metasandstone)	cb1	5.75×10^7	25.4	16.5	2.10×10^6	12.71	3.65
Mélange (Subequal argillite and sandstone)	cm2	1.88×10^7	8.3	2.5	5.64×10^5	3.42	3.00
Serpentinite	sp	4.67×10^6	2.1	5	1.63×10^5	0.99	3.49
Greenstone	gs	4.14×10^6	1.8				
Block (unknown lithology)	b	2.66×10^6	1.2				
Yolla Bolly (metasandstone)	yb	2.61×10^6	1.2				
Radiolarian Chert	c	1.02×10^6	0.5				
White Rock (meta-sandstone)	cwr	1.23×10^6	0.5				
Basaltic Rocks	bs	6.86×10^5	0.3				
Broken Fm (intact metasandstone)	cb2	4.16×10^5	0.2				
Chert	cc	5.57×10^5	0.2				
Blueschist Blocks	m	1.29×10^5	0.1				
	Total	2.26×10^8	100.0	122	16.5×10^7		

Table 1. Proportion of lithology and active earthflows (EF) across the study area.

4.1.4. Aspect

Kelsey (1978) noted that earthflows along the Van Duzen River tended to have a southerly aspect. To test this along the Eel River, we took the median aspect of 4 m cells within each earthflow polygon (Fig. 11a). The mean earthflow aspect is 210° with a mean resultant vector of 0.42. Applying Rayleigh's test for significance of a mean direction, for this dataset the critical resultant vector (α 0.05, $n > 122$) is 0.17, indicating the earthflows do have a significant mean southwesterly aspect.

Given the strong northwest structural control on topography, we also plotted the aspect of all 4m cells within the study area to determine whether this biased the aspect of earthflows. Figure 11b highlights the asymmetry of regional aspect, with an oblate circular histogram showing a slight predominance of cells facing the southwest. The mean direction of all topography is 248° with a small mean resultant vector of 0.04. The critical resultant vector ($\alpha = 0.05$, $n >> 100$) is 0.17, so we can't reject the null hypothesis that there is a preferred orientation of the terrain.

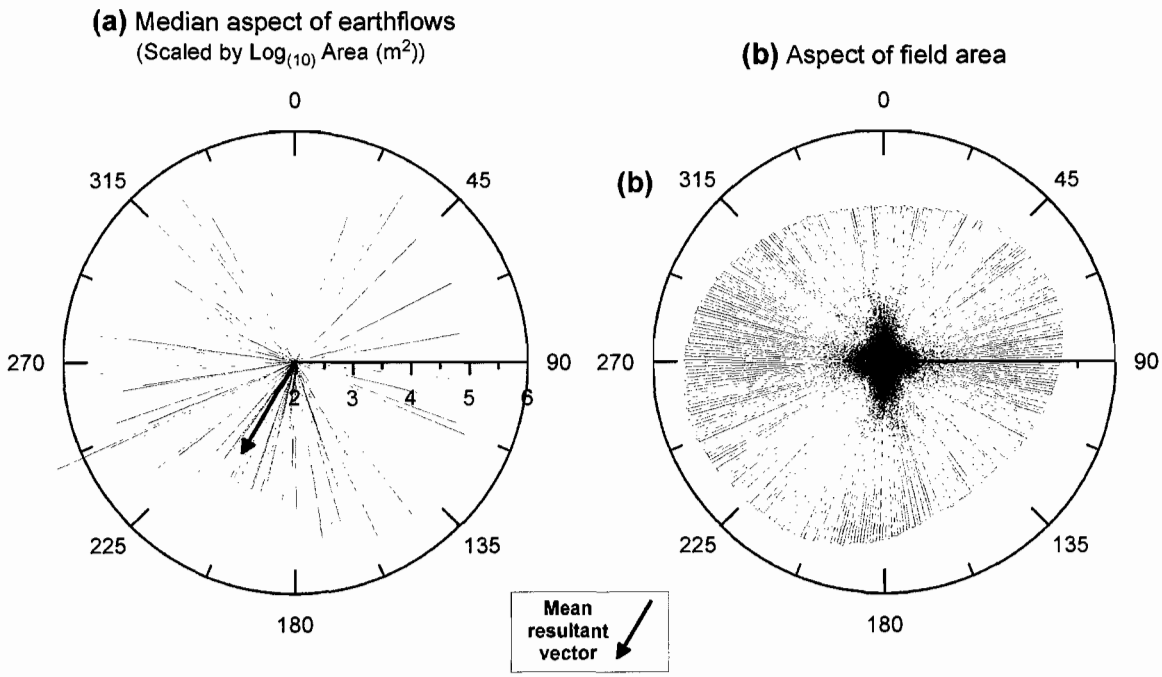

Figure 11. Aspect of earthflows and the study area. (a) Median aspect of 4 m cells within each earthflow polygon, scaled by Log_{10} area (m^2). Mean resultant vector is 210°. (b) Radial histogram of aspect of 4 m cells across the field area. Mean resultant vector is 248°.

To see if the earthflow aspect trend is significantly different from the terrain as a whole, we compared the datasets of earthflow and terrain aspect and performed an F-Test. The two aspect datasets have a calculated F = 53. The critical F value at (α=0.05) is 3.8, so therefore we can reject the null hypothesis that the two populations were drawn from populations with the same mean, and the aspect preference of earthflows is significant.

4.2. Temporal Distribution of Earthflows

In addition to mapping the earthflows which moved between 1944 and 2006, we were able to construct time series of velocity for 16 earthflows. We grouped the earthflows into three categories based on the temporal pattern of movement. Figures 12–14 show the temporal velocity of these earthflows, in addition to the outline and topographic setting of each feature.

Group 1 slides show fast (3–4 m/a) velocities from 1944 through to the late 1970's (Fig. 12). These velocities were sustained or increased through the 1960s, and have gradually decayed since 1981. Earthflows in this group, especially the Kekawaka, Boulder Creek and Rapids features, have some of the most classical earthflow morphologies in the study area, with a long, well defined transport zone and have the greatest cumulative displacements. These earthflows all discharge to a major channel. The Marge earthflow moved a negligible amount after 1968, although this is a small and recent looking feature, and could arguably be classed differently.

In Group 2 (Fig. 13), the earthflows exhibited fast velocities (3–4 m/a) in the first photographic intervals from 1944, and have steadily declined since, with little movement beyond 1981. Three of the 4 earthflows in this group (Laufer, SE-1 and SE-2) are high on the hillslopes and have no connection to major channels. White Lower has evidence of activity all over the earthflow, although due to landscaping during railway operation we could only track trees in the upper section of the earthflow. We have no information about transport zone velocity of this feature, and it conceivably has a different temporal

pattern of movement than suggested by the trees near the headscarp. The adjacent 201 landslide required 2560 bulldozer hours for landscaping extensive drainage installation (Dwyer et al., 1971) which would overwhelm the natural behavior of these earthflows.

The third and largest group of slides has velocities which were generally low (<2 m/a), and show steady movement with occasional surges (Fig. 14). A characteristic of these earthflows is an unusual planform shape. For example, the Island Mountain earthflow is a large wide feature, which showed a lot of internal variability in the rate and amount of sliding. Some of the earthflows exhibit surges over 1–2 photo intervals, such as Lone Pine or SE-3. This group of slides generally had less displacement than the other groups (40–60 m). Six of the eight earthflows have a tight connection with a major channel at the toe, and sustained toe erosion may promote a slow steady movement which overwhelms other factors such as rainfall.

4.3. Climate

Annual rainfall, plotted in Figure 15, is low from the 1920's until the 1940's but thereafter does not exhibit any obvious long term trends, although the 5 year running mean highlights an approximately cyclical decadal pattern. Rainfall from approximately 1940 to 1977 does not show the inter-year variability of other periods, and Syvitski and Morehead (1999) note there is a slight increase in precipitation (and mean annual discharge) over the mid portion of the century. Similarly, the 25th percentile of annual mean daily discharge at Scotia is low in the 1920's and 1930's, but increases from 1940 to 1960. Thereafter, increasing variability is superimposed on a gradual decline since ~1980. A second order polynomial fit highlights this pattern (Fig. 15). Conversely, mean annual daily temperature decreases over the mid century, with a temperature decrease on the order of 1°C. Again, a second order polynomial fit highlights how mean annual daily temperatures were depressed from approximately 1940–1980.

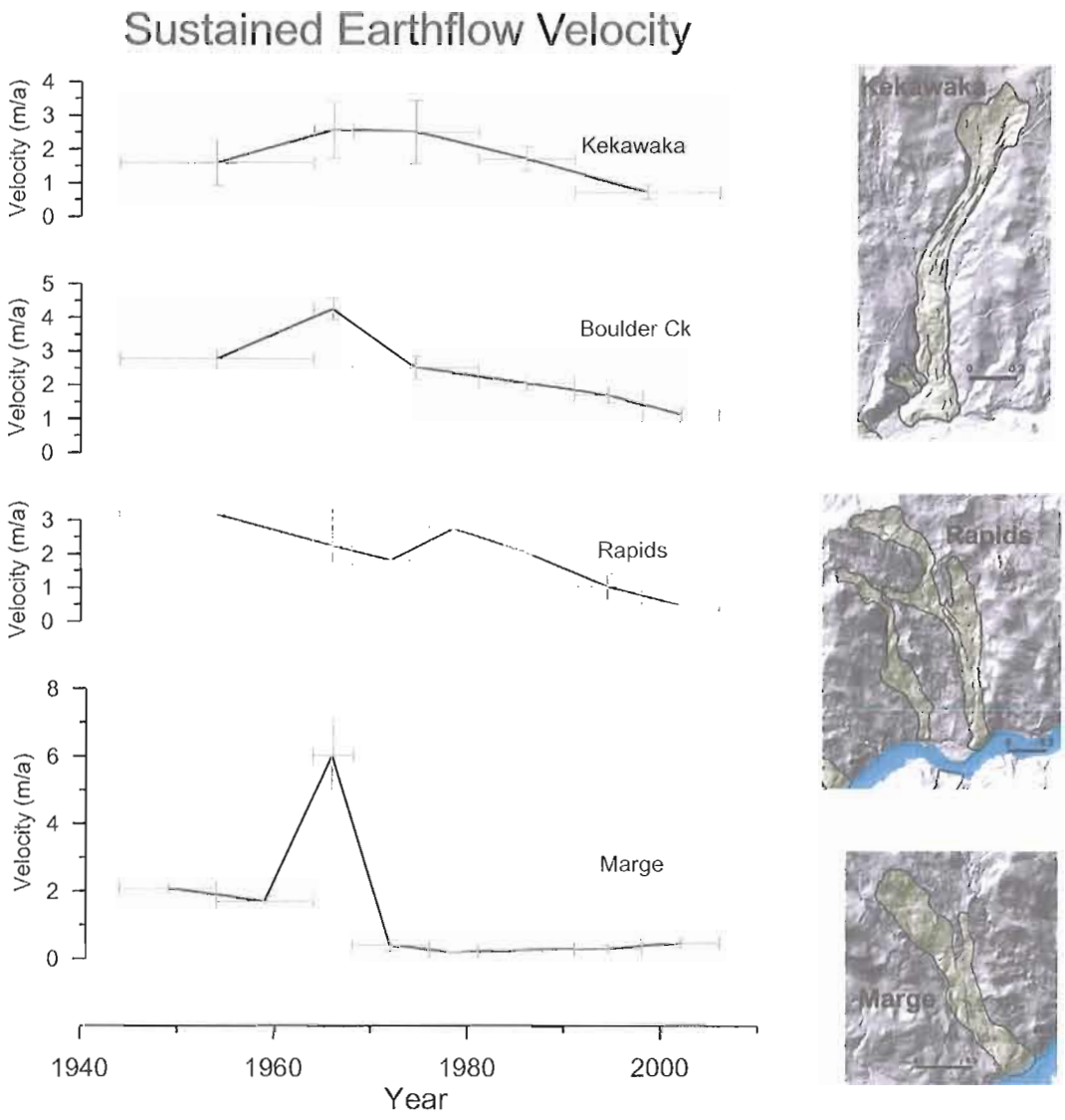

Figure 12. Temporal velocity and maps of earthflows with sustained velocities from 1944–1981, and subsequent decline. The Boulder Creek earthflow is shown in Figure 4. In Figures 12–14, horizontal error bars represent the interval between photos, and vertical error bars are the ± the standard deviation of transport zone tree velocities for each interval.

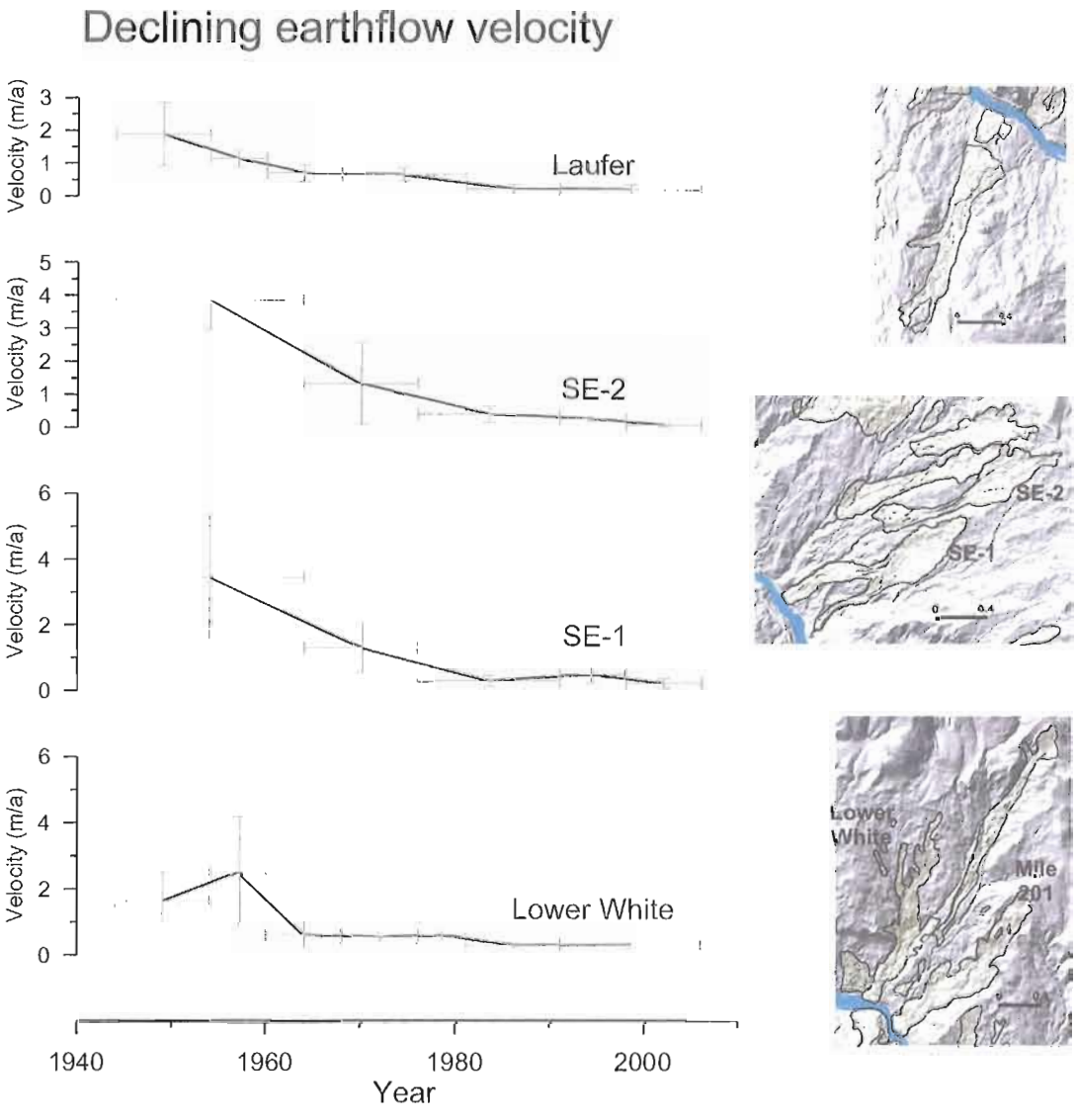

Figure 13. Temporal velocity and maps of earthflows with declining velocities since the 1940's–1950's. Lower White was heavily landscaped, and only trees on the upper region of the flow could be tracked.

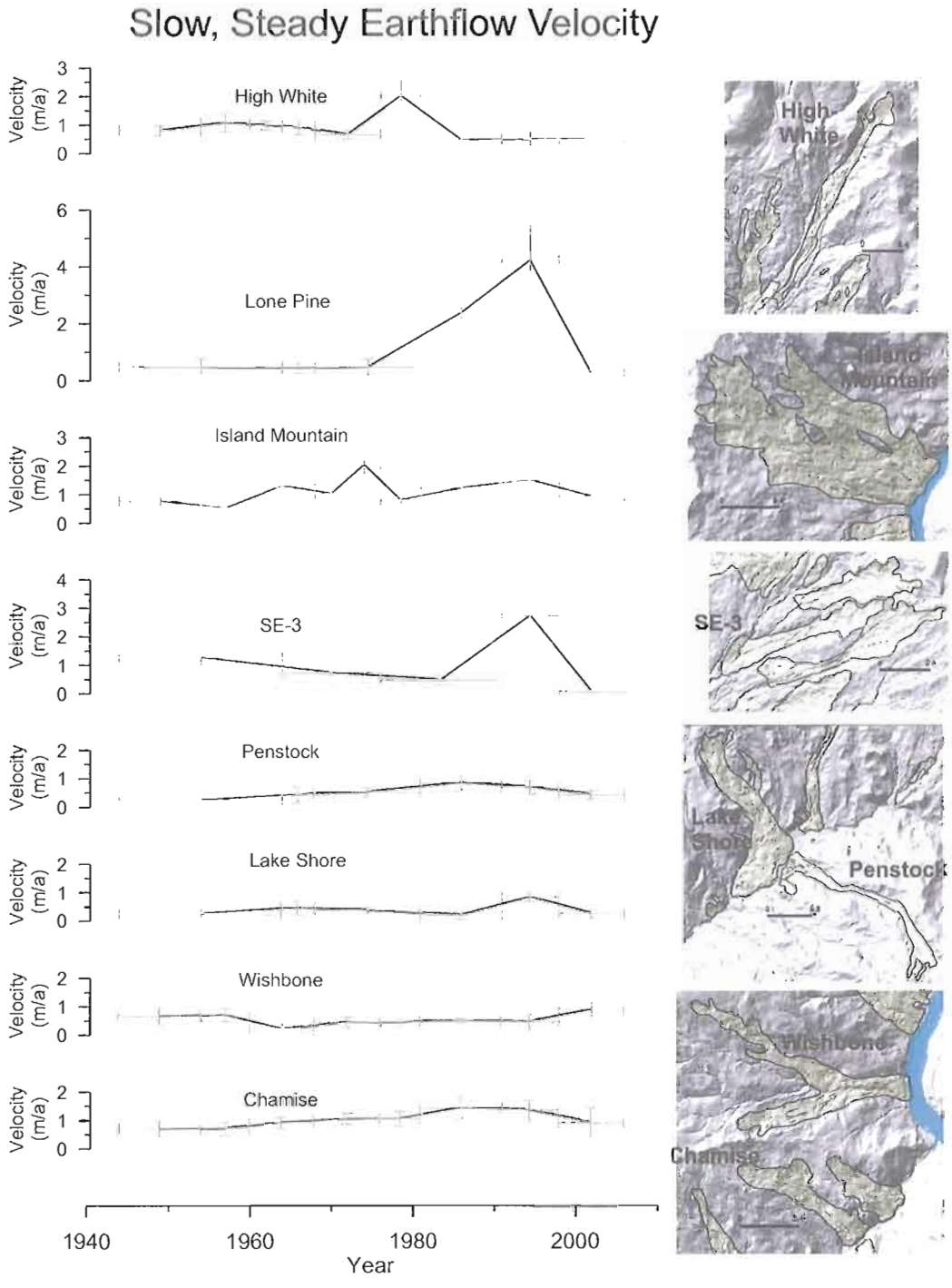

Figure 14. Temporal velocity and maps of earthflows with a slow, steady velocity, with occasional surges. The Lone Pine earthflow is shown in Figure 4.

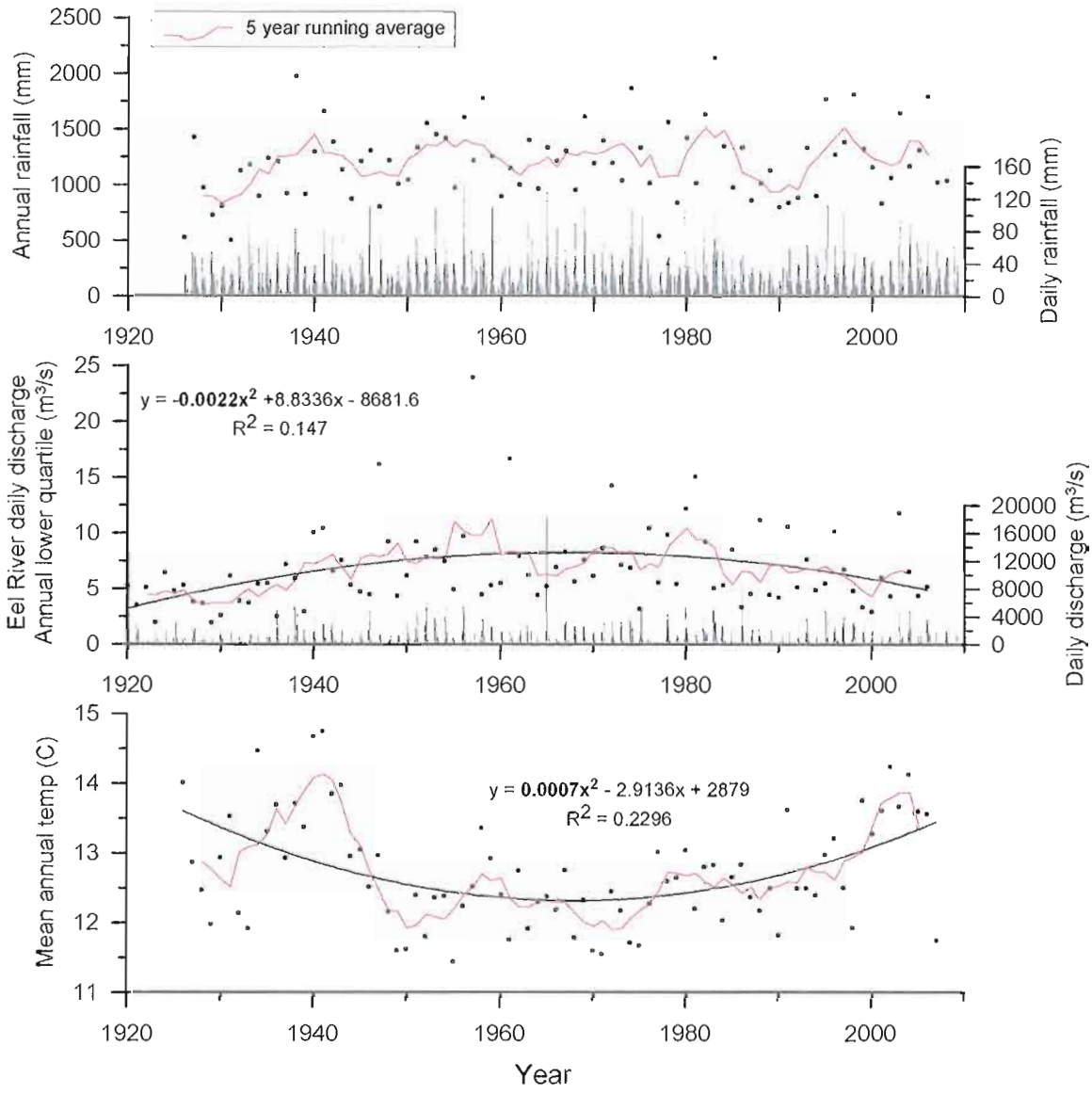

Figure 15. Plots of annual water year (Oct-Sept) climate statistics recorded on the Eel River at Scotia (Fig. 1).

a) Annual rainfall (dots) with a 5 year running average. Daily rainfall is plotted on the right axis.

b) 25th Percentile of annual Eel River daily discharge (dots) with 2nd order polynomial fit (equation shown) and 5 year running average. Daily discharge is plotted on the right axis – note the peak discharge in the 1964 flood.

c) Average annual mean daily temperature, with 2nd order polynomial fit (equation shown) and 5 year running average.

To test the significance of the second order polynomial fits for temperature and Q_{25}, we randomly re-sampled the annual data individually and fit a second order polynomial to the shuffled data. Repeating this 10,000 times for the two datasets, we noted that few of the fit coefficients for the 2nd order term approached the value of the actual data (Fig. 16), emphasizing the significance of 20th century trends.

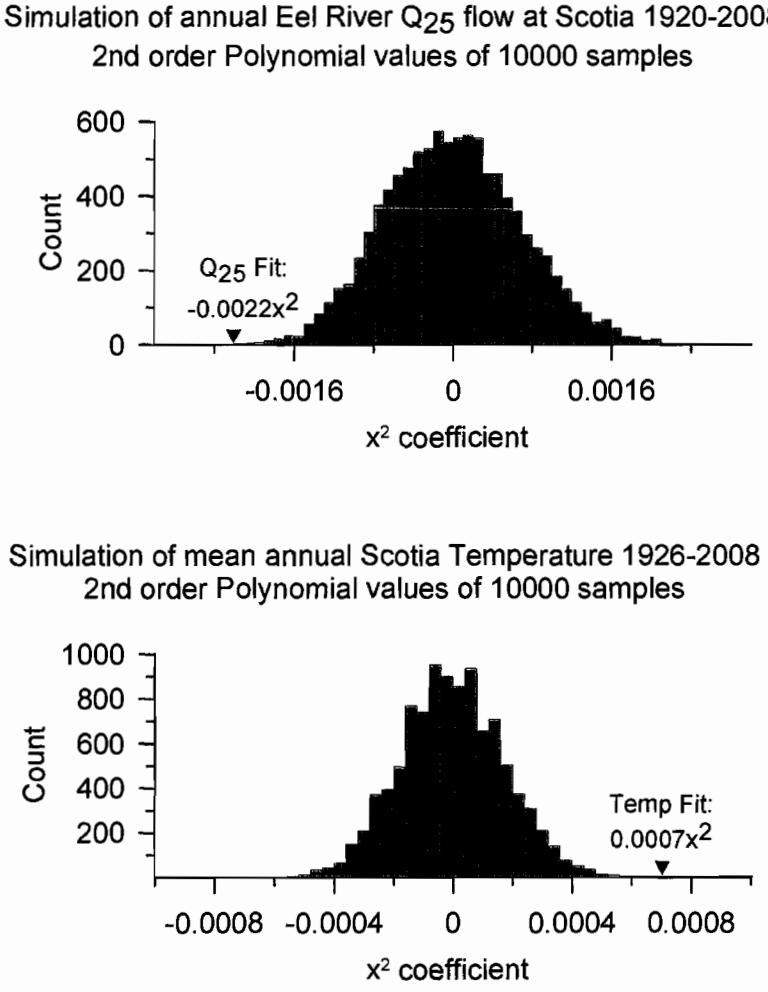

Figure 16. Histogram of x^2 coefficients of polynomial fits to random sampling of a) Q_{25} and b) temperature data, compared to the x^2 coefficients of the real data shown in Figure 15.

It can be difficult to discern subtle decadal-scale trends from annual data, so to better highlight multi-year trends, we calculated the cumulative deviation from the long term mean (Fig. 17). In these plots, a positive slope indicates a series of years with the variable consistently above the long term average of the period of record, and vice versa. Annual rainfall and Q_{25} discharge show similar trends, consistently above average from the 1940's through the 1970's. Temperature shows the opposite trend, temperature cooling abruptly in the late 1940's, and consistently cooler temperatures persist from 1947 to 1978. There is a decrease in the rate of change until 2000, and finally a series of years with above average temperatures.

One of the major influences on decadal climate in the Pacific northwest is the Pacific Decadal Oscillation or PDO (Mantua and Hare, 2002; Mantua et al., 1997). The PDO is driven by sea surface temperatures in the Pacific Ocean, and influences terrestrial climates which vary between cold-wet and warm-dry phases over a period of several decades. We include the raw PDO values and recognized phase shifts in Figure 17. The temperature, precipitation and Q_{25} trends are approximately bracketed by the changes in the PDO cycle.

4.4. Earthflow Sediment Flux

We estimate an annual sediment flux of $120 \pm 9 \times 10^3$ m^3/a for 62 earthflows which discharge directly into a creek or major gully. These earthflows have a combined area of 1.36×10^6 m^2 (6% of the study area), which equates to an erosion rate for the 62 earthflow features of 8.6 ± 0.6 mm/a. When distributed over the study area of 226 km^2, the active earthflows alone produce a sediment yield of 0.53 ± 0.04 mm/a. This is approximately 60% of the 0.9 mm/a sediment yield calculated for the Eel River (1950–2000) by Wheatcroft and Sommerfield (2005), suggesting that 6% of the terrain may supply the majority of the sediment over that period.

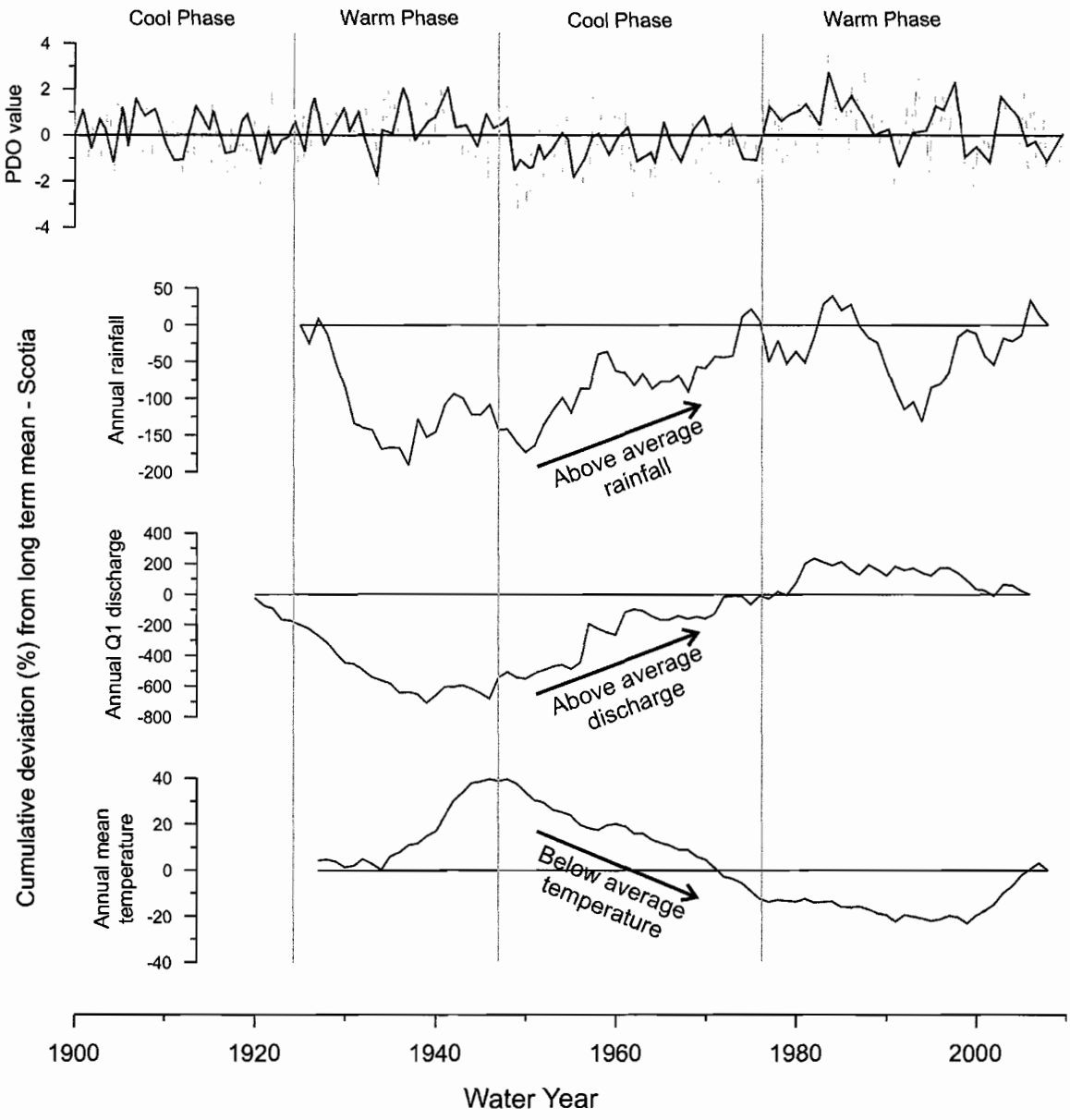

Figure 17. Monthly PDO values from 1900 with annual running mean. The recognized warm and cool phases are shown. Annual rainfall, 25th percentile Eel River discharge, and mean annual temperature cumulative deviation from the long term mean (%). A positive slope indicates sequential years with records above the long-term average.

In Figure 18, we plot the combined annual sediment delivery of 15 earthflows for which we have time series data. The Lone Pine earthflow (Figs. 4, 14) has a large effect on sediment flux from 1981 to 1998, and we present the annual sediment delivery including and excluding the Lone Pine contribution. Sediment delivery exceeds 70,000 m^3/a from 1944 to1964, increases to 95,000 m^3/a from 1964 to 1968, and (excluding Lone Pine) thereafter has steadily declined.

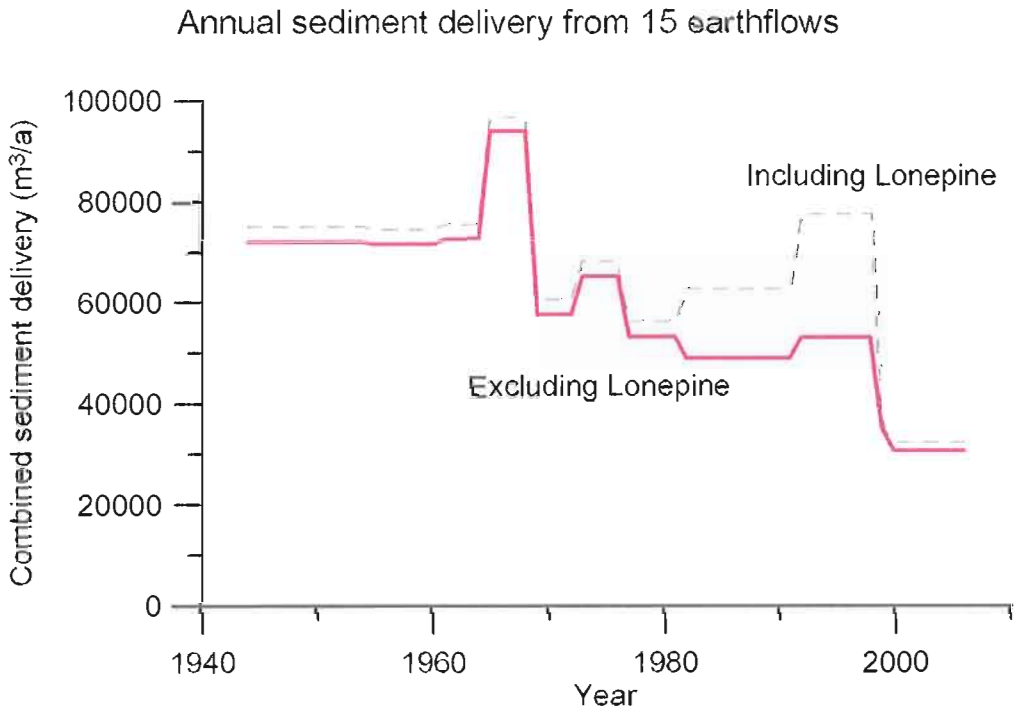

Figure 18. Combined annual sediment delivery for 15 large earthflows, showing the gradual decrease in sediment delivery, especially when the influence of the Lone Pine earthflow is removed.

5. DISCUSSION

5.1 Erosion and Sediment Delivery

Our results show that large, slow moving earthflows are the primary erosional process along the Eel River, preferentially occurring in weak mélange lithology. Mapping and sediment delivery calculations show that sediment flux attributable to active earthflow mass-movement along the Eel River canyon accounts for over half the estimated average sediment yield of the Eel River catchment during the second half of the 20th Century.

We attribute the sediment yield from the remainder of our study area to gullies, streambank erosion, soil creep, and isolated shallow landslides. In resistant lithology, the characteristic ridge and valley morphology indicates debris flows are a primary erosional process, although such terrain was sparse in our field area. There is potential for fluvial erosion of active earthflow terrain through localized gullying (Roering et al., 2009), although we did not account for this in our estimates of earthflow mass-movement. Estimates of fluvial erosion of the earthflow material at the Van Duzen and Redwook Ck sites respectively accounted for 50% and 10% of the total earthflow sediment flux (Kelsey, 1978; Nolan and Janda, 1995). We predict our main stem Eel Study site would lie somewhere between these values – the earthflows along the Eel River are not as active or as fluvially incised as those in the Van Duzen, but have higher rates of activity than those in Redwood Creek.

Given the extensive mélange lithology and the large number of active earthflows, our study area along the Eel River probably has a higher rate of erosion than the catchment average, so the proportion of erosion attributable to earthflow processes may not be as large as our results suggest. We consider Brown and Ritter's (1971) calculation of a sediment yield of 2 mm/a for the Eel River between Dos Rios and Fort Steward a maximum constraint. This data was recorded in the 2 years following the devastating 1964 flooding, and likely reflects increased sediment yield due to that event rather than a long term average rate.

The ratio of earthflow area to contribution to regional sediment flux for our Eel River study site (6% to 60%) approximates that found by Kelsey (1978) in the Van Duzen watershed (1% to 10%), suggesting that on average, active earthflows in Franciscan mélange erode an order of magnitude more rapidly than surrounding terrain. This highlights the highly erosive nature of earthflows, which lower their source area at 8.4 mm/a, 10–20 times greater than the estimated regional long term (10^3–10^4 year) erosion rate (Gendaszek et al., 2005). As argued by Mackey et al. (2009), this rapid rate of erosion indicates earthflows are eroding at unsustainably fast rates over periods beyond a few hundred years. The legacy of this cycle of rapid erosion followed by periods of dormancy (or permanent inactivity) is reflected in the ubiquity of inactive earthflow features in the landscape.

An important finding is that is that 1.3% of the study area, or 17% of the active earthflow terrain showed activity, but did not reach active channels. Earthflows can redistribute material on the hillslopes, and may not deliver sediment directly to channels.

5.2 LiDAR and Aerial Photos

Despite the challenges of mapping earthflows in fine grained mélange lithology, we found the combination of LiDAR, orthorectified aerial photographs, and localized field reconnaissance to be a robust technique to define active features. This approach allowed us to map both in detail and extensively, effectively bridging the gap between site specific studies and regional reconnaissance level photo-based mapping. Mapping the movement of individual trees provided a measure of objectivity in identifying earthflow activity that was not available from analyzing LiDAR maps or features in the field alone.

5.3 Spatial Characteristics

Our results show that the spatial pattern of earthflow activity across the Eel River Canyon has a systematic distribution. Although the size of the data set is modest (n =

122), earthflow sizes show 2 power law distributions. This is significant, as although catastrophic landslides have well documented power law behavior, such a relationship has not been demonstrated for large, slow moving earthflows.

The planform shapes of the earthflows vary greatly, and can diverge significantly from the classical hourglass planform. Many earthflows have complex and intricate margins, and multiple small tributary earthflows feeding into a centralized transport zone (Figs. 4, 7) Earthflows can bifurcate around topography, lower ridges, and capture the drainage area of adjacent terrain.

Typically active earthflows extend from the channel to the ridge (or a topographic break in slope), and we rarely observe them in a transient state, limited in extent to a portion of a hillslope. This suggests that once initiated, earthflows can rapidly expand longitudinally along a hillslope profile. Where earthflows do not span channel to ridge, they are limited to the upper sections of hillslope (Fig. 7), and constitute partial reactivation of older largely dormant earthflows features. This observation supports a top-down driver of longer term earthflow evolution – earthflows reactivate from the top, and activity propagates downslope, rather than a toe perturbation propagating upslope. This contrasts with many other types of bedrock landslide which are very sensitive to base level lowering (Densmore and Hovius, 2000). We argue the availability of readily mobilized source sediment that can be incorporated into an earthflow–probably governed by weathering rates, may be the ultimate control on the location and rate at which earthflows evolve. Figure 19 conceptually describes how an earthflow may evolve cyclically when they are governed by the availability of source material.

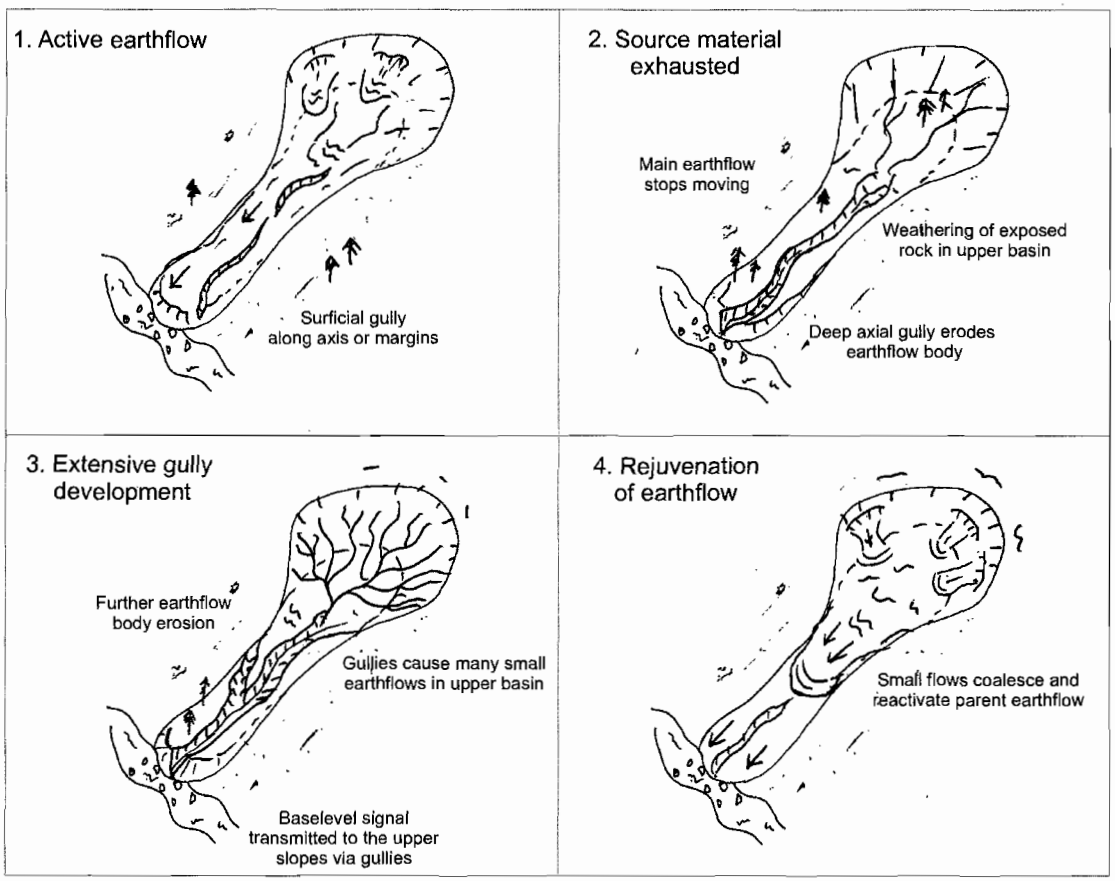

Figure 19. Conceptual earthflow evolution model.1) Active earthflow is being supplied with material from the upper amphitheatre. 2) Eventually the source material is exhausted, and gullies begin to erode the earthflow body. 3) Gullies propagate into the source area, mobilizing the weathered slopes. 4) Small flows coalesce and reactivate the earthflow transport zone.

Within the lithological variability across the study area, active earthflows preferentially occur in the sheared argillaceous mélange unit cml, and 10% of this lithology is subject to active slope instability (Fig. 2, Table 1). However, given the poor bedrock exposure in this region, much of the lithological mapping was undertaken with aerial photograph interpretation, and slope morphology is a key metric in distinguishing between different mélange units. For example, McLaughlin et al. (2000) note that unit cml exhibits characteristic earthflow morphology, and use the rounded, poorly incised,

lumpy and irregular topography as a diagnostic feature during lithological mapping. This introduces circularity when comparing earthflow activity across argillaceous mélange units. More robust is the observed process dichotomy between the argillaceous and more resistant sandstone outcrops, with earthflows absent in the latter (Table 1). Earthflows bifurcate around the harder mélange blocks, leaving them as localized topographic highs extruding out of the mélange. The exposed sandstone blocks either weather away in place by rockfall processes, or they can fail catastrophically if they are sufficiently undermined by the surrounding earthflow prone terrain. Larger, resistant sandstone outcrops at the kilometer scale have well incised drainages, and steeper slopes emphasizing the contrasting erosional regimes that operate within different lithologies in the same landscape, literally just meters apart.

The median earthflow slope is very similar to the study area terrain, although earthflows have a narrower slope distribution. The similarity in mean slopes between earthflows and all terrain supports the contention much of the landscape has been modulated by earthflow processes, even if they are not currently active. A slope of approximately 36% may be an approximate limiting threshold slope for earthflow activity, and represent the residual shear strength of the mélange (e.g., Carson and Petley, 1970; Hutchinson, 1967; Skempton, 1964).

The preferred southwesterly aspect matches the observation of Kelsey (1978), who suggested that slopes with a southerly aspect are dryer, and do not support conifer growth. Across our study area lithology appears to have a stronger influence on vegetation than aspect. Many north facing slopes have the open grassland susceptible to earthflow activity. The primary difference in northerly and southerly aspect is the sun exposure, so the preferred southerly aspect is likely attributable to differences in evaporation and soil moisture. McSaveney and Griffiths (1987) suggest drought may be a necessary precursor for earthflow activity. They argue that deep desiccation cracks penetrate into the earthflow mass during drought, allowing easy access for water when rainfall resumes, whereas when surface moisure levels increase the permeability of the earthflow decreases markedly. In the Eel River catchment, south facing slopes become

highly desiccated over the summer and cracks up to 30 mm wide extend to depths over 1 m. Northerly facing slopes do not dry to the same extent. This aspect governed asymmetry of drying over the summer months may explain some of the southwesterly aspect preference we observe in the active earthflows. The northerly facing slopes do have the morphology of dormant earthflows, so have been active in the past, potentially under different climatic conditions.

5.4 Temporal Characteristics

The time series of earthflow velocities across 16 features show three distinct temporal groupings. The variability in the temporal pattern of earthflow movements can be partially explained by decadal scale climate changes, although earthflow shape and position in the landscape appear to modulate this pattern. In particular, we consider sustained wet periods optimal for increased earthflow activity, especially on large earthflows (Bovis and Jones, 1992). Given the low permeability of earthflow soil (Iverson and Major, 1987), persistently wet conditions allow pore pressures to build up within the earthflow over several or more seasons. We can discount land use change, earthquakes, and base level change as having changed significantly between 1944 and 2006, but acknowledge we have not addressed the cumulative effect of higher frequency climatic changes such as El Nino.

The first group of earthflows showed rapid movement in the first interval from 1944 (Fig. 12), and then movement gradually slowed or stopped. This group of earthflows was unable to sustain movement as the wetter conditions persisted through to the late 1970's, and movement is negligible from 1981. Topographically, these slides are commonly high on the hillslopes and may have stabilized after initial movement due to mid-slope toe buttressing.

The second group of earthflows exhibit sustained movement until the late 1970's, and gradually slowed from approximately 1981 to present. This group of earthflows have long, narrow transport zones which we argue is the most sensitive recorder of decadal

climatic changes (Bovis and Jones, 1992), because they are largely isolated from source or toe effects. The Boulder Creek and Kekawaka earthflows show an increase in velocity over the 1960's, and mimic the trends in temperature and Q_{25} flow, potentially showing a high sensitivity to the variation in climate. This period also coincides with the December 1964 storm, and we cannot confidently discount the role of extreme rainfall events in increasing earthflow activity. For example, although we distinguished declining and sustained temporal behavior (Figs 12–13), if we remove the data point from 1964 to 1968, many of the Figure 12 earthflows would also appear to exhibit declining velocity.

The remaining earthflows are generally slow (1–2 m/a), although some have isolated surges. Six of these eight earthflows are tightly coupled with major creeks and channels, and sustained erosion of the toe may dominate earthflow response over the climatic changes. A clear example of this is the Penstock and Lake Shore earthflows, whose toes oppose each other across Kekawaka Creek and act as a choke point on the channel. Other examples, such as the Chamise, Wishbone, Island Mountain, and Lone Pine landslides feed directly into major channels, which remove the potential buttressing and topographic stability a compressional toe can provide (e.g. Boulder Creek – Figure 4, Laufer Earthflow – Figure 12). We also note that this third group of earthflows commonly feature unconventional shapes, with either small aspect ratios (Lake Edge, Island Mountain), or are extremely skinny (High White, Penstock).

The climate changes significantly in the 1940's (Figs. 15, 17). From the mid 1940's, rainfall and Q_{25} discharge are consistently above average, whereas temperatures are below the average of the period of record (Fig. 15). This time coincides with the PDO cool phase (1946–1977). As our earliest aerial photos date from 1944, we have no record of earthflow activity prior to the 1940's, which impedes our interpretations of long term behavior. In the decades preceding 1944, rainfall and Q_{25} river discharge are generally below the long term average, while median annual daily temperature is above average. The period from 1924–1947 is recognized as a warm phase of the PDO (Fig. 17), and if there was less earthflow activity in from 1920 to 1940, it would support our contention that decadal scale climate changes influence earthflow activity. In this dryer, warmer

climate, we would anticipate less soil moisture, lower groundwater levels, and therefore we would speculate less earthflow activity, although we stress the amount of pre-1944 earthflow activity remains unconstrained. Although unsubstantiated, it is appealing to conceive earthflow activity increasing rapidly in response to the climate changes in the 1940's. As such, our study period would document the rapid earthflow adjustment to the onset of cooler, wetter conditions in 1947.

Some of these earthflows show an interval of rapid movement, such as SE-1 in the mid 1990's. We have little explanation for these events, other than possible natural variability or possibly triggering from individual storms. Isolated earthflow surges have been documented (Hutchinson and Bhandari, 1971). One historical example on the Eel River is the 201 Slide crossing the railway (Fig. 13), reported by Malhase (1938). In February 1938, this earthflow advanced 13 feet over 24 hours in response to heavy rainfall.

Generalizing all the temporal earthflow records, with few exceptions, there has been a decrease in activity since the late 1970's (e.g., Fig. 18). This general reduction in earthflow movement coincides with more variable climate than persisted from 1947–1978. Annual rainfall was below average in the period 1983–1992, but has increased subsequently (Fig. 17). In a departure from the rest of the record, base flow does not follow the increase in rainfall from 1992, potentially attributable to the increased temperature (and therefore evaporation) over the past decade. From 1980, we do not observe the sustained wetter, cooler conditions characteristic of the 1960's, which are conducive to earthflow activity.

The influence of decadal scale climate changes has been recognized in other studies. For example, Bovis and Jones (1992) show increased earthflow activity over the mid 20th Century in British Columbia. Their rainfall cumulative deviation plots are very similar to those from Scotia, highlighting the widespread effect of PDO changes on earthflows across the Pacific Northwest. Geertsema et al. (2006) find very similar temporal patterns of temperature change in British Columbia, although here the change in

climate is having the opposite effect, with increasing temperature since the late 1970's degrading permafrost and increasing landslide activity.

Several earthflows attain maximum velocities in the photo interval 1964–1968 (Fig. 13). This period coincides with both the middle of the PDO cool phase, and the 1964 storm, so it is difficult to distinguish the influence of the extreme rainfall events from ambient climate conditions. On the photographs, we observe little qualitative evidence of accelerated earthflow activity or disturbance in response to the December 1964 storm. For example, there is little evidence of substantial toe erosion or disruption to the gully network on the earthflows, even though the 1964 event had a major effect on rivers and channels (Kelsey, 1980; Sloan et al., 2001). This observation also holds for major storms in 1982 and 1997. Individual rainfall events deliver water too rapidly for infiltration into the soil, although they may affect gullies on the earthflow surface and accelerate erosion of the toe.

The PDO cycle is predicted to switch back to a cold phase from 2008, and measurements of Pacific sea surface temperatures indicate this change is underway (e.g., Buis, 2008). If this shift is sustained and the northern California climate returns to that of the 1940's, we would predict a possible short term reactivation of earthflows high on the hillslopes, and gradual increase in activity of the larger earthflows such a Boulder Creek. Increased earthflow activity over the coming decades will have management implications for land owners, transport corridors, and aquatic habitat, and management strategies should be adjusted accordingly.

6. CONCLUSION

A landscape scale theory explaining earthflow movement, sediment flux and the influence of earthflows on landscape morphology remains a future research objective, but this study illustrates how earthflows control the evolution of this rapidly eroding landscape in the northern California Coast Ranges. We use LiDAR and aerial photos to objectively document earthflow activity and sediment flux at an unprecedented spatial

and temporal scale, and with a higher level of accuracy than available with traditional methods. We find earthflows have a characteristic position in the landscape, and some earthflows exhibit systematic temporal behavior in response to climatic changes

In fine-grained clay-rich lithology, earthflows can have a major impact on sediment yield slope morphology. We estimate active earthflows contribute more than half of the suspended sediment of the Eel River, despite accounting for only 6% of the terrain area. Given the erosion rate of an active earthflow can exceed the regional rate by an order of magnitude, we envisage earthflow activity as intermittent, separated by long periods of dormancy. Most of the argillaceous terrain in our study site shows topographic evidence of earthflows, suggesting that locations of activity can migrate through the landscape. We observed 7.3% of the Eel River Canyon to show movement between 1944 and 2006, and most of this area is represented by large earthflow complexes spanning channel to ridge, with a southwesterly aspect. In contrast to other styles of slope failures, earthflows reactivate from the top and this perturbation propagates downslope, and we suggest long term availability of readily mobilized source sediment is the ultimate control on earthflow activity and evolution.

The temporal pattern of earthflow movement shows variability which approximately coincides with changes in decadal scale climate. This is particularly evident in earthflows with long, well defined transport zones, whereas earthflows with a less conventional planform behave more stochastically. The lack of information about pre-1944 earthflow activity tempers some of our interpretations, as we don't know the historical context of the high rates of movement we document from 1944 to the 1970's They could either represent an increase attributable to the cooler, wetter climate, or alternatively we may have witnessed the earthflows in a longer term monotonic decline of a duration which precedes the photographic record. We argue periods with sustained rainfall and cool temperatures the most amenable to earthflow activity, and if the

predicted shift to a new PDO cool phase transpires, earthflow activity in northern California could again increase in the coming decades.

APPENDICES

APPENDIX A

14-C DATING OF SKUNK CREEK LANDSLIDE COMPLEX, SOUTH FORK EEL RIVER, CALIFORNIA

1. Radiocarbon Dating Landslide Movement

In one accessible landslide in the Skunk Creek catchment (Figure 1), we attempted to constrain the timing of landslide movement. We chose the Skunk Creek landslide because it has limited disturbance by road construction and historical logging activity, and appeared to exhibit multiple phases of movement, and the morphology of the landslide appeared similar to others in the study area. Dating prehistoric landslides is challenging [*Lang et al.*, 1999], and various techniques including tephrochronology [*Hermanns et al.*, 2000], cosmogenic exposure age [*Ballantyne et al.*, 1998; *Bigot-Cormier et al.*, 2005], and radiocarbon dating [*Pellegrini et al.*, 2004] have been utilized. We focused on dating charcoal in the base of headscarp depressions and graben features within the landslide mass. Carbonaceous material deposited in the newly opened depression shortly after slide movement is preserved under the infilling colluvium [*Lang et al.*, 1999], but due to inheritance issues with detrital carbon (time taken from tree growth to eventual burial), the age should be considered a maximum constraint [*McGill et al.*, 2002] and the younger of multiple samples is preferred. We identified a range of suitable target depressions on the LiDAR derived DEM, and using a combination of hand auguring and digging, excavated to the base of the infilling colluvium at four locations on the slide. Two samples of detrital carbon from each of the four sites on the landslide were collected and analyzed for ^{14}C by accelerator mass spectrometry at Lawrence Livermore

National Laboratory, and converted to calendar years using the conversion of *Fairbanks et al* [2005].

2. Skunk Creek Landslide Age Constraints

The oldest ages for Skunk Creek landslide activity are late-Pleistocene (~13.7 ka), and come from an infilled graben below the primary headscarp (Table 1; Figure 1). The ^{14}C ages from Skunk4B are from a deep headscarp depression near the watershed boundary, just above the headscarp of the younger internal slide described below. Although stratigraphically consistent, there is a large age difference between the two Skunk4B samples. Skunk 3B and Skunk 5B come from the margins of a secondary failure within the parent landslide mass, and show a distinct cluster at 2.5–2.8 ka.

Sample	Depth (m)	Radiocarbon age		Calendar Age*	
		Mean	std dev	mean	std dev
Skunk2A1-AAA	2.63 (auger)	12600	60	14827	111
Skunk2B-AAA	2.54 (auger)	11840	100	13745	133
Skunk3B1-AAA	1.5 (soil pit)	2765	45	2858	52
Skunk3B2-AAA	1.5 (soil pit)	2545	35	2691	66
Skunk4B 185	1.85 (auger)	3290	15	3506	31
Skunk4B 195	1.95 (auger)	8790	20	9796	60
Skunk5B 150	1.50 (auger)	2460	15	2563	89
Skunk5B 165	1.65 (auger)	2780	15	2866	19

Table 1. Radiocarbon dates on detrital charcoal from the Skunk Creek Landslide.
*Based on conversion of Fairbanks et al [2005] available at:
http://www.radiocarbon.LDEO.columbia.edu/

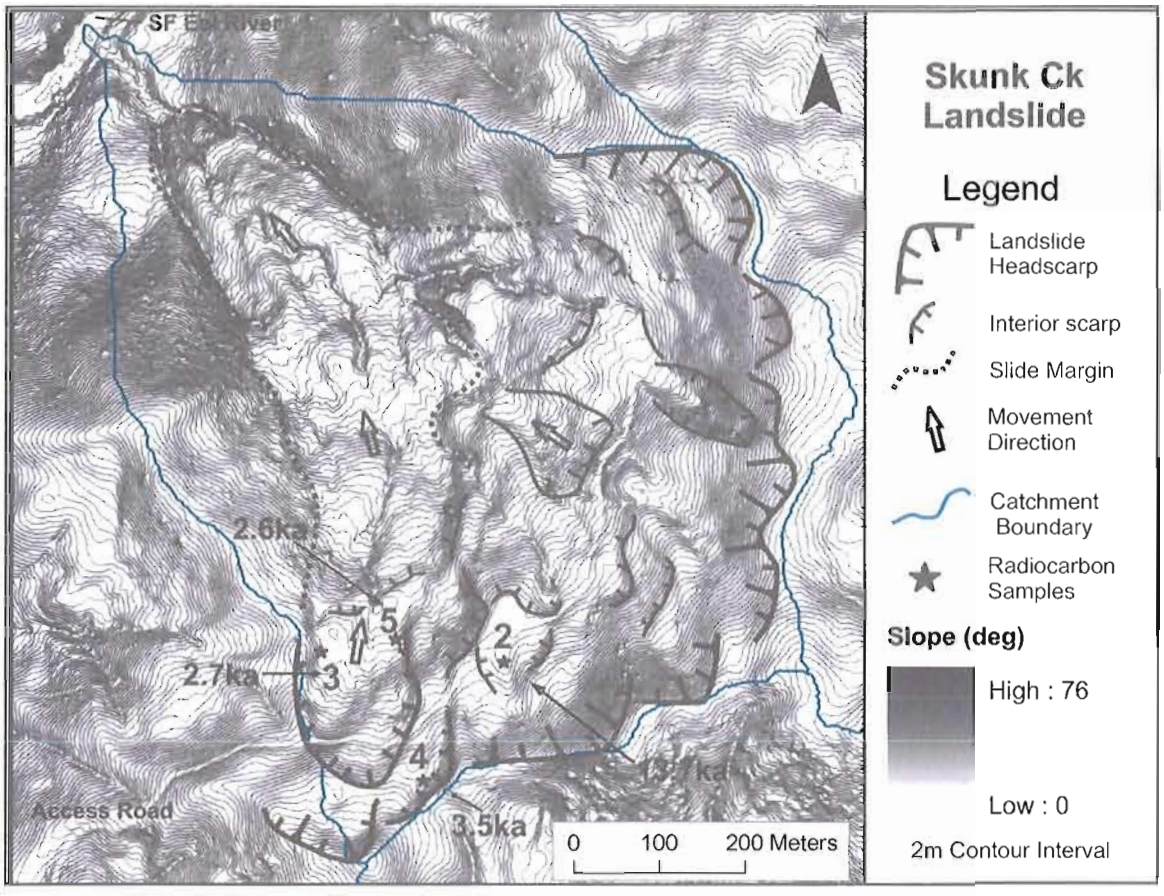

Figure 1. Slope and contour map of the Skunk Creek landslide complex showing the headscarp and major morphological features. Numbers 2-5 denote sample locations for charcoal, described in Table 1. Two samples were taken at each location, with the younger age shown on the map. The ^{14}C ages suggest the landslide failed ~13.5 ka, whereas the morphologically distinct internal feature reactivated approximated 2.6 ka.

3. Climatic Interpretation

The ^{14}C ages from the Skunk Creek landslide support our initial hypothesis of multiple phases of movement within the Skunk Creek landslide basin. The sample from the extensional graben near the primary headscarp (Skunk2) suggests a late Pleistocene age for the landslide. Deep seated landsliding in the Northern Californian Coast Ranges has often been attributed to the climatic conditions of the late Pleistocene, but has not to our knowledge yet been confirmed by carbon dating. The significance of the Skunk4 ages is difficult to interpret, as there is a difference of over 6000 years between samples taken only 10cm apart. The Skunk 4B site has an age of 9.8 ka, which corresponds with the earliest Holocene, and materially later than the samples from the headscarp feature at Skunk2B and 2A, implying different parts of the landslide may have been active at different times. Given inheritance issues, however, we favor the younger age of 3.5 ka. We are more confident in the ages for Skunk 3B and 5B, where four ages from 2 different locations on the inset landslide feature cluster tightly around 2.5–2.9 ka. This landslide has sharper features than the larger parent slide, which would be expected given the younger age, and indicates this feature was mobilized within the mass of the older landslide about 2.6 ka. The multiple phases of movement in the Skunk slide illustrate how subsidiary failures can occur within a previously failed landslide mass, potentially many thousands of years later. The older section of the Skunk landslide is morphologically similar to neighboring slides, and suggests many of the mapped landslides may have failed in the Late-Pleistocene.

Climatically, the latest Pleistocene conditions in the northern Californian Coast Ranges are thought to have been wetter than those at the last glacial maximum, and wetter and colder than modern conditions [*Adam and West*, 1983; *Daniels et al.*, 2005; *Rypins et al.*, 1989]. From an offshore pollen core near the mouth of the Eel River, Barron et al [2003] interpret the latest Pleistocene (<16 ka) to exhibit dry but changeable conditions, with increasing precipitation approaching the Holocene transition. Spikes in alder pollen indicate ground disturbance, possibly due to widespread landsliding. The oldest dates from the Skunk Ck landslide therefore correspond with a changing climate

with increasing precipitation, conditions that would presumably promote landsliding. The early Holocene climate is reportedly dryer and warmer [*Adam and West*, 1983], before a regional shift to slightly cooler and wetter conditions in the late Holocene [*Daniels et al.*, 2005], with the establishment of the modern redwood forest and a maritime climate from about 3.5 ka [*Barron et al.*, 2003]. The radiocarbon dates from 3.5 ka through 2.6 ka coincide with this transition from the dry mid-Holocene to the establishment of redwood forest and wetter modern climatic conditions. Given the lack of deep seating landsliding we observe today, this may reflect a critical period where increased precipitation generated landsliding, before it was mitigated by the expansion of the dense redwood forest over the past 3 ka. Both the late Pleistocene (13.5 ka) and Late Holocene (3.5–2.5 ka timeframes at which we constrain landslide movement relate to periods of climatic change to a wetter climate, and such transitional periods may be instrumental in generating large slope failures.

References

Adam, D.P., and G.J. West, Temperature and Precipitation Estimates through the Last Glacial Cycle from Clear Lake, California, Pollen Data, *Science*, *219* (4581), 168-170, 1983.

Ballantyne, C.K., J.O. Stone, and L.K. Fifield, Cosmogenic Cl-36 dating of postglacial landsliding at The Storr, Isle of Skye, Scotland, *Holocene*, *8* (3), 347-351, 1998.

Barron, J.A., L. Heusser, T. Herbert, and M. Lyle, High-resolution climatic evolution of coastal northern California during the past 16,000 years, *Paleoceanography*, *18* (1), 2003.

Bigot-Cormier, F., R. Braucher, D. Bourles, Y. Guglielmi, M. Dubar, and J.F. Stephan, Chronological constraints on processes leading to large active landslides, *Earth and Planetary Science Letters*, *235* (1-2), 141-150, 2005.

Daniels, M.L., R.S. Anderson, and C. Whitlock, Vegetation and fire history since the Late Pleistocene from the Trinity Mountains, northwestern California, USA, *Holocene*, *15* (7), 1062-1071, 2005.

Fairbanks, R.G., R.A. Mortlock, T.C. Chiu, L. Cao, A. Kaplan, T.P. Guilderson, T.W. Fairbanks, A.L. Bloom, P.M. Grootes, and M.J. Nadeau, Radiocarbon calibration curve spanning 0 to 50,000 years BP based on paired Th-230/U-234/U-238 and C-14 dates on pristine corals, *Quaternary Science Reviews*, *24* (16-17), 1781-1796, 2005.

Hermanns, R.L., M.H. Trauth, S. Niedermann, M. McWilliams, and M.R. Strecker, Tephrochronologic constraints on temporal distribution of large landslides in northwest Argentina, *Journal of Geology*, *108* (1), 35-52, 2000.

Lang, A., J. Moya, J. Corominas, L. Schrott, and R. Dikau, Classic and new dating methods for assessing the temporal occurrence of mass movements, *Geomorphology*, *30* (1-2), 33-52, 1999.

McGill, S., S. Dergham, K. Barton, T. Berney-Ficklin, D. Grant, C. Harding, K. Hobart, R. Minnich, M. Rodriguez, E. Runnerstrom, J. Russell, K. Schmoker, M. Stumfall, J. Townsend, and J. Williams, Paleoseismology of the San Andreas fault at Plunge Creek, near San Bernardino, southern California, *Bulletin of the Seismological Society of America*, *92* (7), 2803-2840, 2002.

Pellegrini, G.B., N. Surian, and C. Urbinati, Dating and explanation of late glacial - Holocene landslides: a case study from the southern Alps, Italy, *Zeitschrift Fur Geomorphologie*, *48* (2), 245-258, 2004.

Rypins, S., S.L. Reneau, R. Byrne, and D.R. Montgomery, Palynological and Geomorphic Evidence for Environmental-Change During the Pleistocene Holocene Transition at Point-Reyes Peninsula, Central Coastal California, *Quaternary Research*, *32* (1), 72-87, 1989.

APPENDIX B

SUPPLEMENTARY MATERIAL FOR CHAPTER III

Date	Photo number	Source	CFL (mm)	Fiducials	Image Format	Resolution (dpi)
8-19-1944	DDD 54-46	DoD/USFS	210 (est)	Measured	Scanned print	800
6-13-1964	VBAG 2-81	USGS	151.67	Measured	Scanned print	1800
7-22-1968	VBZX 1-163	USGS	152.45	Measured	Scanned print	1800
7-08-1981	VEZF 2-4	USGS	152.347	Supplied	Scanned print	1800
7-26-1991	91CA 10-72	WAC	152.903	Supplied	Scanned Diapositive	1200
9-24-2006 - 9-26-2006	Unfiltered Lidar	NCALM	NA	NA	1m DEM	1m

Table 1
Orthorectification requires information including camera lens information (focal length, fiducal distances), a digital elevation model (DEM) of the terrain, and ground control points (GCP's) to correlate image position to the ground. Where possible, we used Camera Focal Length (CFL) information from camera calibration reports, although the 1944 photo parameters had to be estimated from a database (Slama 1980). In the earlier photos (1944-1968) we measured the distance between fiducials manually, and we assumed a perfect principal point of focus (x,y = 0,0). In the 1981 and 1991 photos, fiducial measurements were supplied in the calibration reports. We selected approximately 30 GCP's for each image (e.g. buildings, rock outcrops, trees on stable ridges or terraces) using unfiltered LiDAR as the reference image, and the bare earth LiDAR 1 m DEM to construct the camera model in Erdas Imagine 9.1 software. (Slama, C.C., 1980, Manual of Photogrammetry: Falls Church, VA, American Society of Photogrammetry, p. 1056.)

Table 2. Meteoric ^{10}Be data. For each depth interval, soil samples were oven dried, crushed, and pulverized into a fine powder. From the pulverized mix, a 0.5 g sample was processed following Stone (1998) (See also: http://depts.washington.edu/cosmolab/chem/fusionmethod.pdf). Blank samples were processed with every 4-8 soil samples to constrain the analytical error.

	Sample name	Depth (cm)	Longitude (UTM)	Latitude (UTM)	Elevation (m)	10-Be Conc (Atoms/cm3)	Error (Atoms/cm3)	Inventory (atoms/cm2)	Error (atoms/cm2)	10-Be age	Age Error
Pit 1	KW1015	0-15	458470	4441020	606	2.9E+07	1.8E+06	1.0E+09	3.9E+07	620	130
	KW11530	15-30				2.5E+07	1.5E+06				
	KW13045	30-45				6.6E+05	2.1E+05				
	KW14560	45-60				7.8E+05	3.2E+05				
	KW16075	60-75				2.2E+05	2.0E+05				
	KW17590	75-90				1.4E+07	1.2E+06				
Pit 2	KW2015	0-15	458400	4440759	536	2.1E+07	1.2E+06	4.2E+08	1.9E+07	250	50
	KW21530	15-30				4.0E+06	4.0E+05				
	KW23045	30-45				6.6E+05	2.1E+05				
	KW24560	45-60				1.4E+06	2.3E+05				
	KW26090	60-90				4.0E+05	3.7E+05				
	KW290120	90-120				-6.4E+03	-2.6E+05				
	KW2120145	120-145				-1.6E+04	-1.6E+05				
	KW2145170	145-170				1.7E+05	3.8E+05				
Pit 3	KW3015	0-15	458211	4440484	473	2.5E+07	1.9E+06	6.8E+08	3.3E+07	400	80
	KW31530	15-30				1.5E+07	1.2E+06				
	KW33045	30-45				1.5E+06	4.8E+05				
	KW34560	45-60				8.9E+05	3.3E+05				
	KW36090	60-90				5.9E+05	3.7E+05				
	KW390120	90-120				-9.1E+04	-1.4E+05				
	KW3120160	120-160				2.2E+05	1.3E+05				
	KW3160200	160-200				3.5E+05	2.9E+05				

	Sample name	Depth (cm)	Longitude (UTM)	Latitude (UTM)	Elevation (m)	10-Be Conc (Atoms/cm3)	Error (Atoms/cm3)	Inventory (atoms/cm2)	Error (atoms/cm2)	10-Be age	Age Error
Pit 4	KW50010	0-10	458164	4440302	439	7.0E+07	4.1E+06	2.9E+09	2.5E+08	1700	400
	KW51020	10-20				4.9E+07	2.9E+06				
	KW52030	20-30				3.1E+07	1.3E+07				
	KW53040	30-40				4.9E+07	2.0E+07				
	KW54050	40-50				3.8E+07	2.2E+06				
	KW55060	50-60				2.1E+07	1.4E+06				
	KW56080	60-80				1.8E+07	1.4E+06				
Crown	KW40010	0-10	458548	4441112	638	2.8E+08	1.7E+07	2.0E+10	4.3E+08	12000	2500
	KW41020	10-20				3.2E+08	1.9E+07				
	KW42030	20-30				3.2E+08	1.8E+07				
	KW43040	30-40				3.3E+08	1.7E+07				
	KW44050	40-50				2.9E+08	1.6E+07				
	KW45060	50-60				2.7E+08	1.6E+07				
	KW46070	60-70				1.8E+08	9.8E+06				

Figure 1. Earthflow Geomorphology - The earthflow has a steep arcuate headscarp defining an amphitheatre-like collection or source zone, which enlarges by retrogressive failure of the headscarp and provides the earthflow material. Failing blocks back rotate in a listric manner and fall into the hummocky upper amphitheatre or source zone, where they disintegrate, and themselves become buried by disintegration and raveling from subsequent failure blocks above. The upper section of the source zone gradually transitions downslope into a smoother, narrow transportation zone and (although moving) the surface becomes more stable, allowing shrubs to grow. The transportation zone transitions into a compressive broad section with thrusting and folding. Down slope of the road, the flow steepens, and surficial slumps disrupt the earthflow surface. At the toe the earthflow encounters Kekawaka Creek. A steep, interlocking boulder cascade (removed by LiDAR processing) inhibits mass flow movement into the creek, but erosion of the toe occurs by slumping from the toe face and erosion of fines during high flows. Due to the boulder constriction, the earthflow toe mass is subject to compression and over-thrusting, and is escaping laterally onto an alluviated reach downstream. The background image is LiDAR derived slope (1m resolution).

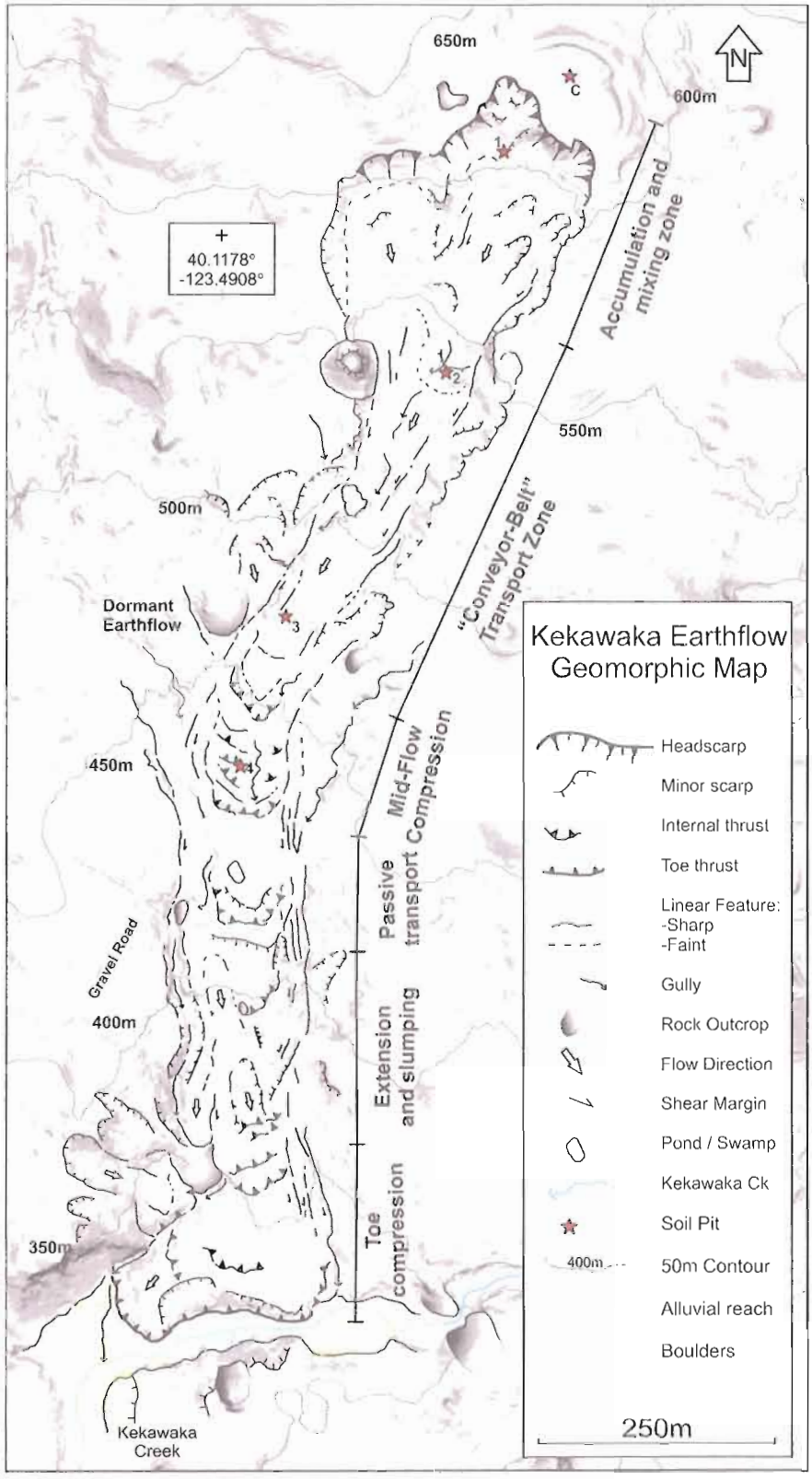
650m
600m
550m
500m
450m
400m
350m
N
C
1
2
3
4
+
40.1178°
-123.4908°
Accumulation and mixing zone
"Conveyor-Belt" Transport Zone
Mid-Flow Compression
Passive transport
Extension and slumping
Toe compression
Dormant Earthflow
Gravel Road
Kekawaka Creek
Kekawaka Earthflow Geomorphic Map
Headscarp
Minor scarp
Internal thrust
Toe thrust
Linear Feature:
-Sharp
-Faint
Gully
Rock Outcrop
Flow Direction
Shear Margin
Pond / Swamp
Kekawaka Ck
Soil Pit
400m
50m Contour
Alluvial reach
Boulders
250m

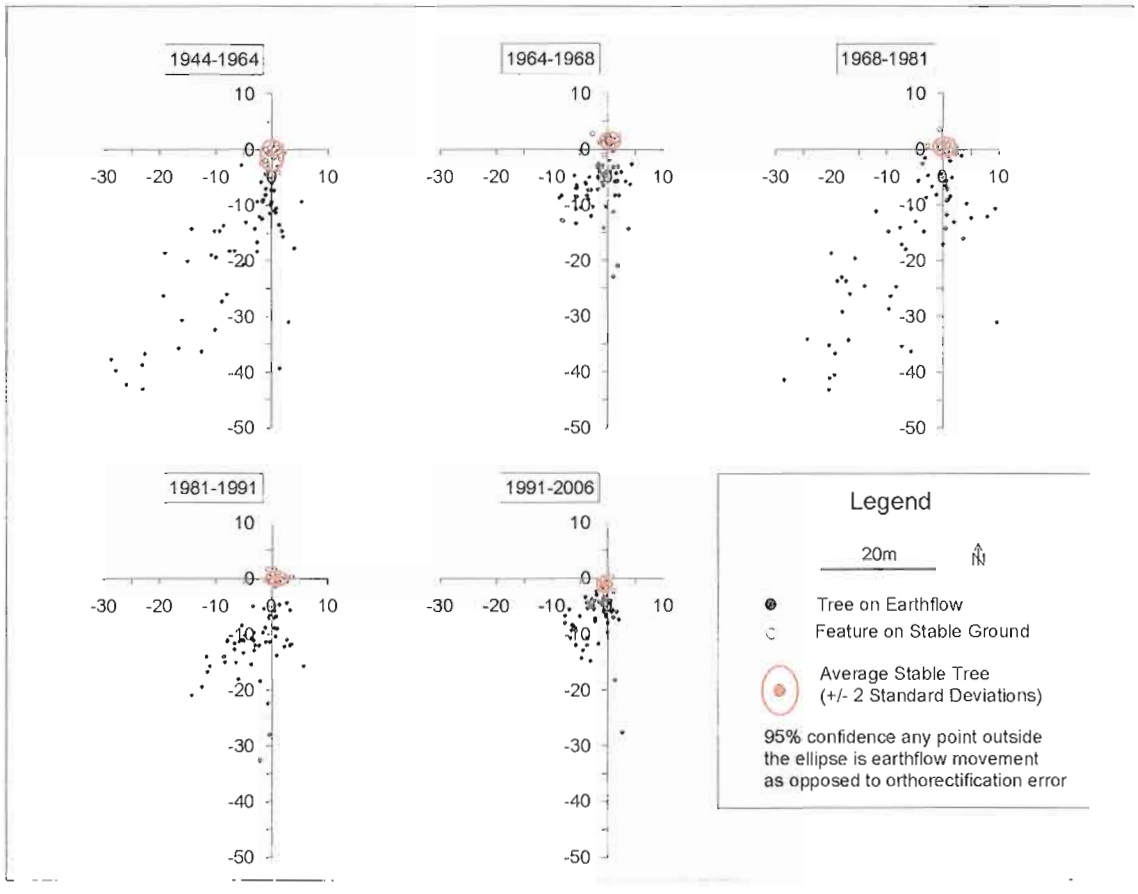

Figure 2. Comparison of stable features vs. trees on the earthflow for each photographic interval. We are 95% confident features plotting outside the circle (2 standard deviations) reflect earthflow movement, as opposed to orthorectification errors or vegetation change.

APPENDIX C

EVIDENCE FOR A LANDSLIDE DAMMED PALEO-LAKE ALONG THE MAIN STEM EEL RIVER

During the course of researching earthflows along the Eel River, I have discovered several lines of evidence suggesting the Eel River was one impounded behind a large landslide dam.

Many terrace features cluster within a consistent elevation (~240-242m asl), as shown on Figures 1 and 2. I have visited many of these features in the field, and they are typically gently undulating surfaces with bioturbated fine grained sediments. Small creeks and gullies at this elevation commonly exhibit a subtle wedge of fine-grained sediments, consistent with delta-like deposition.

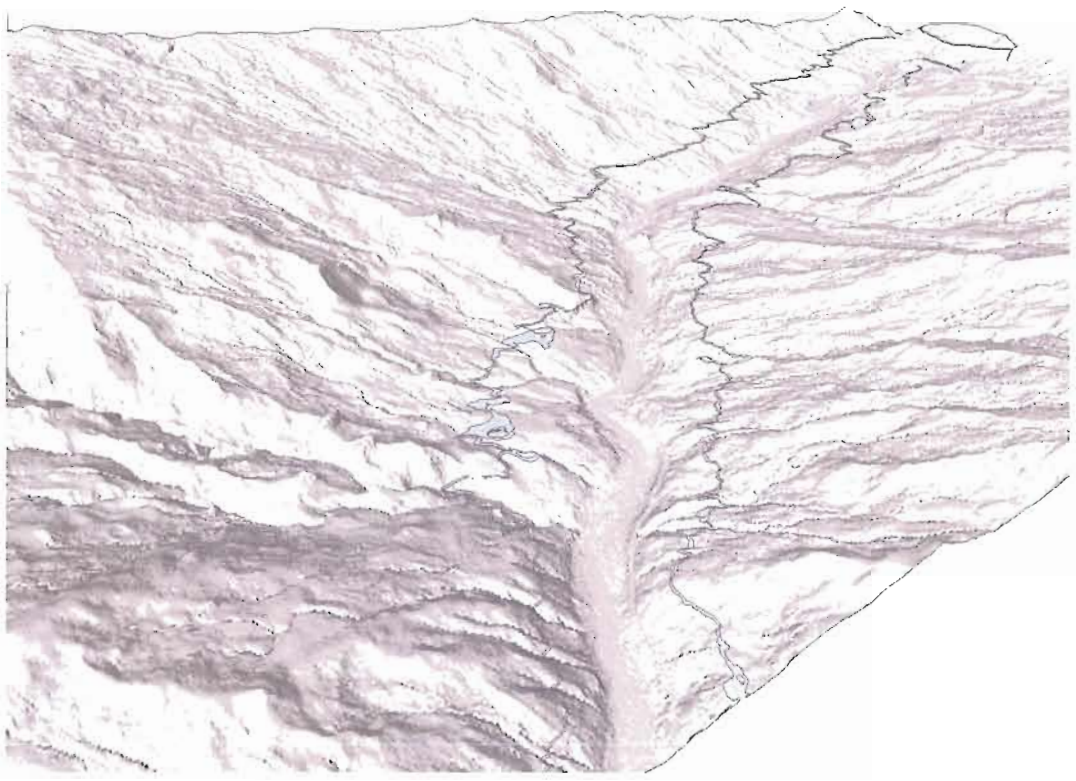

Figure 1. Oblique view up the Eel River canyon. Map is filtered shaded relief LiDAR. Blue line represents elevation between 240 m and 243 m, showing broad flat areas defining the edge of the paleolake.

Figure 2. Southern section of the LiDAR coverage - filtered shaded relief. Red shading depicts elevation from 240 to 243 m. Boxes show where there are flat terrace features at this elevation, and possibly represent shoreline features from the landslide dammed paleolake.


N
1 km

I discovered outcrops of finely laminated sediments along Kekawaka Creek at an elevation of ~230 m (457497 E, 4438948 N – UTM Zone 10N). The deposits are attributable to suspension fallout in standing water (Figs. 3–4). Packages of clast supported angular gravels separate the fine grained laminated sequences, and I interpret these deposits as debris flows intermittently entering the lake.

Figure 3. Exposure of finely laminated deposits interlayered with clast supported angular gravels. Grid is 0.5 m squares.

Figure 4. Sample of finely laminated silts. Under a binocular microscope, I picked fine detrital charcoal for ^{14}C dating. The silts showed extensive faulting and deformation, probably due to post depositional slumping. Knife handle is 94 mm long.

Sample ID	Lab	Lab ID	Sample Description	Source	^{14}C Age (yr)	Error	Calendar Age (yr)	Error
KW 1 C	LLNL	144860	Bark	Paleosol	210	30	230	80
KW 3-1	LLNL	144861	Detrital charcoal	Laminated silts	21440	80	25745	154
KW 4-1	LLNL	144862	Detrital charcoal	Laminated silts	19020	60	22592	95
KW2:8	Beta	Beta-256979	Detrital Charcoal	Laminated silts	36050	300	41306	320
KW2:9	Beta	Beta-256980	Wood	Laminated silts	80	40	N/A	N/A

Table 1. ^{14}C ages of fine grained deposits. LLNL is Lawrence Livermore National Laboratory, and Beta is Beta Analytic. Calibration is from Fairbanks et al. (2005).

Accelerator Mass Spectrometry dating of detrital charcoal in the finely laminated sediments found in the Kekawaka Creek exposure gives a range of radiocarbon ages (Table 1). Both intact samples (KW 1C and KW2:9) have modern ages, and I consider these modern roots. The detrital charcoal samples all returned late Pleistocene ages. Detrital charcoal should be assumed a maximum age given inheritance issues, and the younger of multiple samples is preferred. As there are samples reasonably close in age at 22,592 and 25,745 years, these dates are preferred to the older date. I interpret the sediments to have been deposited after the youngest age, possibly just prior to the Last Glacial Maximum.

We observe a large landslide scar coming off Neafus Pk (Fig. 5), a large sandstone outcrop east of the Eel River. This landslide scar has the volume, relief and lithology to conceivably dam the Eel River for a period sufficient for a lake to create shoreline features, and for lacustrine deposits to accumulate.

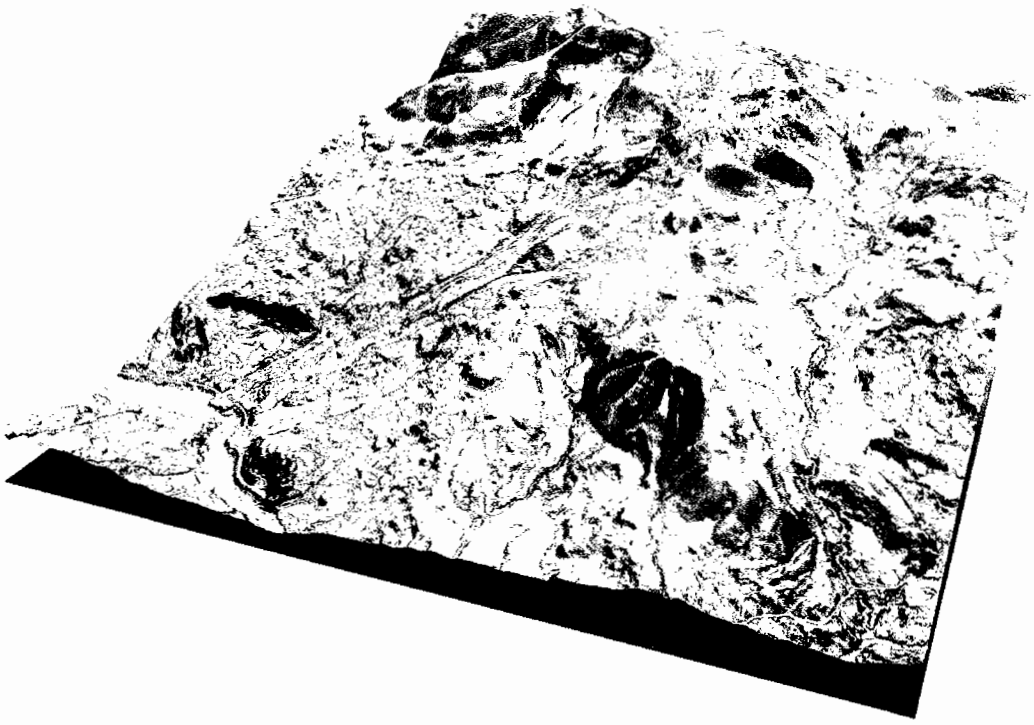

Figure 4. Oblique view of Nefus Peak showing a large landslide scar just below the ridgeline. Landslide scar is 454760 E, 4442860 N (UTM Zone 10).

Most pertinent to the earthflow research is that some of these apparent shoreline features are cut into the toes of huge dormant earthflows flanking the Eel River canyon. This suggests the earthflows have been dormant at least since the lake was present, potentially since before the Last Glacial Maximum, and provides a novel relative means of constraining the timing of earthflow activity

References for Appendix C

Fairbanks, R. G., Mortlock, R. A., Chiu, T. C., Cao, L., Kaplan, A., Guilderson, T. P., Fairbanks, T. W., Bloom, A. L., Grootes, P. M., and Nadeau, M. J., 2005, Radiocarbon calibration curve spanning 0 to 50,000 years BP based on paired Th-230/U-234/U-238 and C-14 dates on pristine corals: Quaternary Science Reviews, v. 24, no. 16-17, p. 1781-1796.

APPENDIX D

AERIAL PHOTOGRAPHS USED IN CHAPTER IV

Date	Photo numbers	Source	CFL (mm)	Fiducials	Image Format	Resolution (dpi)
8-19-1944	DDD 54-30:50 DDD 57-39:59	DoD USFS-6RNF	210 (est.)	Measured	Scanned print	800
7-19-1954	CVL 6N 66:70	HumCo	209.55	Measured	Scanned print	1200
6-24-1960	HS 36 07:15	HumCo	303 (est.)	Measured	Scanned print	1200
6-13-1964	VBAG 1-148, 2-81:85	USGS	151.67	Measured	Scanned print	1800
1968	AF1968 268	Air Force c/o USFS-6RNF	151.484	Measured	Scanned Print	1600
7-22-1968	VBZX 1- 160:163	USGS	152.45	Measured	Scanned print	1800
7-10-1972	F60BP 0172 108	USFS-6RNF	152.57	Supplied	Scanned print	1600
7-25-1972	MEND 9-77 MEND 10-84	Mendocino Co	209.55	Measured	Scanned print	1200
7-22-1976	VEEX 1- 97:104	UC Berkeley	152.21	Supplied	Scanned Diapositive	2400
7-08-1981	VEZF 2-4	USGS	152.347	Supplied	Scanned print	1800
7-26-1991	10-23:25 10-66:72	WAC (91CA)	152.903	Supplied	Scanned Diapositive	1200
08-12-1998	10477-194:195 10480-256:259	USGS	153.212	Supplied	Scanned Print	1800
9-24-2006 - 9-26-2006	Unfiltered Lidar	NCALM	NA	NA	1m DEM	1m

Table 1. Aerial photos used to track earthflow movement in Chapter IV. Est. indicates the camera focal length (CFL) was estimated.

Sources of aerial photographs in Table 1:

DoD: Department of Defense
HumCo: Humboldt County Department of Public Works, Eureka, CA
USGS: US Geological Survey Earth Explorer (Online store)
USFS-SRNF: US Forest Service, Six Rivers National Forest, Eureka, CA
Mendocino Co: Mendocino County Assessors Office, Ukiah, CA
UC Berkeley: UC Berkeley Earth Science and Map Library
WAC: Western Air Corporation, Eugene, OR
NCALM: National Center for Airborne Laser Mapping

REFERENCES

Chapter I

Bovis, M. J., and Jones, P., 1992, Holocene History of Earthflow Mass Movements in South-Central British-Columbia - the Influence of Hydroclimatic Changes: Canadian Journal of Earth Sciences, v. 29, no. 8, p. 1746-1755.

Brown, W. M., and Ritter, J. R., 1971, Sediment Transport and Tubidity in the Eel River Basin, California: Geological Survey Water-Supply Paper, v. 1986, p. 67.

Chorley, R. J., Dunn, A. J., and Beckinsale, R. P., 1991, Historical and regional geomorphology, 1890-1950, The history of the study of landforms; or, The development of geomorphology: New York, Wiley.

Coe, J. A., Ellis, W. L., Godt, J. W., Savage, W. Z., Savage, J. E., Michael, J. A., Kibler, J. D., Powers, P. S., Lidke, D. J., and Debray, S., 2003, Seasonal movement of the Slumgullion landslide determined from Global Positioning System surveys and field instrumentation, July 1998-March 2002: Engineering Geology, v. 68, no. 1-2, p. 67-101.

Davis, W. M., 1899, The Geographic Cycle: The Geographic Journal, v. 14, no. 5, p. 481-504.

Dietrich, W. E., Bellugi, D. G., Sklar, L. S., Stock, J. D., Heimsath, A. M., and Roering, J. J., 2003, Geomorphic Transport Laws for Predicting Landscape Form and Dynamics, *in* Wilcock, P., and Iverson, R. M., eds., Prediction in Geomorphology: Washington DC, American Geophysical Union, p. 103-132.

Dietrich, W. E., and Perron, J. T., 2006, The search for a topographic signature of life: Nature, v. 439, no. 7075, p. 411-418.

Dwyer, M. J., Scott, R. G., and Lorens, P. J., 1971, Landslide Conditions and Related Sediment Production on the Eel River: California Department of Water Resources.

Iverson, R. M., and Major, J. J., 1987, Rainfall, Groundwater-Flow, and Seasonal Movement at Minor Creek Landslide, Northwestern California - Physical

Interpretation of Empirical Relations: Geological Society of America Bulletin, v. 99, no. 4, p. 579-594.

Kelsey, H. M., 1978, Earthflows in Franciscan Melange, Van Duzen River Basin, California: Geology, v. 6, no. 6, p. 361-364.

Malamud, B. D., Turcotte, D. L., Guzzetti, F., and Reichenbach, P., 2004, Landslide inventories and their statistical properties: Earth Surface Processes and Landforms, v. 29, no. 6, p. 687-711.

Maquaire, O., Malet, J. P., Remaitre, A., Locat, J., Klotz, S., and Guillon, J., 2003, Instability conditions of marly hillslopes: towards landsliding or gullying? The case of the Barcelonnette Basin, South East France: Engineering Geology, v. 70, no. 1-2, p. 109-130.

Penck, W., 1953, Morphological Analysis of Landforms: London, MacMillan and Co., 424+ p.

Perron, J. T., Kirchner, J. W., and Dietrich, W. E., 2009, Formation of evenly spaced ridges and valleys: Nature, v. 460, no. 7254, p. 502-505.

Seidl, M. A., and Dietrich, W. E., 1992, The Problem of Channel Erosion into Bedrock: Catena Supplement, v. 23, p. 101-124.

Trotter, C. M., 1993, Weathering and Regolith Properties at an Earthflow Site: Quarterly Journal of Engineering Geology, v. 26, no. 3, p. 163-178.

Chapter II

Abry, P., *ONDELETTES ET TURBULENCES - Multirésolutions, algorithmes de décompositions, invariance d'échelle et signaux de pression*, 290 pp., Diderot, Editeur des Sciences et des Arts, Paris, 1997.

Azanon, J.M., A. Azor, J.V. Perez-Pena, and J.M. Carrillo, Late Quaternary large-scale rotational slides induced by river incision: The Arroyo de Gor area (Guadix basin, SE Spain), *Geomorphology*, *69* (1-4), 152-168, 2005.

Barron, J.A., L. Heusser, T. Herbert, and M. Lyle, High-resolution climatic evolution of coastal northern California during the past 16,000 years, *Paleoceanography*, *18* (1), 2003.

Booth, A.M., J.J. Roering, and J.T. Perron, Automated landslide mapping using spectral analysis and high-resolution topographic data: Puget Sound lowlands, Washington, and Portland Hills, Oregon, *Geomorphology*, *109* (3-4), 132-147, 2009.

Cendrero, A., and F. Dramis, The contribution of landslides to landscape evolution in Europe, *Geomorphology*, *15* (3-4), 191-211, 1996.

Cruden, D.M., and D.J. Varnes, Landslide Types and Processes, in *Landslides: Investigation and Mitigation*, edited by A.K. Turner, and R.L. Schuster, pp. 36-71, National Academy Press, Washington, DC, 1996.

Densmore, A.L., R.S. Anderson, B.G. McAdoo, and M.A. Ellis, Hillslope evolution by bedrock landslides, *Science*, *275* (5298), 369-372, 1997.

Densmore, A.L., M.A. Ellis, and R.S. Anderson, Landsliding and the evolution of normal-fault-bounded mountains, *Journal of Geophysical Research - Solid Earth*, *103* (B7), 15203-15219, 1998.

Densmore, A.L., and N. Hovius, Topographic fingerprints of bedrock landslides, *Geology*, *28* (4), 371-374, 2000.

Dietrich, W.E., D.G. Bellugi, L.S. Sklar, J.D. Stock, A.M. Heimsath, and J.J. Roering, Geomorphic Transport Laws for Predicting Landscape Form and Dynamics, in *Prediction in Geomorphology*, edited by P. Wilcock, and R.M. Iverson, pp. 103-132, American Geophysical Union, Washington DC, 2003.

Dietrich, W.E., and J.T. Perron, The search for a topographic signature of life, *Nature*, *439* (7075), 411-418, 2006.

Ferguson, R.I., Meander Irregularity and Wavelength Estimation, *Journal of Hydrology*, *26* (3-4), 315-333, 1975.

Finnegan, N.J., L.S. Sklar, and T.K. Fuller, Interplay of sediment supply, river incision, and channel morphology revealed by the transient evolution of an experimental bedrock channel, *Journal of Geophysical Research-Earth Surface*, *112* (F3), 2007.

Fuller, T.K., L.A. Perg, J.K. Willenbring, and K. Lepper, Field evidence for climate-driven changes in sediment supply leading to strath terrace formation, *Geology*, *37*, 2009.

Furlong, K.P., and S.Y. Schwartz, Influence of the Mendocino triple junction on the tectonics of coastal California, *Annual Review of Earth and Planetary Sciences*, *32*, 403-433, 2004.

Gangodagamage, C., E. Barnes, and E. Foufoula-Georgiou, Scaling in river corridor widths depicts organization in valley morphology, *Geomorphology*, *91* (3-4), 198-215, 2007.

Griffiths, J.S., A.B. Hart, A.E. Mather, and M. Stokes, Assessment of some spatial and temporal issues in landslide initiation within the Rio Aguas Catchment, South-East Spain, *Landslides*, *2* (3), 183-192, 2005.

Harvey, A.M., Coupling between hillslopes and channels in upland fluvial systems: implications for landscape sensitivity, illustrated from the Howgill Fells, northwest England, *Catena*, *42* (2-4), 225-250, 2001.

Hasbargen, L.E., and C. Paola, Landscape instability in an experimental drainage basin, *Geology*, *28* (12), 1067-1070, 2000.

Hilley, G.E., and J.R. Arrowsmith, Geomorphic response to uplift along the Dragon's Back pressure ridge, Carrizo Plain, California, *Geology*, *36* (5), 367-370, 2008.

Hovius, N., C.P. Stark, and P.A. Allen, Sediment flux from a mountain belt derived by landslide mapping, *Geology*, *25* (3), 231-234, 1997.

Hovius, N., C.P. Stark, H.T. Chu, and J.C. Lin, Supply and removal of sediment in a landslide-dominated mountain belt: Central Range, Taiwan, *Journal of Geology*, *108* (1), 73-89, 2000.

Hovius, N., C.P. Stark, M.A. Tutton, and L.D. Abbott, Landslide-driven drainage network evolution in a pre-steady-state mountain belt: Finisterre Mountains, Papua New Guinea, *Geology*, *26* (12), 1071-1074, 1998.

Hugenholtz, C., and D. Lacelle, Geomorphic controls on landslide activity in Champlain sea clays along Green's Creek, Eastern Ontario, Canada, *Geographie physique et Quaternaire*, *58* (1), 9-23, 2004.

Iverson, R.M., and J.J. Major, Rainfall, Groundwater-Flow, and Seasonal Movement at Minor Creek Landslide, Northwestern California - Physical Interpretation of Empirical Relations, *Geological Society of America Bulletin*, *99* (4), 579-594, 1987.

Jayko, A.S., M.C. Blake, R.J. McLaughlin, H.N. Ohlin, S.D. Ellen, and H.M. Kelsey, Reconnaissance Geologic Map of the Covelo 30- by 60- Minute Quadrangle, Northern California, US Geological Survey, 1989.

Kelsey, H.M., Earthflows in Franciscan Melange, Van Duzen River Basin, California, *Geology*, *6* (6), 361-364, 1978.

Korup, O., Geomorphic imprint of landslides on alpine river systems, southwest New Zealand, *Earth Surface Processes and Landforms*, *30* (7), 783-800, 2005a.

Korup, O., Large landslides and their effect on sediment flux in South Westland, New Zealand, *Earth Surface Processes and Landforms*, *30* (3), 305-323, 2005b.

Korup, O., Effects of large deep-seated landslides on hillslope morphology, western Southern Alps, New Zealand, *Journal of Geophysical Research - Earth Surface*, *111* (F1), 2006.

Korup, O., J.J. Clague, R.L. Hermanns, K. Hewitt, A.L. Strom, and J.T. Weidinger, Giant landslides, topography, and erosion, *Earth and Planetary Science Letters*, *261* (3-4), 578-589, 2007.

Lashermes, B., E. Foufoula-Georgiou, and W.E. Dietrich, Channel network extraction from high resolution topography using wavelets, *Geophysical Research Letters*, *34* (23), 2007.

Lock, J., H. Kelsey, K. Furlong, and A. Woolace, Late neogene and quaternary landscape evolution of the northern California Coast Ranges: Evidence for Mendocino triple junction tectonics, *Geological Society of America Bulletin*, *118* (9-10), 1232-1246, 2006.

Malamud, B.D., D.L. Turcotte, F. Guzzetti, and P. Reichenbach, Landslide inventories and their statistical properties, *Earth Surface Processes and Landforms*, *29* (6), 687-711, 2004.

Mather, A.E., J.S. Griffiths, and M. Stokes, Anatomy of a 'fossil' landslide from the Pleistocene of SE Spain, *Geomorphology*, *50* (1-3), 135-149, 2003.

McKean, J., and J. Roering, Objective landslide detection and surface morphology mapping using high-resolution airborne laser altimetry, *Geomorphology*, *57* (3-4), 331-351, 2004.

McKean, J.A., D.J. Isaak, and C.W. Wright, Geomorphic controls on salmon nesting patterns described by a new, narrow-beam terrestrial-aquatic lidar, *Frontiers in Ecology and the Environment*, *6* (3), 125-130, 2008.

Meunier, P., N. Hovius, and A.J. Haines, Regional patterns of earthquake-triggered landslides and their relation to ground motion, *Geophysical Research Letters*, *34* (20), 2007.

Niemi, N.A., M. Oskin, D.W. Burbank, A.M. Heimsath, and E.J. Gabet, Effects of bedrock landslides on cosmogenically determined erosion rates, *Earth and Planetary Science Letters*, *237* (3-4), 480-498, 2005.

Ouimet, W.B., K.X. Whipple, L.H. Royden, Z.M. Sun, and Z.L. Chen, The influence of large landslides on river incision in a transient landscape: Eastern margin of the Tibetan Plateau (Sichuan, China), *Geological Society of America Bulletin*, *119* (11-12), 1462-1476, 2007.

Palmquist, R.C., and G. Bible, Conceptual Modeling of Landslide Distribution in Time and Space, *Bulletin of the International Association of Engineering Geology*, *21*, 178-186, 1980.

Pisias, N.G., A.C. Mix, and L. Heusser, Millennial scale climate variability of the northeast Pacific Ocean and northwest North America based on radiolaria and pollen, *Quaternary Science Reviews*, *20* (14), 1561-1576, 2001.

Roering, J.J., J.W. Kirchner, and W.E. Dietrich, Characterizing structural and lithologic controls on deep-seated landsliding: Implications for topographic relief and landscape evolution in the Oregon Coast Range, USA, *Geological Society of America Bulletin*, *117* (5-6), 654-668, 2005.

Schmidt, K.M., and D.R. Montgomery, Limits to Relief, *Science*, *270* (5236), 617-620, 1995.

Seidl, M.A., and W.E. Dietrich, The Problem of Channel Erosion into Bedrock, *Catena Supplement*, *23*, 101-124, 1992.

Stark, C.P., A self-regulating model of bedrock river channel geometry, *Geophysical Research Letters*, *33* (4), 2006.

Stock, J.D., and W.E. Dietrich, Erosion of steepland valleys by debris flows, *Geological Society of America Bulletin*, *118* (9-10), 1125-1148, 2006.

Terzaghi, K., Mechanism of Landslides, in *Application of geology to engineering practice*, edited by S. Paige, pp. 83-123, Geological Society of America, New York, 1950.

Van den Eeckhaut, M., J. Poesen, G. Govers, G. Verstraeten, and A. Demoulin, Characteristics of the size distribution of recent and historical landslides in a populated hilly region, *Earth and Planetary Science Letters*, *256* (3-4), 588-603, 2007.

Van Den Eeckhaut, M., J. Poesen, G. Verstraeten, V. Vanacker, J. Moeyersons, J. Nyssen, and L.P.H. van Beek, The effectiveness of hillshade maps and expert knowledge in mapping old deep-seated landslides, *Geomorphology*, *67* (3-4), 351-363, 2005.

Whipple, K.X., Bedrock rivers and the geomorphology of active orogens, *Annual Review of Earth and Planetary Sciences*, *32*, 151-185, 2004.

Wieczorek, G.F., Preparing a detailed landslide-inventory map for hazard evaluation and reduction, *Bulletin of the Association of Engineering Geologists*, *21* (3), 337-342, 1984.

Wills, C.J., and T.P. McCrink, Comparing landslide inventories: The map depends on the method, *Environmental & Engineering Geoscience*, *8* (4), 279-293, 2002.

Zhou, Z.Q., Wavelet energy spectrum for time-frequency localization of earthquake energy, *International Journal of Imaging Systems and Technology*, *13* (2), 133-140, 2003.

Chapter III

Baum, R.L., Messerich, J., and Fleming, R.W., 1998, Surface deformation as a guide to kinematics and three-dimensional shape of slow-moving, clay-rich landslides, Honolulu, Hawaii: Environmental & Engineering Geoscience, v. 4, p. 283–306.

Bovis, M.J., and Jones, P., 1992, Holocene History of Earthflow Mass Movements in South-Central British-Columbia - the Influence of Hydroclimatic Changes: Canadian Journal of Earth Sciences, v. 29, p. 1746–1755.

Brown, W.M., and Ritter, J.R., 1971, Sediment Transport and Tubidity in the Eel River Basin, California: Geological Survey Water-Supply Paper, v. 1986, p. 67.

Coe, J.A., Ellis, W.L., Godt, J.W., Savage, W.Z., Savage, J.E., Michael, J.A., Kibler, J.D., Powers, P.S., Lidke, D.J., and Debray, S., 2003, Seasonal movement of the Slumgullion landslide determined from Global Positioning System surveys and field instrumentation, July 1998-March 2002: Engineering Geology, v. 68, p. 67–101, doi: 10.1016/S0013-7952(02)00199-0.

Dietrich, W.E., and Perron, J.T., 2006, The search for a topographic signature of life: Nature, v. 439, p. 411–418, doi: 10.1038/nature04452.

Fuller, T.K., Perg, L.A., Willenbring, J.K., and Lepper, K., 2009, Field evidence for climate-driven changes in sediment supply leading to strath terrace formation: Geology, v. 37, 467–470

Iverson, R.M., and Major, J.J., 1987, Rainfall, Groundwater-Flow, and Seasonal Movement at Minor Creek Landslide, Northwestern California - Physical

Interpretation of Empirical Relations: Geological Society of America Bulletin, v. 99, p. 579–594, doi: 10.1130/0016-7606(1987)99<579:RGFASM>2.0.CO;2.

Keefer, D.K., and Johnson, A.M., 1983, Earth Flows: Morphology, Mobilization and Movement: Geological Survey Professional Paper, v. 1256, p. 1–56.

Kelsey, H.M., 1978, Earthflows in Franciscan Melange, Van Duzen River Basin, California: Geology, v. 6, p. 361–364, doi: 10.1130/0091-7613(1978)6<361:EIFMVD>2.0.CO;2.

McKean, J.A., Dietrich, W.E., Finkel, R.C., Southon, J.R., and Caffee, M.W., 1993, Quantification of Soil Production and Downslope Creep Rates from Cosmogenic Be-10 Accumulations on a Hillslope Profile: Geology, v. 21, p. 343–346, doi: 10.1130/0091-7613(1993)021<0343:QOSPAD>2.3.CO;2.

Monaghan, M.C., and Elmore, D., 1994, Garden-Variety Be-10 in Soils on Hill Slopes: Nuclear Instruments & Methods in Physics Research. Section B, Beam Interactions with Materials and Atoms, v. 92, p. 357–361, doi: 10.1016/0168-583X(94)96034-8.

Pavich, M.J., Brown, L., Harden, J., Klein, J., and Middleton, R., 1986, Be-10 Distribution in Soils from Merced River Terraces, California: Geochimica et Cosmochimica Acta, v. 50, p. 1727–1735, doi: 10.1016/0016-7037(86)90134-1.

Pavich, M.J., and Chadwick, O.A., 1997, 10Be soil inventories along a climatic gradient on Kohala Mountain: Geological Society of America, Cordilleran Section, 93rd annual meeting Abstracts with Programs, v. 29, p. 56.

Stone, J., 1998, A rapid fusion method for separation of beryllium-10 from soils and silicates: Geochimica et Cosmochimica Acta, v. 62, p. 555–561, doi: 10.1016/S0016-7037(97)00369-4.

Syvitski, J.P., and Morehead, M.D., 1999, Estimating river-sediment discharge to the ocean: application to the Eel margin, northern California: Marine Geology, v. 154, p. 13–28, doi: 10.1016/S0025-3227(98)00100-5.

Walstra, J., Dixon, N., and Chandler, J.H., 2007, Historical aerial photographs for landslide assessment: two case histories: Quarterly Journal of Engineering Geology and Hydrogeology, v. 40, p. 315–332, doi: 10.1144/1470-9236/07-011.

Wolf, P.R., and Dewitt, B.A., 2000, Elements of Photogrammetry. With Applications in GIS: Boston, MA, McGraw-Hill.

You, C.F., Lee, T., and Li, Y.H., 1989, The Partition of Be between Soil and Water: Chemical Geology, v. 77, p. 105–118, doi: 10.1016/0009-2541(89)90136-8.

Zhang, X.B., Phillips, C., and Pearce, A., 1991, Surface Movement in an Earthflow Complex, Raukumara Peninsula, New-Zealand: Geomorphology, v. 4, p. 261–272, doi: 10.1016/0169-555X(91)90009-Y.

Chapter IV

Angeli, M. G., Gasparetto, P., Menotti, R. M., Pasuto, A., and Silvano, S., 1996, A visco-plastic model for slope analysis applied to a mudslide in Cortina d'Ampezzo, Italy: Quarterly Journal of Engineering Geology, v. 29, p. 233-240.

Baum, R. L., Fleming, R. W., and Johnson, A. M., 1993, Kinematics of the Aspen Grove Landslide, Ephraim Canyon, Central Utah, Landslide Processes in Utah - Observation and Theory, p. 34.

Bickner, F., 1985, Relative dating and geologic interpretation of thirteen fluvial terraces of the Eel River, northern California: Geological Society of America Abstracts with Programs, v. 17, no. 6, p. 342.

Booth, A. M., Roering, J. J., and Perron, J. T., 2009, Automated landslide mapping using spectral analysis and high-resolution topographic data: Puget Sound lowlands, Washington, and Portland Hills, Oregon: Geomorphology, v. 109, no. 3-4, p. 132-147.

Bovis, M. J., and Jones, P., 1992, Holocene History of Earthflow Mass Movements in South-Central British-Columbia - the Influence of Hydroclimatic Changes: Canadian Journal of Earth Sciences, v. 29, no. 8, p. 1746-1755.

Brown, W. M., and Ritter, J. R., 1971, Sediment Transport and Tubidity in the Eel River Basin, California: Geological Survey Water-Supply Paper, v. 1986, p. 67.

Bruckl, E., and Sehidegger, A. E., 1973, Application of Theory of Plasticity to Slow Mud Flows: Geotechnique, v. 23, no. 1, p. 101-107.

Buis, A., 2008, Larger Pacific Climate Event Helps Current La Nina Linger: NASA JPL, 2008-066.

Burbank, D. W., Leland, J., Fielding, E., Anderson, R. S., Brozovic, N., Reid, M. R., and Duncan, C., 1996, Bedrock incision, rock uplift and threshold hillslopes in the northwestern Himalayas: Nature, v. 379, no. 6565, p. 505-510.

California Department of Water Resources, 1965, Bulletin No. 136 - North Coastal Area Investigation: Department of Water Resources, 136.

-, 1970, Middle Fork Eel River landslide investigation: California Department of Water Resources.

Carson, M. A., and Petley, D. T., 1970, The Existence of Threshold Slopes in the Denudation of the Landscape: Transactions of the Institute of British Geographers, v. 49, p. 77–95.

Carter, W. E., Shrestha, R. L., and Slatton, K. C., 2007, Geodetic laser scanning: Physics Today, v. 60, no. 12, p. 41-47.

Chandler, J. H., and Brunsden, D., 1995, Steady-State Behavior of the Black-Ven Mudslide - the Application of Archival Analytical Photogrammetry to Studies of Landform Change: Earth Surface Processes and Landforms, v. 20, no. 3, p. 255-275.

Coe, J. A., Ellis, W. L., Godt, J. W., Savage, W. Z., Savage, J. E., Michael, J. A., Kibler, J. D., Powers, P. S., Lidke, D. J., and Debray, S., 2003, Seasonal movement of the Slumgullion landslide determined from Global Positioning System surveys and field instrumentation, July 1998-March 2002: Engineering Geology, v. 68, no. 1-2, p. 67-101.

Cruden, D. M., and Varnes, D. J., 1996, Landslide Types and Processes, *in* Turner, A. K., and Schuster, R. L., eds., Landslides: Investigation and Mitigation: Washington, DC, National Academy Press, p. 36-71.

Densmore, A. L., Anderson, R. S., McAdoo, B. G., and Ellis, M. A., 1997, Hillslope evolution by bedrock landslides: Science, v. 275, no. 5298, p. 369-372.

Densmore, A. L., Ellis, M. A., and Anderson, R. S., 1998, Landsliding and the evolution of normal-fault-bounded mountains: Journal of Geophysical Research - Solid Earth, v. 103, no. B7, p. 15203-15219.

Densmore, A. L., and Hovius, N., 2000, Topographic fingerprints of bedrock landslides: Geology, v. 28, no. 4, p. 371-374.

Dietrich, W. E., Bellugi, D. G., Sklar, L. S., Stock, J. D., Heimsath, A. M., and Roering, J. J., 2003, Geomorphic Transport Laws for Predicting Landscape Form and Dynamics, *in* Wilcock, P., and Iverson, R. M., eds., Prediction in Geomorphology: Washington DC, American Geophysical Union, p. 103-132.

Dietrich, W. E., and Dunne, T., 1978, Sediment budget for a small catchment in mountainous terrain: Zeitschrift Fur Geomorphologie, v. 29, p. 191-206.

Dwyer, M. J., Scott, R. G., and Lorens, P. J., 1971, Landslide Conditions and Related Sediment Production on the Eel River: California Department of Water Resources.

Fuller, T. K., Perg, L. A., Willenbring, J. K., and Lepper, K., 2009, Field evidence for climate-driven changes in sediment supply leading to strath terrace formation: Geology, v. 37.

Furlong, K. P., and Govers, R., 1999, Ephemeral crustal thickening at a triple junction: The Mendocino crustal conveyor: Geology, v. 27, no. 2, p. 127-130.

Furlong, K. P., and Schwartz, S. Y., 2004, Influence of the Mendocino triple junction on the tectonics of coastal California: Annual Review of Earth and Planetary Sciences, v. 32, p. 403-433.

Geertsema, M., Clague, J. J., Schwab, J. W., and Evans, S. G., 2006, An overview of recent large catastrophic landslides in northern British Columbia, Canada: Engineering Geology, v. 83, no. 1-3, p. 120-143.

Gendaszek, A., Thompson, N., Balco, G., Todd, C., and Stone, J., 2005, LONG-TERM EROSION RATES OF COASTAL WATERSHEDS IN THE PACIFIC NORTHWEST: Geological Society of America Abstracts with Programs, v. 37, no. 7, p. 200.

Glastonbury, J., and Fell, R., 2008, Geotechnical characteristics of large slow, very slow, and extremely slow landslides: Canadian Geotechnical Journal, v. 45, no. 7, p. 984-1005.

Glenn, N. F., Streutker, D. R., Chadwick, D. J., Thackray, G. D., and Dorsch, S. J., 2006, Analysis of LiDAR-derived topographic information for characterizing and differentiating landslide morphology and activity: Geomorphology, v. 73, no. 1-2, p. 131-148.

Gonzalez-Diez, A., Remondo, J., de Teran, J. R. D., and Cendrero, A., 1999, A methodological approach for the analysis of the temporal occurrence and triggering factors of landslides: Geomorphology, v. 30, no. 1-2, p. 95-113.

Guzzetti, F., Malamud, B. D., Turcotte, D. L., and Reichenbach, P., 2002, Power-law correlations of landslide areas in central Italy: Earth and Planetary Science Letters, v. 195, no. 3-4, p. 169-183.

Harden, D. R., Colman, S. M., and Nolan, K. M., Mass Movement in the Redwood Creek Basin, Northwestern California: U.S. Geological Survey Profesisonal Paper, v. 1454-G, p. G1-G11.

Hilley, G. E., Burgmann, R., Ferretti, A., Novali, F., and Rocca, F., 2004, Dynamics of slow-moving landslides from permanent scatterer analysis: Science, v. 304, no. 5679, p. 1952-1955.

Hovius, N., Stark, C. P., and Allen, P. A., 1997, Sediment flux from a mountain belt derived by landslide mapping: Geology, v. 25, no. 3, p. 231-234.

Hovius, N., Stark, C. P., Tutton, M. A., and Abbott, L. D., 1998, Landslide-driven drainage network evolution in a pre-steady-state mountain belt: Finisterre Mountains, Papua New Guinea: Geology, v. 26, no. 12, p. 1071-1074.

Hungr, O., Evans, S. G., Bovis, M. J., and Hutchinson, J. N., 2001, A review of the classification of landslides of the flow type: Environmental & Engineering Geoscience, v. 7, no. 3, p. 221-238.

Hutchinson, J. N., 1967, The Free Degredation of London Clay Cliffs, *in* Proc. Geotechnical Conf., Oslo, p. 113-118.

Hutchinson, J. N., and Bhandari, R. K., 1971, Undrained Loading, a Fundamental Mechanism of Mudflows and Other Mass Movements: Geotechnique, v. 21, no. 4, p. 353-&.

Iverson, N. R., 1986a, Dynamics of slow landslides: a theory for time-dependent behavior, *in* Abrahams, A. D., ed., Hillslope Processes: Boston, Mass, Allen and Unwin, p. 297-317.

Iverson, R. M., 1986b, Unsteady, Nonuniform Landslide Motion .1. Theoretical Dynamics and the Steady Datum State: Journal of Geology, v. 94, no. 1, p. 1-15.

-, 1986c, Unsteady, Nonuniform Landslide Motion .2. Linearized Theory and the Kinematics of Transient-Response: Journal of Geology, v. 94, no. 3, p. 349-364.

-, 2005, Regulation of landslide motion by dilatancy and pore pressure feedback: Journal of Geophysical Research - Earth Surface, v. 110, no. F2.

Iverson, R. M., and Major, J. J., 1987, Rainfall, Groundwater-Flow, and Seasonal Movement at Minor Creek Landslide, Northwestern California - Physical Interpretation of Empirical Relations: Geological Society of America Bulletin, v. 99, no. 4, p. 579-594.

Jayko, A. S., Blake, M. C., McLaughlin, R. J., Ohlin, H. N., Ellen, S. D., and Kelsey, H. M., 1989, Reconnaissance Geologic Map of the Covelo 30- by 60- Minute Quadrangle, Northern California: US Geological Survey, scale 1:100,000.

Keefer, D. K., and Johnson, A. M., 1983, Earth Flows: Morphology, Mobilization and Movement: Geological Survey Professional Paper, v. 1256, p. 1-56.

Kelsey, H. M., 1977, Landsliding, channel changes, sediment yield and land use in the Van Duzen River basin, north coastal California, 1941 - 1975 [Ph.D. thesis]: University of California, Santa Cruz, 370 p.

-, 1978, Earthflows in Franciscan Melange, Van Duzen River Basin, California: Geology, v. 6, no. 6, p. 361-364.

-, 1980, A Sediment Budget and an Analysis of Geomorphic Process in the Van-Duzen River Basin, North Coastal California, 1941-1975 - Summary: Geological Society of America Bulletin, v. 91, no. 4, p. 190-195.

Kelsey, H. M., and Carver, G. A., 1988, Late Neogene and Quaternary Tectonics Associated with Northward Growth of the San-Andreas Transform-Fault, Northern California: Journal of Geophysical Research-Solid Earth and Planets, v. 93, no. B5, p. 4797-4819.

Korup, O., 2005, Large landslides and their effect on sediment flux in South Westland, New Zealand: Earth Surface Processes and Landforms, v. 30, no. 3, p. 305-323.

-, 2006, Rock-slope failure and the river long profile: Geology, v. 34, no. 1, p. 45-48.

Korup, O., Clague, J. J., Hermanns, R. L., Hewitt, K., Strom, A. L., and Weidinger, J. T., 2007, Giant landslides, topography, and erosion: Earth and Planetary Science Letters, v. 261, no. 3-4, p. 578-589.

Lehre, A. K., and Carver, G. A., 1985, Thrust faulting and earthflows: Speculations on the sediment budget of a tectonically active drainage basin, *in* Savina, M. E., ed., American Geomorphological Field Group Field Trip Guidebook 1985 Conference, p. 169-183.

Leprince, S., Berthier, E., Ayoub, F., Delacourt, C., and Avouac, J. P., 2008, Monitoring Earth Surface Dynamics With Optical Imagery: EOS, Transactions, American Geophysical Union, v. 89, no. 1, p. 1-2.

Lins, H. F., and Slack, J. R., 1999, Streamflow trends in the United States: Geophysical Research Letters, v. 26, no. 2, p. 227-230.

Lock, J., Kelsey, H., Furlong, K., and Woolace, A., 2006, Late neogene and quaternary landscape evolution of the northern California Coast Ranges: Evidence for Mendocino triple junction tectonics: Geological Society of America Bulletin, v. 118, no. 9-10, p. 1232-1246.

Luce, C. H., and Holden, Z. A., 2009, Declining annual streamflow distributions in the Pacific Northwest United States, 1948-2006: Geophysical Research Letters, v. 36.

Mackey, B. H., Roering, J. J., and McKean, J. A., 2009, Long-term kinematics and sediment flux of an active earthflow, Eel River, California: Geology, v. 37, no. 9, p. 803-806.

Malamud, B. D., Turcotte, D. L., Guzzetti, F., and Reichenbach, P., 2004, Landslide inventories and their statistical properties: Earth Surface Processes and Landforms, v. 29, no. 6, p. 687-711.

Malet, J. P., Maquaire, O., and Calais, E., 2002, The use of Global Positioning System techniques for the continuous monitoring of landslides: application to the Super-Sauze earthflow (Alpes-de-Haute-Provence, France): Geomorphology, v. 43, no. 1-2, p. 33-54.

Malhase, J., 1938, Landslide at Mile Post 201 Telegraph Poles 9 to 12, Northwestern Pacific Railroad.

Mantua, N. J., and Hare, S. R., 2002, The Pacific decadal oscillation: Journal of Oceanography, v. 58, no. 1, p. 35-44.

Mantua, N. J., Hare, S. R., Zhang, Y., Wallace, J. M., and Francis, R. C., 1997, A Pacific interdecadal climate oscillation with impacts on salmon production: Bulletin of the American Meteorological Society, v. 78, no. 6, p. 1069-1079.

Maquaire, O., Malet, J. P., Remaitre, A., Locat, J., Klotz, S., and Guillon, J., 2003, Instability conditions of marly hillslopes: towards landsliding or gullying? The case of the Barcelonnette Basin, South East France: Engineering Geology, v. 70, no. 1-2, p. 109-130.

McKean, J., and Roering, J., 2004, Objective landslide detection and surface morphology mapping using high-resolution airborne laser altimetry: Geomorphology, v. 57, no. 3-4, p. 331-351.

McLaughlin, R. J., Ellen, S. D., Blake, M. C. J., Jayko, A. S., Irwin, W. P., Aalto, K. R., Carver, G. A., and Clark, S. H. J., 2000, Geology of the Cape Mendocino, Eureka, Garberville, and Southwestern part of the Hayfork 30 x 60 Minute Quadrangles and Adjacent Offshore Area, Northern California: U.S. Geological Survey.

McLaughlin, R. J., Kling, S. A., Poore, R. Z., McDougall, K., and Beutner, E. C., 1982, Post-Middle Miocene Accretion of Franciscan Rocks, Northwestern California: Geological Society of America Bulletin, v. 93, no. 7, p. 595-605.

McSaveney, M. J., and Griffiths, G. A., 1987, Drought, Rain, and Movement of a Recurrent Earthflow Complex in New-Zealand: Geology, v. 15, no. 7, p. 643-646.

Merritts, D., and Bull, W. B., 1989, Interpreting Quaternary Uplift Rates at the Mendocino Triple Junction, Northern California, from Uplifted Marine Terraces: Geology, v. 17, no. 11, p. 1020-1024.

Merritts, D. J., 1996, The Mendocino triple junction: Active faults, episodic coastal emergence, and rapid uplift: Journal of Geophysical Research-Solid Earth, v. 101, no. B3, p. 6051-6070.

Muhs, D. R., Thorson, R. M., Clague, J. J., Mathews, W. H., McDowell, P. F., and Kelsey, H. M., 1987, Pacific Coast and Mountain System, *in* Graf, W. L., ed., Geomorphic systems of North America: Boulder, Geological Society of America, p. 517-581.

Nittrouer, C. A., 1999, STRATAFORM: overview of its design and synthesis of its results: Marine Geology, v. 154, no. 1-4, p. 3-12.

Nolan, K. M., and Janda, R. J., 1995, Movement and Sediment Yield of Two Earthflows, Northwestern California, *in* Survey, U. S. G., ed., p. F1-F12.

Ohlmacher, G. C., 2007, Plan curvature and landslide probability in regions dominated by earth flows and earth slides: Engineering Geology, v. 91, no. 2-4, p. 117-134.

Ouimet, W. B., Whipple, K. X., and Granger, D. E., 2009, Beyond threshold hillslopes: Channel adjustment to base-level fall in tectonically active mountain ranges: Geology, v. 37, no. 7, p. 579-582.

Perron, J. T., Dietrich, W. E., and Kirchner, J. W., 2008, Controls on the spacing of first-order valleys: Journal of Geophysical Research-Earth Surface, v. 113, no. F4.

Pettinga, J. R., 1987, Waipoapoa Landslide - a Deep-Seated Complex Block Slide in Tertiary Weak-Rock Flysch, Southern Hawkes Bay, New-Zealand: New Zealand Journal of Geology and Geophysics, v. 30, no. 4, p. 401-414.

Roering, J. J., Stimely, L. L., Mackey, B. H., and Schmidt, D. A., 2009, Using DInSAR, airborne LiDAR, and archival air photos to quantify landsliding and sediment transport: Geophysical Research Letters, v. 36.

Savage, W., and Wasowski, J., 2006, A plastic flow model for the Acquara-Vadoncello landslide in Senerchia, Southern Italy: Engineering Geology, v. 83, no. 1-3, p. 4-21.

Schmidt, K. M., and Montgomery, D. R., 1995, Limits to Relief: Science, v. 270, no. 5236, p. 617-620.

Schulz, W. H., 2007, Landslide susceptibility revealed by LIDAR imagery and historical records, Seattle, Washington: Engineering Geology, v. 89, no. 1-2, p. 67-87.

Schulz, W. H., McKenna, J. P., Kibler, J. D., and Biavati, G., 2009, Relations between hydrology and velocity of a continuously moving landslide-evidence of pore-pressure feedback regulating landslide motion?: Landslides, v. 6, no. 3, p. 181-190.

Scott, R. G., 1973, Geology and sediment production for ten Eel River landslides: California Department of Water Resources - Northern District.

Skempton, A. W., 1964, Long-term stability of clay slopes: Geotechnique, v. 14, p. 77-102.

Slama, C. C., 1980, Manual of Photogrammetry: Falls Church, VA, American Society of Photogrammetry, p. 1056.

Slatton, K. C., Carter, W. E., Shrestha, R. L., and Dietrich, W., 2007, Airborne Laser Swath Mapping: Achieving the resolution and accuracy required for geosurficial research: Geophysical Research Letters, v. 34, no. 23.

Sloan, J., Miller, J. R., and Lancaster, N., 2001, Response and recovery of the Eel River, California, and its tributaries to floods in 1955, 1964, and 1997: Geomorphology, v. 36, no. 3-4, p. 129-154.

Smith, B. J., Tilton, W. C., Elko, J. M., and Jacobus, C. D., 1974, Eel River Basin Environmental Studies: California Department of Water Resources

Sommerfield, C. K., Drake, D. E., and Wheatcroft, R. A., 2002, Shelf record of climatic changes in flood magnitude and frequency, north-coastal California: Geology, v. 30, no. 5, p. 395-398.

Sommerfield, C. K., and Nittrouer, C. A., 1999, Modern accumulation rates and a sediment budget for the Eel shelf: a flood-dominated depositional environment: Marine Geology, v. 154, no. 1-4, p. 227-241.

Sommerfield, C. K., and Wheatcroft, R. A., 2007, Late Holocene sediment accumulation on the northern California shelf: Oceanic, fluvial, and anthropogenic influences: Geological Society of America Bulletin, v. 119, no. 9-10, p. 1120-1134.

Swanson, F. J., and Swanston, D. N., 1977, Complex mass-movement terrains in the Western Cascade Range, Oregon: Geological Society of America Reviews in Engineering Geology, v. 3, p. 113-124.

Syvitski, J. P., and Morehead, M. D., 1999, Estimating river-sediment discharge to the ocean: application to the Eel margin, northern California: Marine Geology, v. 154, no. 1-4, p. 13-28.

van Asch, T. W. J., Van Beek, L. P. H., and Bogaard, T. A., 2007, Problems in predicting the mobility of slow-moving landslides: Engineering Geology, v. 91, no. 1, p. 46-55.

Van de Grift, J. W., and Sack, D., 2004, Monitoring slump-earthflow complex movement: A southeastern Ohio case study: Ohio Journal of Science, v. 104, no. 5, p. 126-135.

Van Den Eeckhaut, M., Poesen, J., Verstraeten, G., Vanacker, V., Moeyersons, J., Nyssen, J., and van Beek, L. P. H., 2005, The effectiveness of hillshade maps and expert knowledge in mapping old deep-seated landslides: Geomorphology, v. 67, no. 3-4, p. 351-363.

Vulliet, L., and Hutter, K., 1988, Viscous-Type Sliding Laws for Landslides: Canadian Geotechnical Journal, v. 25, no. 3, p. 467-477.

Wahrhaftig, C., and Curry, R. R., 1967, Geologic implications of sediment discharge recorded from Northern Coast Ranges, California, *in* Man's effect on California watersheds: Report of the California Assembly Committee on Natural Resources, Planning, and Public Works, Subcommittee on Forestry and Watershed Management, Part III, p. 35-58

Wheatcroft, R. A., and Sommerfield, C. K., 2005, River sediment flux and shelf sediment accumulation rates on the Pacific Northwest margin: Continental Shelf Research, v. 25, no. 3, p. 311-332.

Wieczorek, G. F., 1984, Preparing a detailed landslide-inventory map for hazard evaluation and reduction: Bulletin of the Association of Engineering Geologists, v. 21, no. 3, p. 337-342.

Wills, C. J., and McCrink, T. P., 2002, Comparing landslide inventories: The map depends on the method: Environmental & Engineering Geoscience, v. 8, no. 4, p. 279-293.

Wolf, P. R., and Dewitt, B. A., 2000, Elements of Photogrammetry. With Applications in GIS: Boston, MA, McGraw-Hill.

Zhang, X. B., Phillips, C., and Pearce, A., 1991, Surface Movement in an Earthflow Complex, Raukumara Peninsula, New-Zealand: Geomorphology, v. 4, no. 3-4, p. 261-272.